Passage Secondary Flow Effects on Turbine Endwall Discrete Holes Film Cooling – A Literature Survey, New Theory and Measurement

A Dissertation

Submitted to the faculty of the

University of Minnesota by

Ting-Wei Chen

In partial fulfillment of the

requirements for the degree of

Master of Science

Advised by

Prof. Terrence W. Simon

and

Prof. Richard J. Goldstein

August 2024

MECHANICAL ENGINEERING

UNIVERSITY OF MINNESOTA

Isaac Newton,

"The mathematical Principles of Natural Philosophy (1846)/ Book III – Rules"

---

1. We are to admit no more causes of natural things than such as are both true and sufficient to explain their appearances.

2. Therefore, to the same natural effects we must, as far as possible, assign the same causes.

3. The qualities of bodies, which admit neither intensification nor remission of degrees, and which are found to belong to all bodies within the reach of our experiments, are to be esteemed the universal qualities of all bodies whatsoever.

4. In experimental philosophy we are to look upon propositions inferred by general induction from phenomena as accurately or very nearly true, notwithstanding any contrary hypothesis that may be imagined, till such time as other phenomena occur, by which they may either be made more accurate, or liable to exceptions.

Acknowledgement

I would like to start by thanking my two wonderful advisors, Prof. Terrence W. Simon and Prof. Richard J. Goldstein. It is my pleasure to be guided by these two great scientists, learning their viewpoints on research and the broad thermal and fluid area.

I learned many precious lessons from Prof. Terrence W. Simon, ranging from thermal fluid knowledge to his taste in research to writing and presentation skills to his working attitude and leadership to his modest personality to a correct way of thinking. Among these, the most impressive point is that he always challenged me to think from the fundamentals, approaching the problem independently, while finding my research interest along the way. Prof. Terrence Simon is not only a perfect role model in my career, but also like a father who guided me in graduate school.

I would like to thank Prof. Richard J. Goldstein, for calling me from the US when I was in Taiwan, bringing me to study at Minnesota, offering me a chance to join the Heat Transfer Laboratory, and supporting me through my study financially even after he was sick and eventually passed away. One thing I would like to thank him most for is, giving me a well-framed but open-ended research problem, as a continuation of studies in his group. Addressing such a problem taught me to think like an experimentalist, model new problems by handling unknown phenomena, and select the most significant and solvable point to proceed. Reading research articles from his group in the past decades is like learning the history of the convective heat transfer field and his style of doing research.

I would like to thank many people in the group of Heat Transfer Laboratory, and Dept. of Mechanical Engineering.

First, I would like to start by thanking Dr. Matthew Stinson for letting me use his doctoral data in my master thesis. His dedication to his PhD thesis, coupled with his valuable suggestions and support along the path, directly contributes to this thesis. In addition, I would like to thank Mr. Martinez Pajuelo Sergio for our time spent together, especially those days working together in the lab. I learned a lot about his optimism and storied in his country, Peru. Also, I would like to thank Dr. Kedar Nawathe, Dr. Rui Zhu, Mr. Enci Lin, and Mr. Alex Li, for sharing their experience with instruments in the Turbulent Convection Heat Transfer Laboratory. This advice helped me a lot, especially when I first started to set up my experiment.

I must appreciate people in the ME Department. First, I would like to thank Prof. Tianhong Cui, Dr. Peng Zhou, Ms. Jitong Duan, and Mr. Jungyoon Kim, for the group presentations given every week. I learned a lot about selecting a paper and clearly communicating my ideas. In addition, I would like to thank Prof. Vinod Srinivasan, Prof. Jiarong Hong, Prof. Marien Simeni, and Mr. Ankit Saini for choosing me as their teaching assistant in the Thermal Engineering Laboratory and Fluid Mechanics, Thermodynamics, and Heat Transfer courses. I would also like to thank Prof. Jeff Tithof for his guidance in the Computational Heat Transfer course, and the conversations we have had after that. I would like to thank Mr. Reza Yousofvand and Mr. Umberto Costa Bitencourt for the fruitful discussions we had. I would like to thank Prof. Peter Bruggeman for his suggestions in my second year, and, particularly, feedback on the 3MT competition. I would like to thank Anderson student innovation laboratory, for their help with 3D manufacturing and laser cutting on making my discrete hole testing pieces. In addition, I would like to thank Prof. Ellen Longmire and Prof. Chris Hogan, for their great lectures on turbulence and multiphase systems, and for serving on my master's committee.

I would like to thank my undergraduate research advisor, Prof. Shyy-Woei Chang who guided me into convection heat transfer research. As the first to receive a college education in my family, becoming a scientist was never an option in my mind, and even pursuing a career outside of Taiwan. Because of his guidance and support along the path, I was not lost in my undergraduate work, and fortunately, had the privilege to study in Minnesota later. Also, I would like to thank my bosses at ASUS Technology in Taiwan, particularly Mr. Chad Chen, Mr. Andy Yan, and Mr. Glenn Wu. They provided me with a chance to join their team as a college graduate without many experiences. This industrial experience approaching realistic heat transfer problem benefited me a lot when I went back to more sophisticated heat transfer work in graduate school.

Though the last two years in Minnesota were covered by constant challenges, sometimes seems to proceed in a dark cave and can hardly see the end, it is a worthwhile journey and fruitful process when looking back now. The difficulty of this study is far beyond my ability when I started, and what I can accomplish alone. The present thesis is the result of all these great people I have met and who have generously helped me.

Dedication

To my father, who had battled cancer more than a decade without any complaint, taught me never to give up on my dream, always stay optimistic, and care about others.

To Prof. Richard J. Goldstein (March 27, 1928 - March 6, 2023), and the Heat Transfer Laboratory at the University of Minnesota.

Abstract

In this thesis, film cooling effectiveness measurement results representative of gas turbine endwall cooling are discussed with emphasis on describing the effects that features in the complex turbine passage flow have on them. Film cooling is when cool air from elsewhere in the turbine is supplied through walls of the turbine passage that require cooling providing a protective layer of cool air over the surface to partially isolate it from the hot mainstream. Complexity comes from secondary flows naturally occurring in the passage. Important is their influence on film cooling effectiveness. Holes for film cooling injection are typically distributed over the upstream portion of the passage walls in an attempt to cover and protect the full passage. The present study documents separate and combined effects present in the passage by studying a single hole of various shapes, hole orientation angles with respect to the main flow, injection-to-main-flow velocity ratios, and passage flow with and without vortices generated upstream.

Representative endwall surface wall shear fields are documented in the literature as are hole pattern designs. They establish the angle between the near-wall flow approaching a selected hole and the centerline direction of the corresponding hole. Often, shear field data are not available within the passage and approach flow directions to some holes cannot accurately be applied. Then, the flow approaching only holes that are upstream in the passage (particularly, upstream of any coolant injection) can be accurately described**.** Nevertheless, measurements showing migration of coolant on the endwall downstream of selected holes have been valuable to document how coolant is affected by features in the surrounding flow, features such as the momentum of injection, the passage main flow direction, and the effects of vortices in the vicinity of the hole. One example is the discrete hole located under a vortex created at the airfoil leading edge and residing near the passage entrance where ejected coolant is swept by the vortex away from the endwall, resulting in low local values of surface effectiveness. This leaves the upstream endwall regions near the pressure and suction surfaces having difficulty in providing coolant coverage by discrete hole injection. The measurements documented in the present study provide guidance for interpreting such downstream distributions of coolant.

Cases discussed herein have low injection rates upstream of the passage. Studies with high injection rates upstream of the inlet (high ratios of passage inlet momentum flow near the

endwall to passage average momentum flow) are fundamentally different and are not discussed herein. Such cases have strong injection along the endwall immediately upstream of the passage inlet (strong combustor wall cooling) and, thus, would have a different passage secondary flow pattern. Such a pattern is discussed in Nawathe, et al. (2023) as the "impingement vortex."

The measurements of the present study document the endwall coolant coverage and coolant distributions in the flow at several planes downstream of injection. Such data not only show the cooling effectiveness but track the coolant in the passage flow. Flow measurements describe profiles of mean velocity, describing the boundary layer growth and momentum deficit of streamwise momentum upstream and downstream of injection. Understanding the interaction of secondary flows with film cooling in the turbine is significant to gas turbine designers. Dominant flow features of secondary flow are convected vortices in the mainstream, endwall crossflow, and suction and pressure legs of the vortex formed at the passage leading edge.

Table of Contents

List of Figures

List of Tables

Nomenclature

Symbols

BR	coolant blowing ratio	
C	chord length	m
C_{ax}	axial chord length	m
D	hole diameter	m
DR	density ratio	
g	local acceleration due to gravity	m/s^2
h	heat transfer coefficient	$W/(m^2K)$
M or M_h	Coolant blowing ratio	
P	pressure	Pa
MFR	coolant mass flow to mainstream mass flow ratio	
Q	volumetric flow rate	$m^{3/}s^1$
Re	Reynolds number	
Sh	Sherwood number	
Tu	turbulence intensity	
T	temperature	K
θ	recovery temperature coefficient	
U	velocity component in x direction	m/s
X	passage axial direction	
y	displacement of distance	m
Y	passage pitchwise direction	
Z	passage spanwise direction	

Greek

β	hole orientation angle	∘
ρ	density	kg/m^3
υ	kinematic viscosity, μ/ϱ	m^2/s
μ	dynamic viscosity	kg/ms
δ	boundary layer thickness at $U=U_m$	m
δ_1	displacement thickness	m
δ_2	momentum thickness	m
Δ	difference operator	
η	film cooling effectiveness	

Subscripts

avg	average
ax	axial direction
cali	calibration
c	coolant
h	hole
m	approach flow evaluated in the freestream at the outer edge of the boundary layer

Abbreviation

CRVP	Counter Rotating Vortex Pair emerging from jet in crossflow
DNS	Direct Numerical Simulation
IR	Infrared thermometer
LES	Large Eddy Simulation
PLIF	Planar Laser-Induced Fluorescence
PIV	Particle Image Velocimetry
MRC	Magnetic Resonance Concentration
MRV	Magnetic Resonance Velocimetry
RANs	Reynolds-Averaged Navier–Stokes
TLC	Thermochromic Liquid Crystal
VG	Vortex Generator

Chapter 1. Introduction

1.1 Motivation

Gas turbine usage is widespread for propulsion and power generation. The fundamentals of gas turbines are explained briefly. Ambient air passes through a compressor to increase its pressure. Then, heat is added to the high-pressure air in a combustion chamber. The hot, high-pressure air is then expanded through a turbine, powering the compressor. Excess power from the turbine produces shaft work for power generation. Alternatively, a nozzle is positioned downstream of the turbine, or downstream of a fan of the power shaft, to generate thrust for propulsion. The schematic of the gas turbine engine is shown in Figure 1.1.

Because energy demands are increasing faster than non-renewable energy sources can supply, the need for pushing highly efficient and reliable gas turbine engines is rising. Classical thermodynamics reveals that higher turbine inlet temperatures are needed to enhance the turbine power output and to increase the energy efficiency for the turbine. Thermodynamics considerations are not the only governing factors; material requirements and other design constraints should be considered. Though new concepts such as ceramic materials have been proposed for achieving higher temperatures before failure, in practice, many of these concepts are not currently mechanically robust enough for turbomachinery.

Turbine blades are cast from superalloys, which have brilliant mechanical properties. Nevertheless, modern turbine inlet temperatures have risen to levels at or even above the failure temperatures of such advanced superalloys. Thus, the only possible design is one with careful consideration of the turbine cooling: typically, and an addition of internal and external cooling applied on the surfaces that require protection. High-pressure cooling air is readily available in the engine for use as cooling fluid by taking compressor exit air and bypassing the combustion chamber. The coolant air is routed to key cooling locations, as shown in Figure 1.2.

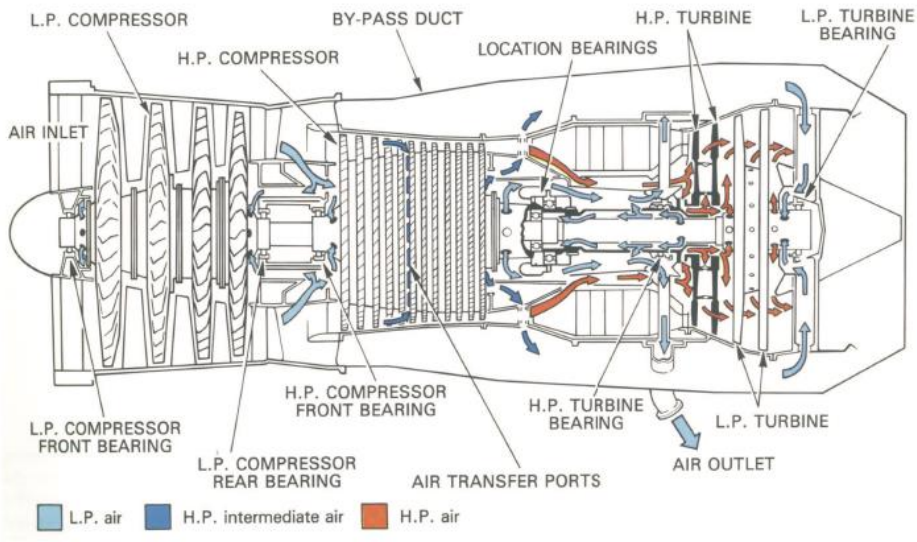

Figure 1.1: Gas Turbine Engine (Rolls-Royce, 1986)

A primary external cooling method that is widely applied is film cooling. Coolant air is ejected through the surface and provides a protective film of coolant between the hot working fluid and the turbine passage surface. Film cooling techniques are applied on the nozzle guide vanes, rotor blades, and on the vane and blade endwall surfaces, as pictured in Figure 1.2. These are particularly significant in the first few turbine stages where the working gas is at its highest temperature. The radial temperature profile of the gas exiting the combustor (upstream of the turbine) is approximately parabolic, and a high thermal load is found on the stator vane and rotor blade surfaces. Thus, many works had focused on these surfaces. Recently, the temperature profile has been further flattened, with combustor redesign aiming at reducing emissions and enhancing combustor mean exit temperatures (Simon, et al., 2008). Because of these recent advances, an increased heat load is seen on the turbine endwall and more research must be invested to endwall film cooling.

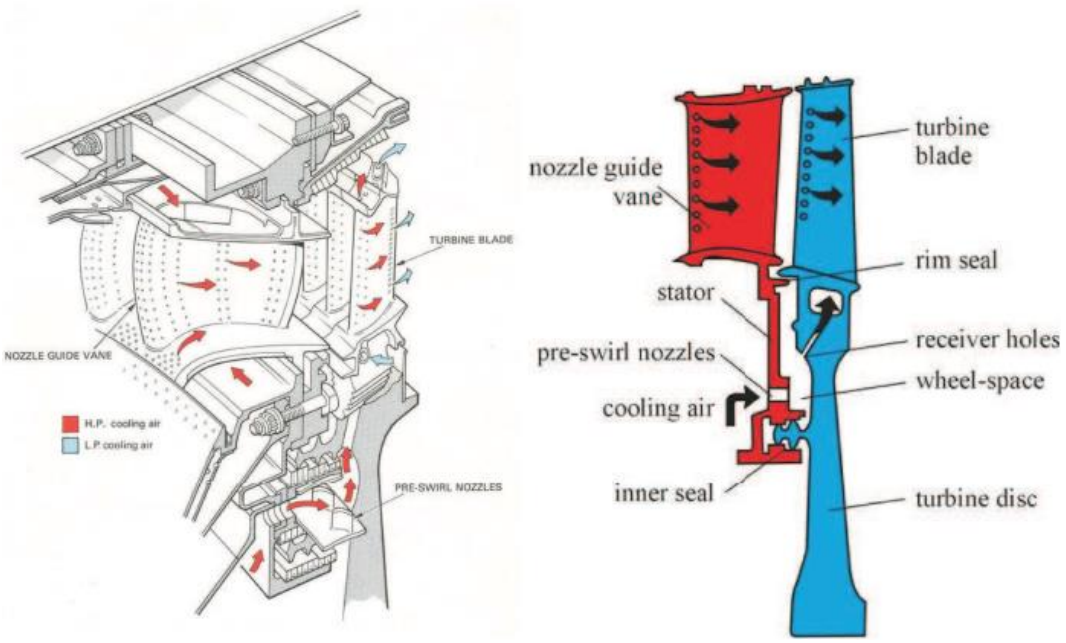

Figure 1.2: Passage Film Cooling (Rolls-Royce, 1986)

Endwall region cooling remains a challenging issue due to the complex secondary flow features in the passage. A description of secondary flow patterns in the turbine is shown in Figure. 1.3. The difficulty is to cool near the leading-edge stagnation point of the endwall and throughout the passage on the endwall surface near the pressure side. This is because of secondary flows, particularly the pressure leg of a horseshoe vortex (to be discussed later) generated at the airfoil leading edge and passing around the pressure side of the airfoil. This pressure leg sweeps the coolant away from the wall and causes mixing between the working fluid from the combustor toward the endwall surface. In addition, there is a challenge because of mixing by secondary flows, particularly in the endwall crossflow and downwash regions of the pressure leg of the horseshoe vortex. This further strengthens the endwall crossflow. The crossflow sweeps coolant from the pressure side toward the suction side along the endwall, resulting in a more difficult cooling situation on the downstream part of the passage near the pressure side.

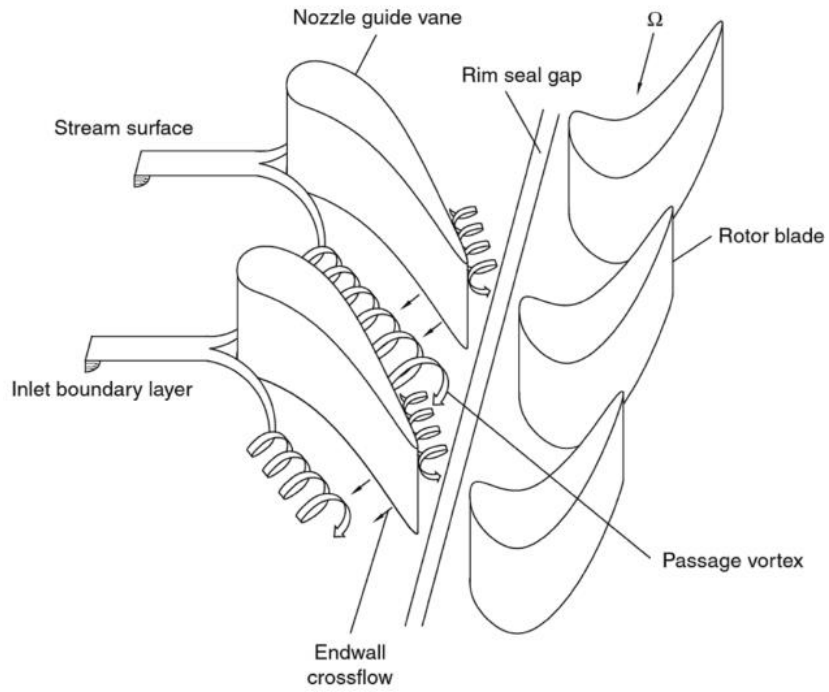

Figure 1.3: Nozzle Vane and Rotor Blade Endwall Flows (Childs, 2010)

Coolant injection upstream of the passage

The primary means to reach endwall full coverage film cooling is injection of coolant upstream of the passage on both the stator and rotor turbine stages.

In the stator, recently, upstream coolant injection, from the passage inlet (Ornano & Povey, 2017) or the combustor-turbine interface (Nawathe, et.al, 2023), has been proven to thicken the inner layer of the near-wall turbulent boundary layer flow, if the injection momentum ratio (coolant momentum to passage flow momentum) is sufficiently high. With the energized turbulent boundary layer flow, upstream coolant injection can penetrate the passage flow, reach the rear part of the pressure side surface, and impinge on the pressure side surface, an area that has been considered particularly challenging on effective film cooling.

In the rotor, purge flows of coolant injected upstream of rotor platform are used as cooling sources for the endwall. The purge flow is applied to purge the wheel space of hot gas or to prevent ingestion of hot gas into the stator-rotor gap that could damage turbine disk components. Ideally, purge flow, if applied properly, possesses the potential to cool the endwall surface. The coolant path is shown in the Figure 1.4.

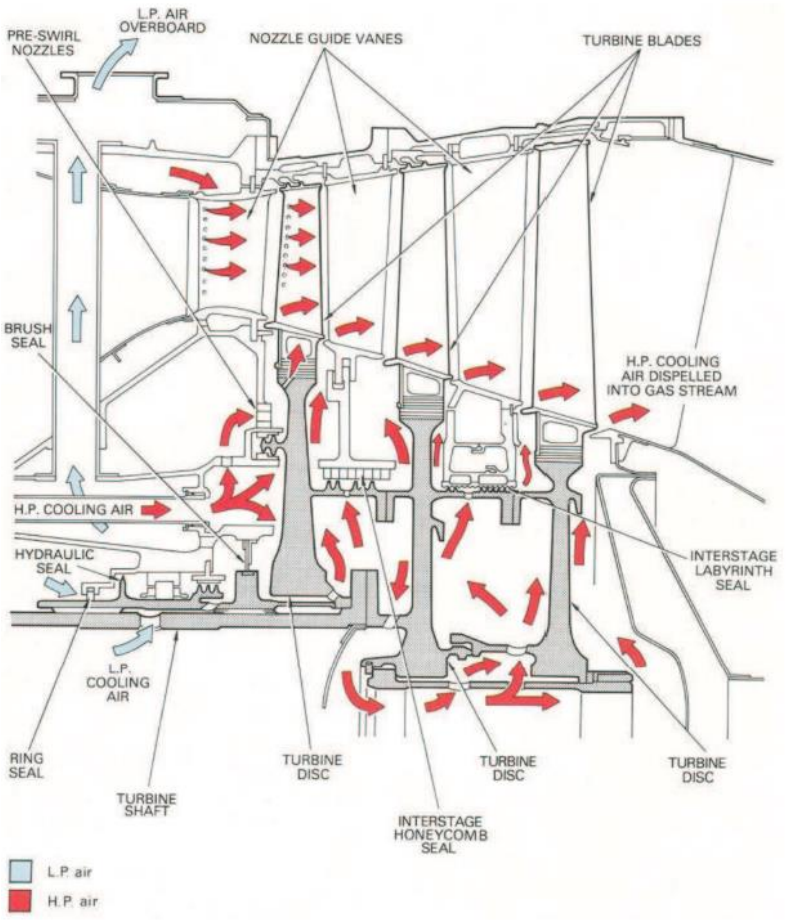

Figure 1.4: Wheelspace Coolant Flow Paths (Rolls-Royce, 1986)

In reality, relative motion between the stator and rotor should be considered. This motion leads to a swirling flow effect (rotational effect) that directs coolant from the pressure side of the endwall surface toward the suction side of the surface. As a result, the pressure side of the endwall is more challenging to cool by injection of purge flow coolant. When designing the endwall cooling scheme in a turbine blade passage, it is crucial to consider the relative swirl when designing endwall film cooling schemes, as purge flow between the rotor and stator might be insufficient for adequate film cooling coverage on the endwall surface.

Discrete hole coolant injection on the turbine endwall

Due to the difficulty in cooling the endwall with purge flow alone on the rotor platform, discrete holes are added, positioned throughout the passage, particularly on the pressure side to achieve adequate film cooling. Typically, the axes of the discrete holes are aligned with the local endwall flow velocity, to reduce mixing (enhancing heat (mass) transfer coefficients and reducing film cooling effectiveness). This may not always be practical, due

to manufacturing constraints, so the discrete holes may lead to injecting coolant with misalignment of the local endwall flow velocity.

Because of manufacturing constraints, the effects of discrete hole injection direction were recently investigated by Stinson (2019). A schematic of the two tested discrete hole geometries is shown in Figure 1.5. The discrete hole plates feature 15 discrete holes distributed uniformly throughout the endwall surface of the turbine, and arranged in two ways:

(1) Parallel scheme. The 0° plate layout angles the holes in the same direction as the local near-wall flow.

(2) Perpendicular scheme. The 90° plate layout angles the holes with 90° offset relative to the 0° plate.

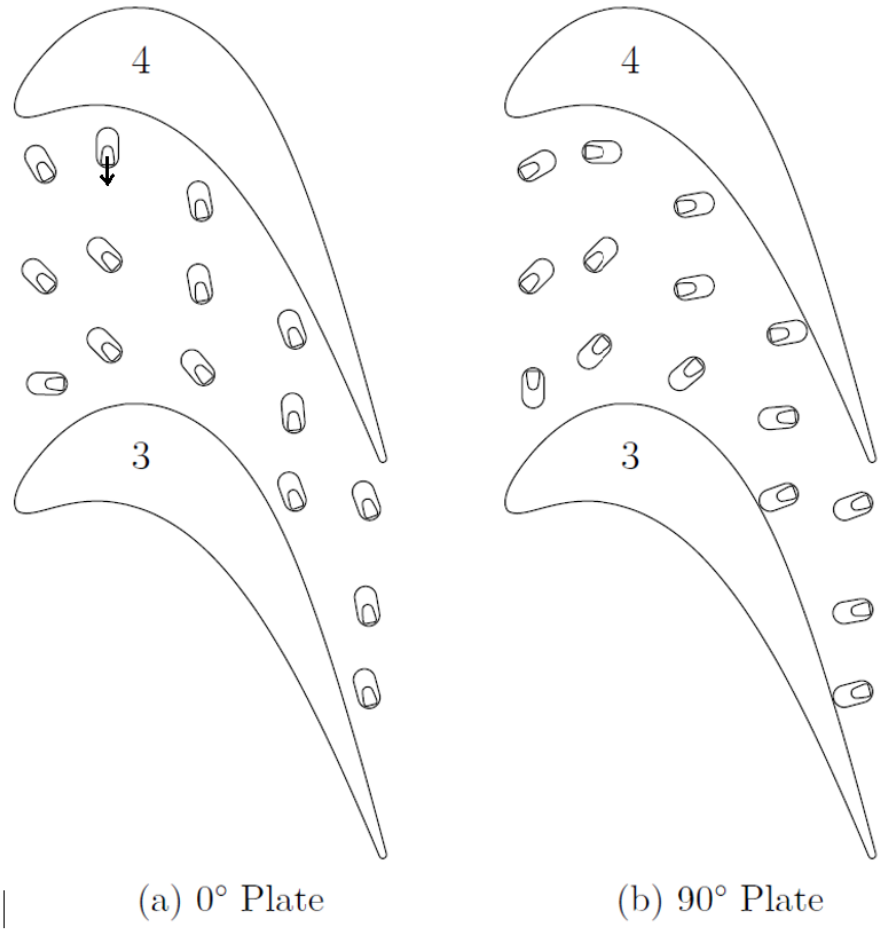

Figure 1.5: Discrete hole Locations. (a) Parallel scheme. Holes were oriented in directions for which injection flow is aligned with the boundary layer flow. (b) Perpendicular scheme. Hole was rotated 90°relative to the first geometry. (Stinson, 2019). The arrow shows coolant discharge direction for one of the holes.

Results show that significant cooling penalties occur with this injection regarding both the mass transfer (enhanced) and the film cooling effectiveness (diminished), indicating that the discrete hole injection misalignment penalty should be avoided if possible. In addition, the angle misalignment effect leads to enhanced mixing and coolant blowing through the boundary layer, which explains the mass transfer and film cooling results.

However, as shown in Figure 1.6, while misaligned discrete hole injection led to substantially decreased peak film cooling effectiveness values, only a moderate reduction in averaged film cooling effectiveness was found overall within the passage downstream (x/Cax>0.5). Furthermore, an even more interesting pattern is upstream in the passage (x/Cax<0.5), where film cooling effectiveness values of the perpendicular (90°) scheme exceed those of the parallel (0°) scheme.

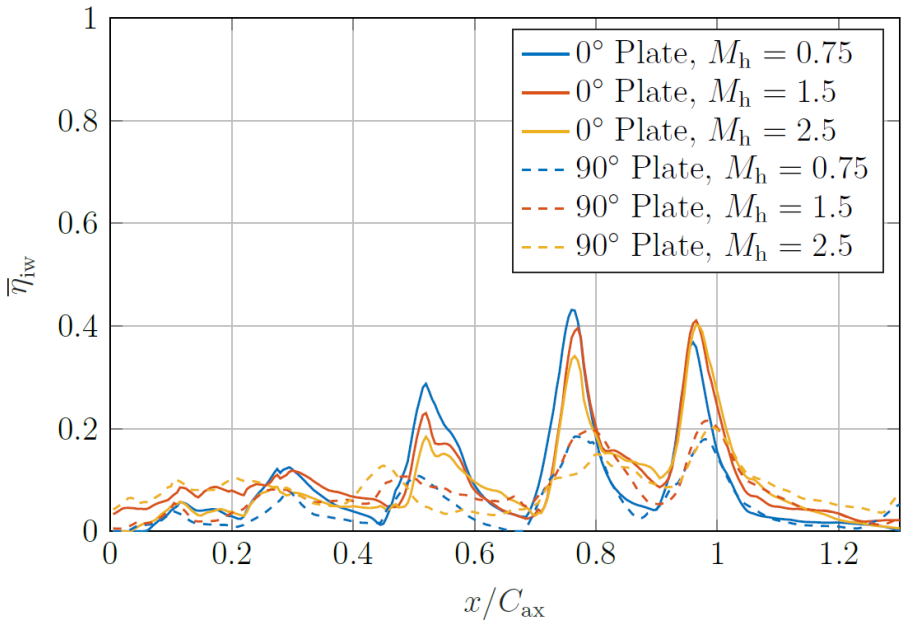

Figure 1.6: Pitchwise-averaged film cooling effectiveness for discrete hole film cooling on the turbine endwall. (Stinson, 2019). Mh is the coolant blowing ratio. η_{iw} is the area-averaged wall film cooling effectiveness

Due to enhanced mixing, one will expect coolant flow to blow off the boundary layer when leaving the hole exit at the injection into the passage flow point. The coolant flows disperse more widely on the surface, leading to a larger downstream film cooling area and only a moderate reduction in film cooling effectiveness value. Overall, the mechanism of "mixing" within the coolant injection flow and external (passage) flow on the endwall surface in the turbine is insufficient to explain the dispersal, spreading, and migration of coolant injection flow from the discrete holes. The spreading of coolant flow with external

(passage) flow is inconsistent at various locations of the endwall surface, indicating that the process of mixing is strongly dependent on the location of discrete hole injection holes on the turbine endwall and the locations of local features of the external (passage) flow.

Studies like the discrete hole placement study of Stinson (2019), revealed the value of distributed discrete holes uniformly placed throughout the endwall surface of the turbine. Unfortunately, such studies are scarce in the current literature. The locations for optimum placement of discrete injection holes on the endwall surface are highly dependent on specific needs to cool the endwall as judged by the gas turbine industry. Typically, due to cost, these discrete hole studies do not cover the entire surface. Thus, mixing between the coolant flow injected from discrete holes and the external (passage) flow on the endwall surface must be explained by extraction of more information than from a single study.

1.2 Objectives

The goal of this thesis is to 1) explain the spreading of coolant flow downstream of the film cooling injection points with various choices of locations of injection on the endwall surface and 2) describe the physics behind the "mixing" within the coolant injection flow and passage flow on the turbine endwall. Such topics require careful consideration of passage flow on the endwall of the passage of the turbine and of the coolant injection flow from the discrete holes.

A single study of endwall discrete hole film cooling is insufficient to describe the physics behind mixing of coolant flow and passage flow. One will expect different spreading processes at various locations on the endwall in the turbine. Thus, more than one study is covered herein, including Stinson (2019), Yang, et al. (2018), Barigozzi, et al. (2005), and Colban, et al. (2008). These studies are extracted from the literature and expected to provide a comprehensive viewpoint for discrete hole film cooling at various locations on the turbine endwall. Such surveys will first include concise literature review of the passage flow in the turbine, coolant injection flow from discrete holes, discrete hole film cooling on the turbine endwall, and the recent works by Stinson (2019) taken at the University of Minnesota. Overall, this discussion covers the spreading of coolant injection flow by passage flow in the turbine passage at various locations of the endwall surface. Also, this study is the first to gather these materials from the literature in an organized way. It is expected that the survey of literature in this thesis can serve as a baseline for follow-on research in the topic of discrete hole endwall film cooling. Review of literature is covered

in Chapter 2, and is presented as a conference paper (see Chen et al. 2024)

Furthermore, within previous reviews of the literature, this thesis points out several avenues of flow on the turbine endwall, observing previously unidentified phenomena that require further study for the entire gas turbine community. To resolve this, this thesis further models unknown phenomena and physical processes that had not been previously thoroughly discussed. A theory about vortical interactions is proposed to describe the spreading, dispersing, and migration of coolant injection flow on the turbine endwall. Such theory is first proposed in Chapter 2.4, and further detailed in Chapter 7.

To prove the credibility of the proposed theory about vortical interaction, and to promote it to the gas turbine community, this thesis applies the theory to explain the evidence about unknown phenomena that had been addressed in the literature, and support its credibility. This theory was presented in the gas turbine conference and was recognized by the audience in that presentation. Details about the validation of this theory by reference to the literature can be found in Chapter 7. The referenced conference paper (Chen et al., 2024) can be found in Appendix A.

To validate the proposed theory by measurement, this thesis experimentally characterizes the spreading process behind the coolant injection flow and external flow in the turbine passage. Such measurements model the corresponding flow physics in the turbine cascade, designs an experiment to reproduce these flow physics in the available test facility (the flat plate in a wind tunnel), and characterizes the spreading of coolant by detailed thermal measurements. The design of the experiment may be the first to frame the research question in the present way. In general, the measurements will further validate the credibility of the theory about the spreading of coolant, as proposed in this thesis. In addition, the measurements documented in this thesis had not been previously done and are valuable in their own. It can validate the quality of physics simulation and may provide some hints of unsteadiness within the mixing process of coolant spreading. Details about the measurement can be found in Chapter 8.

Chapter 2. Literature review

The purpose of this section is to discuss the flow in real turbines where passage secondary flow features and coolant injection flow features must both be considered. Focus is on the effects on coolant coverage. This is a tall order, but some aspects and portions of the endwall film cooling situation can be discussed using support from focused experiments and computation that relate to the various features discussed above. This serves as the beginning of a model for describing endwall coolant coverage.

2.1 Secondary Flow

Geometric features that have a major effect on passage secondary flows are the following six:

1) streamline curvature due to airfoil camber,

2) concave (pressure) wall to convex (suction) wall pressure differences due to streamline curvature within the passage,

3) streamwise acceleration of the flow in the upstream portion of the passage due to the decreasing passage flow area in the streamwise direction and endwall contouring and streamwise deceleration of the flow downstream in the passage due to a streamwise increasing passage flow area,

4) Stagnation of the flow on the airfoil leading edge region and the effects it has on the flow near the endwall-leading edge junction. Here, lower stagnation pressure near the endwall than present above the endwall boundary layer drives flow down the leading-edge region to create a vortex in the endwall-leading edge corner (see Figure 2.1 leading edge region).

5) This vortex at the leading edge is carried around the leading edge on both the pressure and suction sides (Figure 2.1, vsh1 and vph1).

6) The pressure-to-suction side pressure gradient and the low momentum of the endwall boundary layer led to migration of the endwall boundary layer fluid from pressure side to suction side of the passage (Figure 2.1, vp1). The higher streamwise momentum within

the passage flow (away from the endwall) prevents this pressure side-to-suction-side migration within the passage.

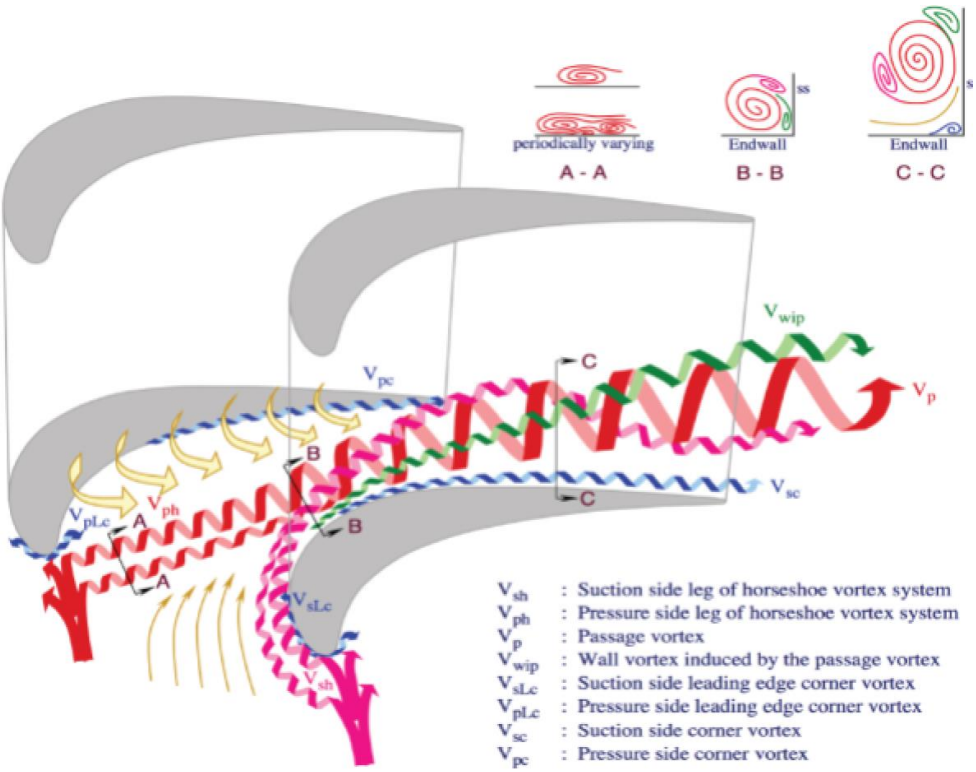

Figure. 2.1: Secondary Flows in Turbine Cascade (Wang, et al., 1997)

2.2 Jet in Crossflow

This section discusses the vortices generated at the film cooling hole as documented in flat plate models for studies of various parameters and the effects of the holes being at different passage locations (see Figure 2.2). Some important parameters are hole geometry, compound angle hole orientation, vortices due to flow interactions, boundary layer thickness, flow turbulence of the approach flow to the hole, streamwise pressure gradient, and local passage flow to hole axis crossflow. The objective for studying these parameters is to achieve clearer understanding to support designs for better film cooling performance. One important item to highlight when using such experimental results is the relationship between a cascade flow representation and a flat plate model. In the flat plate experimental model, it is relatively easy to access the measurement region to document the influences of different parameters on film cooling performance. An experiment on a flat plate, however, cannot simulate important cascade flow features, like the vortices in the passage discussed above. Thus, results from a flat plate model are inherently more difficult to relate to engine behavior. To address this mismatch,

parameters are modeled by attempting to replicate actual secondary flow field features found at the separate locations in the cascade, or turbine passage. An example is an embedded vortex in the approach flow to a single hole under study.

In the following, individual discussions of the different parameters are presented. Then, a realistic flow environment in the turbine cascade (a realistic engine situation) having more than one effect is discussed. Thus, single effects are first introduced, then discussions of multiple effects are offered. Modeling the simultaneous interactions of two or more parameters requires thoughtful modeling of the system while considering engine passage flow physics.

2.2.1 Counter-rotating vortices at the coolant hole

The discrete-hole geometry and the jet-to-approach-flow fluid dynamics lead to three-dimensional flow and temperature fields around and downstream of injection slots or holes. Jet lift-off, high turbulence intensity in the shear layer, and counter rotating vortex pairs are important features to consider. Furthermore, counter rotating vortices are inherently inclined to leave the surface due to the upwash secondary flow vector on the center of the vortex pair. Goldstein et al. (1968) was among the first to discuss counter rotating vortices in film cooling (as depicted by Figure 2.2). They studied coolant flow entering through a circular hole at an angle of 35 deg to the surface. Their results show that, as the jet of fluid leaves the hole, it retards the main flow along the upstream side of the jet causing increased pressure there, and reduces pressure downstream of the jet. This pressure difference provides the force that deflects and deforms the jet. Circulatory motions shown in Figure 2.2 are caused by intensive mixing of the two flows. The deformation of the jet is strongly affected by the blowing rate parameter (the ratio of blowing mass flux to approach flow mass flux). In general, the injected fluid penetrates farther into the passage stream when the blowing parameter is larger.

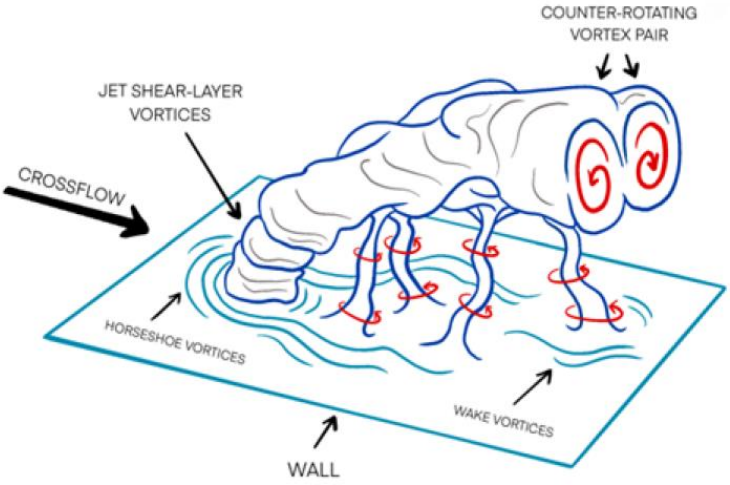

Figure 2.2: Vortical features of a jet in crossflow, as depicted by Fric and Roshko (1964)

2.2.2 Shaped holes

A shaped diffuser hole oriented in the streamwise direction decreases jet penetration into the mainstream, increases lateral spread of coolant on the endwall, and increases film cooling performance. Such a diffusion hole was first proposed by Goldstein, et al. (1974) to increase surface film cooling performance by reducing jet penetration to the mainstream. Various means have been sought to reduce penetration of the coolant jet while increasing lateral spreading to improve cooling over a wider region between holes. A means for doing so is to widen the departure area of the hole from that of the metering section (minimum flow area section that controls the cooling fluid flow rate). Prior film cooling studies used cylindrical and uniform cross section holes. When the geometry near the film cooling flow channel exit is altered by increasing the exit area (shown in Figure 2.3), improved film cooling effectiveness is attained. It is expected that by altering the passage at the hole exit, a Coanda effect is created, which induces the emerging fluid to follow the surface rather than depart from the surface and penetrate the passage flow. Various other geometric and fluid dynamics parameters can affect the performance of discrete hole film cooling, such as hole spacing to diameter ratio, length of hole to hole diameter ratio, other shape features of the hole, inclination angle with the surface to be cooled, skewing of the hole relative to the flow giving compound angle injection, surface curvature, and surface smoothness. Fluid dynamics parameters that were varied in such studies include blowing rate (ratio of coolant mass flux to passage mass flux), momentum flux ratio (coolant momentum flux to passage flow momentum flux), density ratio (coolant to passage density), velocity ratio (coolant velocity to passage average velocity at the hole exit), free-stream turbulence intensity and

turbulence length scales of the coolant flow and passage flow, and streamwise pressure gradient.

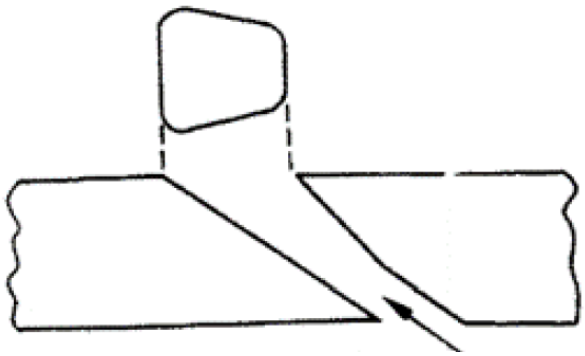

Figure 2.3: A cylindrical hole with a shaped diffuser. Projected area is shown above the hole (Goldstein, et al., 1974)

2.2.3 Compound angle hole

This section aims to understand film coverage with discrete hole injection within the passage in an actual setting. It is known that the approach flow direction upstream of a film cooling hole can be skewed from the hole centerline direction due to various effects in the passage, such as pressure-to-suction-surface crossflow and the horseshoe vortex system. When the film cooling hole is misaligned with the approach flow (a compound angled hole orientation), one of the vortices in the counter rotating vortex pair behind the hole gains strength at the expense of the other vortex. This continues downstream until there is a single streamwise vortex that dominates the flow field. This is observed for even small crossflow angles. The streamwise leeward vorticity becomes the dominant vorticity downstream of the hole, and by increasing the crossflow angle, it becomes larger and more asymmetric. These features were reported by Schmidt, et al. (1996), Goldstein and Jin (2000), and Age, et al. (2008).

2.2.4 Compound angle injection with shaped hole

More description about the nature of the shaped hole, particularly the effect of a crossflow angle, were reported by Haydt and Lynch (2019) who documented the flow field and presented surface cooling measurements. Measurements with particle image velocimetry at several downstream planes normal to the streamwise direction were reported. Their data (Figure 2.4) show that circulation increases as the crossflow angle increases and the flow field transitions from a vortex pair to a single streamwise vortex. For large compound angles (i.e., 60 deg), the streamwise vortex lifts the core of the jet

off the surface, isolating the coolant from the endwall and decreasing surface film cooling performance downstream of injection. For even the smallest cross flow angle (i.e., 15 deg), the flow field is significantly asymmetric, not only in terms of the vorticity, but also as indicated by the velocity vector field. As the crossflow angle increases from 15 to 45 deg, the streamwise vortex increases. Overall, as the compound angle increases, the magnitude of streamwise vorticity increases, becoming more asymmetric. This pattern was reported by Zamiri and Chung (2021).

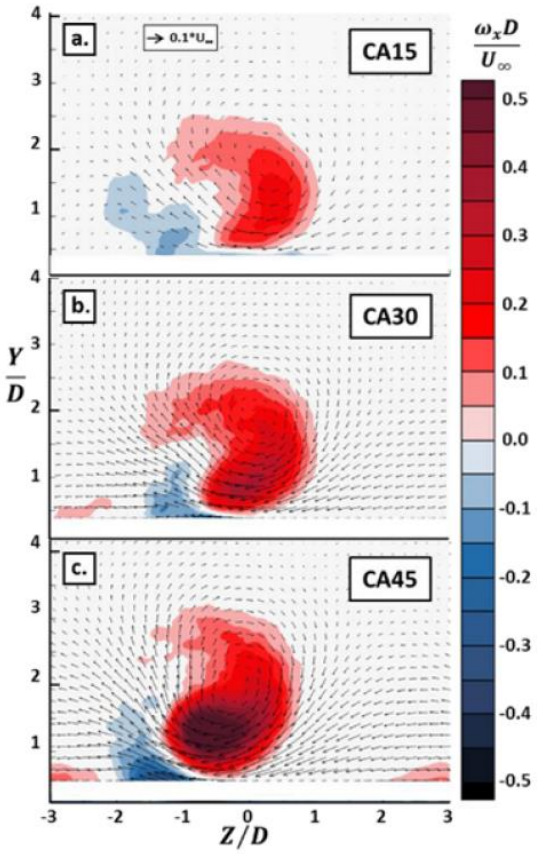

Figure 2.4: Normalized x-vorticity contours for a range of compound angles (indicated in insets, e.g. CA45) at a mass flux ratio of 3.0. Taken at 5 diameters downstream of the hole centerline. The vorticity is overlaid with vectors of in-plane velocity Haydt and Lynch (2019).

2.2.5 Effect of upstream vortex

Embedded vortices (produced by a vortex generator) interacting with a counter rotating vortex pair created by a jet in crossflow have been described in the literature. These cases replicate the complex secondary flows in an endwall passage, including horseshoe vortices, passage vortices, and the corner vortices, as described previously,

interacting with film cooling jets. Near the wall are vortices embedded in the endwall boundary layer flow. Studies of isolated effects contribute to understanding the interaction of the horseshoe vortex system and the counter-rotating vortex pair generated by film cooling injection. This simulation is relevant to the section upstream of the passage throat where the boundary layer flow (with embedded vortices) has not separated from the endwall. The effect of an embedded vortex and its interaction with the counter-rotating vortex pair was reported by Ligrani, et al. (1989). They measured temperature, velocity, and dimensionless heat transfer coefficient (Stanton number) distributions to show the effects of embedded vortices on film cooling with either in-line or compound angle injection of cooling fluid. Their results show how coolant is disrupted by the vortices. Chung, et al. (2009) studied the effects of embedded vortices produced by a vortex generator on film cooling with various compound angles (inclination and orientation). The study documented the vorticity field over compound angles of zero to 60 deg with two coolant mass flux to passage mass flux ratios of 1.0 and 3.0. The heat transfer coefficient was shown to vary remarkably according to relative positions of the vortex to passage secondary flow features and vortex rotation direction. The data are presented in Figure 2.5. Figure 2.5(b) shows time-average velocity fields of the vortex and the secondary flow when the attack angle of the vortex is 20 deg (as shown by Figure 2.5(a)). The vortex consists of upwash and downwash regions.

In the downwash region, the momentum boundary layer becomes thin since the secondary flow induced by the vortex moves to the wall. In the upwash region, coolant is separated from the wall and is swept away and dissipated by the vortex. Recently, Cui, et al. (2022) reported the destructive mechanism on film cooling performance of a near-wall vortex on the endwall for cases with coolant to passage mass flow ratios ranging from 0.5 to 2.5. The near-wall streamwise vortex intensifies mixing of the hot gas and coolant flows. Film coverage areas vary remarkably with changes in position of the streamwise vortices. As shown in Figure 2.6, for the no-vortex case, two vortical structures with opposite rotation directions are generated when the mainstream interacts with the coolant jet. A pair of kidney-shaped vortices appears separately over the hole's lateral plane.

Figures 2.6(b)–2.6(d) correspond to streamlines and coolant distributions for the MVG case (middle vortex generator), LVG (lower) case, and RVG (right) case, respectively. The development of the kidney vortex is hindered and the kidney vortex in the downstream direction almost disappears. The kidney vortex causes an upwash to

separate the coolant jet from the film that resides in the upwash region where the coolant is drawn into the mainstream by the streamwise vortex. In the downwash region, the mainstream fluid is drawn into and mixed with the coolant and the cooling effect is greatly weakened. For the LVG case, the endwall coolant flow is in the upwash region as the vortex passes, so the vortex sweeps the coolant jet into the upwash region more effectively than in the MVG and RVG cases. Consequently, the coolant film is extruded to a slender shape in the upwash region of the vortex. With the vortices of the MVG and RVG cases, some distortion of the coolant distribution results from the vortex upwash, but most of it remains intact. Overall, the above studies regarding embedded vortices and counter-rotating vortices provide insight into discussions about the interaction of the horseshoe vortex system and the emerging coolant upstream of the throat (passage minimum area) where the endwall boundary layer flow has not separated. This can be said for cases spanning from the pressure wall to the suction wall.

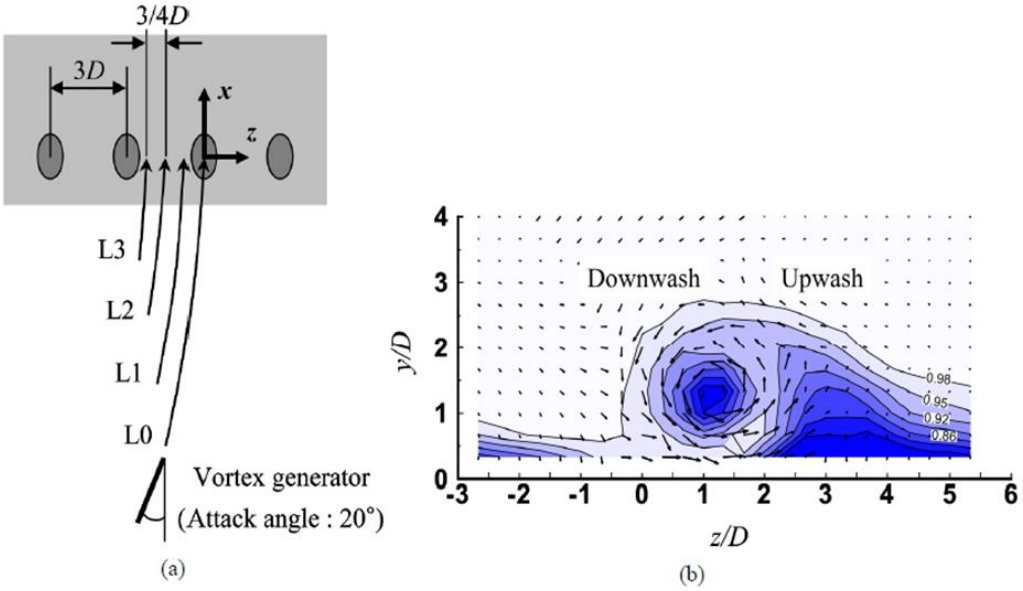

Figure 2.5: Reported by Cui, et al. (2022) (a) Relative positions between the cooling hole and the center of the vortex under rotational directions. (b) Nondimensionalized velocity and secondary flow vectors at x/D=0

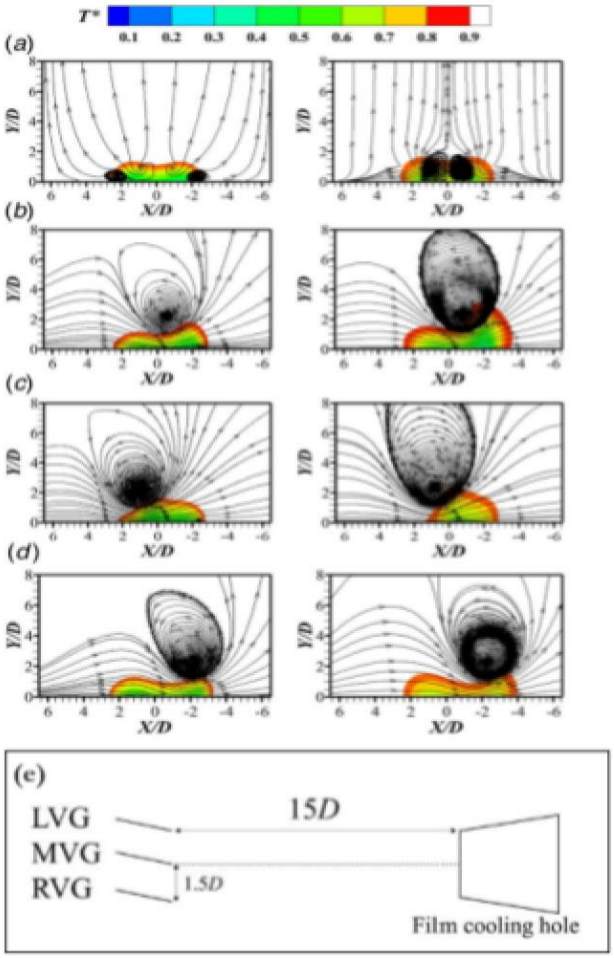

Figure 2.6: Film cooling effectiveness contours and streamlines of four cases of different cross sections. The left column is documented at Z/D=3 and the right column is documented at Z/D = 10 (Z is the downstream distance), M=1.0 studied by Cui et al. (2022)(a) case without vortex generator (b) MVG: vortex generator in the middle (c) LVG: vortex generator on the left, and (d) RVG: vortex generator on the right (e) vortex generator locations.

2.2.6 Effect of crossflow

An additional effect is the pressure-to-suction-surface crossflow. This crossflow is produced by the pressure gradient from the pressure side to suction side of a passage near the endwall. It is especially important downstream of the passage throat (downstream of the three-dimensional separation line), where a new, thin, and accelerating endwall boundary layer flow resides. More details about the three-dimensional turbulent boundary layer are available in Eaton (1995). One research path is to study the crossflow effect on a flat plate model and relate the results back to turbine flow conditions, since measurements near the endwall in a cascade are three-dimensional and unsteady.

Li, et al. (2018) studied the influence of endwall crossflow on shaped hole film cooling performance, both experimentally and numerically. The experimental study was conducted in a curved channel simulating the real turbine environment with blowing ratios over 0.5-2.5. Results show that the crossflow changes the relative positions of the kidney vortices generated at the outlet of the shaped hole. The negative kidney vortices remain on the endwall and decay rapidly downstream. Coolant is driven by the crossflow to migrate in the radial direction.

2.3 Full coverage film cooling with discrete hole injection through endwall film cooling holes

To assist in the discussion of passage secondary flow effects on endwall film cooling, the full coverage endwall data of (Stinson, 2019) are studied. This case presents data that describe the combined effects discussed separately above. Such data apply more accurately to cases with thin approach flow boundary layers (low upstream endwall boundary layer momentum) as seen when the ratio of endwall approach flow momentum to the passage flow momentum is weak (the endwall to passage flow momentum flux ratio is <1.0). As previously noted, a high approach flow momentum flux ratio would lead to a different pattern of secondary flows in the passage, identified as the "impingement vortex," (Alqefl, et al., 2021) and (Nawathe, et al., 2023). Interested readers can refer to studies conducted by Ornano and Povey (2017), Alqefl, et al. (2021), and Nawathe, et al. (2023).

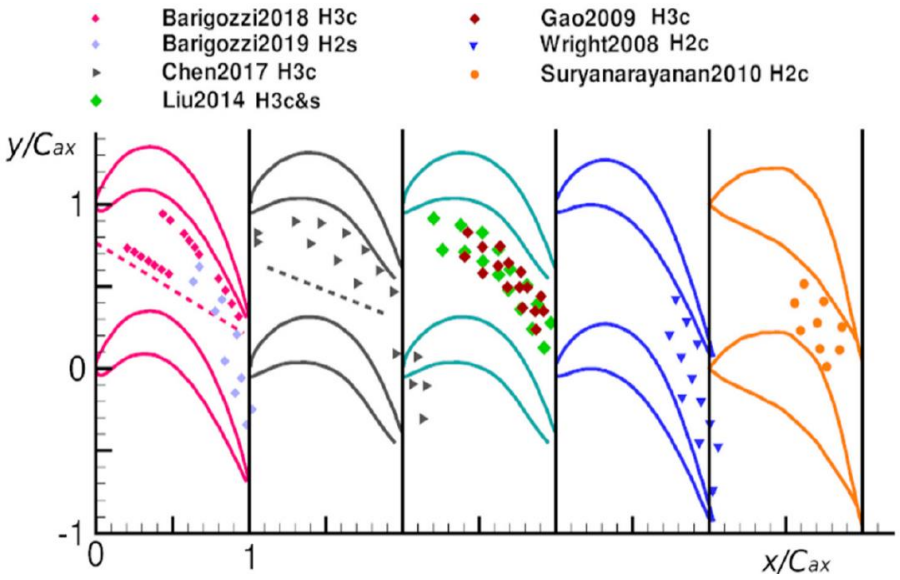

Figure 2.7: A recent review paper the historical placement of discrete hole film cooling across past decades by research groups worldwide, as documented by Barigozzi, et al. (2022)

As reported by Barigozzi, et al. (2022) and shown in Figure 2.7, there has been very little in the literature on discrete hole film cooling of the upstream portion of the passage near the pressure and suction surfaces. This reduced coverage of discrete hole film cooling may be traced to seminal work by Friedrichs, et al. (1999) in which their data suggest that discrete hole film cooling is ineffective in countering the horseshoe vortex near the leading edge of the pressure surface (upstream of the endwall separation line). The leading edge of the pressure surface, therefore, would remain inadequately cooled. Instead, cooling in this region, near the leading edge at the suction surface has been predominantly via upstream slot injection, as pioneered by Blair (1974) and others. This decision led to minimal exploration of discrete hole film cooling in this upstream region. Consequently, little evidence of the effect of lifting of coolant by the suction leg of the horseshoe vortex and the influence of the corner vortex is available in the literature.

2.3.1 Interaction of secondary flow and discrete hole injection at various locations on the endwall

The endwall surface can be divided into different regions, each showing particular endwall film-cooling features:

i) The downstream region beyond the endwall separation line is very close to the pressure side where the jets follow the crossflow driven by the pressure-to-suction side pressure difference.

ii) An upstream region that demonstrates effective film cooling performance on the suction side of the passage as a result of coolant injection through rows of holes or slots upstream of the passage.

iii) The upstream region on the pressure side of the passage, which remains difficult to cool. It is surmised that the horseshoe vortex is one of the dominant features in the upstream region on the pressure side of the passage.

Overall, the literature has a rather complete description concerning discrete cylindrical and shaped holes oriented inline with near-wall velocity vectors within the passage. The leading edge on the pressure side still remains difficult to cool due to the horseshoe vortex at this region. One thing to highlight is that the leading edge near the pressure wall is one of the regions that remains difficult to cool using discrete, round holes. Cylindrical holes near the airfoil leading edge near the vortex lift-off line were introduced

by Friedrichs, et al. (1999). Their findings show that coolant coverage around the blade leading edge is difficult to attain, especially in the vicinity of the leading edge stagnation point. It is expected that the coolant in this region is likely to lift off the surface. In addition, discrete shaped holes on the endwall were studied by Barigozzi, et al. (2005) in a nozzle vane cascade. Their data show that at high injection rates, passage vortex effects tend to become weaker, leading to strong reduction of the endwall crossflow and more uniform flow along the spanwise direction. They showed that the shaped hole is more effective than the cylindrical hole, especially at low injection rates, which increases the cooling performance in the front part of the vane passage. Discrete, shaped holes were further studied by Colban, et al. (2008). Discrete hole axes on the endwall were skewed with the approach flow and the holes were oriented away from the pressure surface (wall).

The case with the highest blowing ratio and several holes near the pressure side in the upstream portion of the passage is shown in Figure 2.8. Ejected coolant from discrete holes located at P2 and P4 lift off the surface as a result of strong secondary flows. Other ejected coolant from discrete holes located at P1, P3, and P5 follow the hole axes due to increased coolant momentum, instead of lifting off by the secondary flows. Though the compound angle discrete cylindrical holes have been thoroughly studied, the compound angle discrete shaped holes on the pressure side and suction side remain poorly understood.

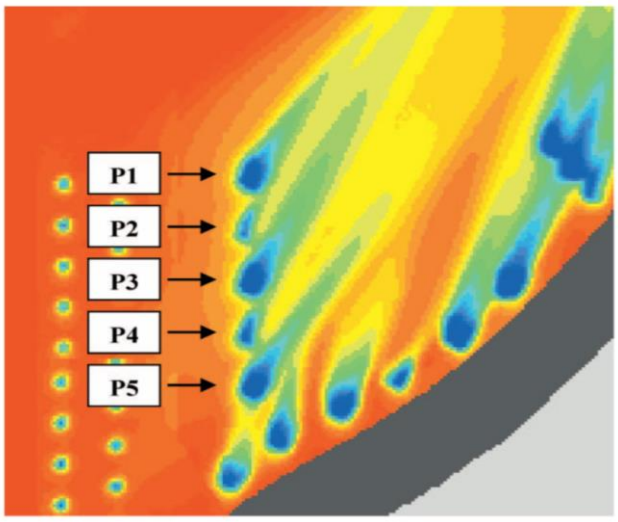

Figure 2.8: Closeup view of region near the pressure side leading edge (baseline 100% case). P1-P5 located holes in this region. Blue represents highest coverage and red represents lowest coverage. Reported by Colban, et al. (2008)

2.3.2 Strategies for cooling the leading-edge region approaching the passage throat

i) Hole location: The coolant should be injected at the downwash location of the secondary flow vortex to constrain coolant to near the endwall region to enable better surface coolant coverage. This relies on proper selection of the discrete hole locations and their orientations with their near endwall approach flows.

ii) Hole geometry: At the downwash part of the horseshoe vortex, asymmetric vortices from discharged coolant should have different coolant rotation than the rotation of the local horseshoe vortex, avoiding merger of these vortices. This requires proper selection of hole geometries, particularly shaped holes, near the surface close to the leading edge near the pressure surface.

iii) Hole orientation: Although ejected coolant is constrained on the surface under the downwash part of the horseshoe vortex, strong coolant vorticity is necessary to resist dissipation of the vortices by viscosity and provide better surface coverage. This requires introduction of compound-angle, shaped holes to produce a more intense asymmetric vortex pair near the surface close to the leading edge of the pressure surface.

2.3.3 Evidence from recent studies

A full-coverage experimental and computational study was conducted by Stinson (2019) using a diffusion shaped hole and full-surface coverage. The compound angle, shaped hole pattern (oriented away from the pressure surface and, in the upstream portion of the passage, the suction surface) these are important additional data to supporting the present study. They show migration of coolant downstream of individual film cooling holes. Surface effectiveness distributions were measured by the naphthalene sublimation technique for three blowing ratios. Single pixel uncertainties for the film cooling effectiveness data are around 5%-10%. Variations across multiple pixels can be described with lower uncertainty, allowing tracking of the coolant discharge plumes.

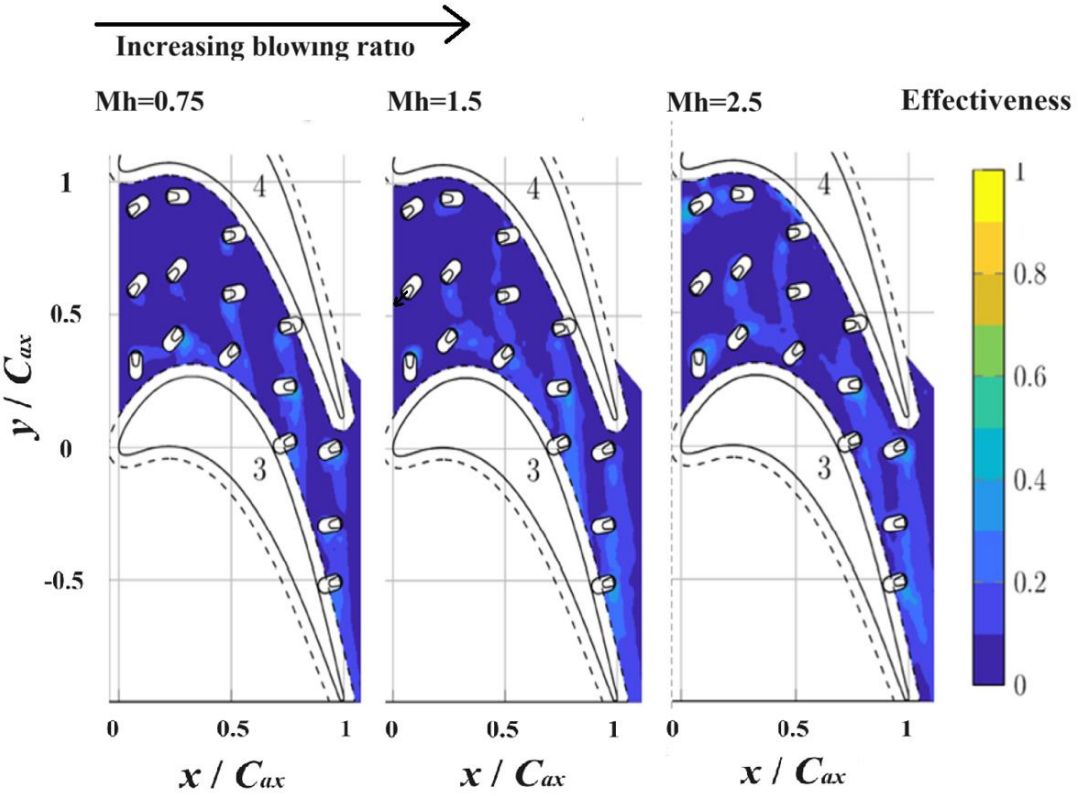

Figure 2.9: Film cooling effectiveness values for the "perpendicular" holes. The coolant average velocity to passage average velocity ratios, Mh, are shown for the three cases, from Stinson (2019). An arrow (upstream hole, center plot) is added to show the coolant exit direction.

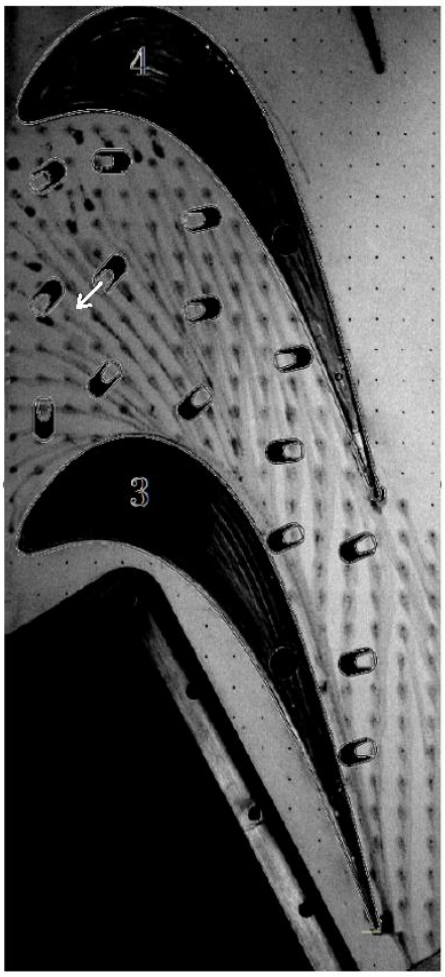

Figure 2.10: Oil dot visualization for endwall surface shear stress direction fields. There was no coolant injection. However, discrete hole injection exit planes from the Stinson (2019) study were sketched by the present author to visualize the hole positions in the study. Turbulence intensity = 4%. Reported by Papa, et al. (2011). The arrow shows the direction of coolant exit flow.

Papa, et al. (2011) performed the oil-dot visualization technique to visualize endwall surface shear stress directions giving guidance concerning near-endwall flow directions in a passage of the Stinson geometry, but without film coolant injection. Figure 2.10 shows results with a 5% approach flow turbulence intensity. In one case of the Stinson dataset, holes were oriented in-line with the apparent near-endwall flow directions in the passage, as given by this technique. In a second case, the holes were rotated so that they were approximately 90 deg to the apparent near-endwall flow direction of each hole (called "perpendicular"). This data set is presented in Figure 2.9. The perpendicular hole case provides more uniform coverage of coolant along the endwall-suction surface junction when the blowing ratio, Mh, is 1.5. A possible explanation is that the coolant energizes the pressure leg of the horseshoe vortex on the suction side of the passage. It is surmised that

this is due to a delay in lift-up of the passage vortex, leading to a weakening of the corner vortex along the suction side. Endwall surface wall shear fields, documented here, and the hole pattern, indicate the angles between the near-wall flows approaching selected coolant holes and the corresponding coolant hole axes (Figure 2.10). As the measured or computed shear fields used for this observation were without holes or coolant injection, these approach flow directions can accurately be applied, typically, to only the most upstream row of holes (upstream of coolant injection).

Pressure surface.

Results from Stinson (2019) show film cooling effectiveness values along the leading edge of the pressure side of the passage. The discrete shaped holes shown and identified with numbers are oriented perpendicular to the approach flow, Figure 2.11. Low surface cooling effectiveness is observed for cases where blowing ratios are 0.75 and 1.5. Here, it is expected that the approach flow is perpendicular to the axis of Hole#1, generating an asymmetric vortex that has similar rotation to that of the pressure leg of the horseshoe vortex, promoting the merging of these two vortices. As previously discussed, this would result in low surface film cooling effectiveness. For the higher blowing ratio case (Mh = 2.5), higher surface effectiveness values are observed surrounding the hole. A potential explanation is that the coolant has larger vorticity and stronger jet penetration with the larger blowing ratio. These are beneficial to retaining more coolant on the surface under the pressure leg of the horseshoe vortex. Apparently, discrete shaped holes here cannot provide enough coolant surface coverage at a low blowing ratio. One other finding is that for the case with the largest blowing ratio (Mh = 2.5), the endwall-pressure surface corner junction has greater film cooling coverage. A possible reason for this is that the ejected coolant is swept under the corner vortex and accumulates there. A complementary study by Yang et al. (2018) for cases where the compound angle holes are oriented toward the pressure surface is documented in Figure 2.12. Their data show higher coolant coverage at the upstream portion of the passage near the pressure surface. It is expected that the vortex generated with coolant ejection is asymmetric and has a different rotational sense than that of the pressure leg of the horseshoe vortex in this region. Overall, the Yang, et al. (2018) and Stinson (2019) studies document both positive and negative compound angles and provide a suggestion that shaped holes introduced upstream in the passage should be strategically located under the passage vortex for better surface coverage.

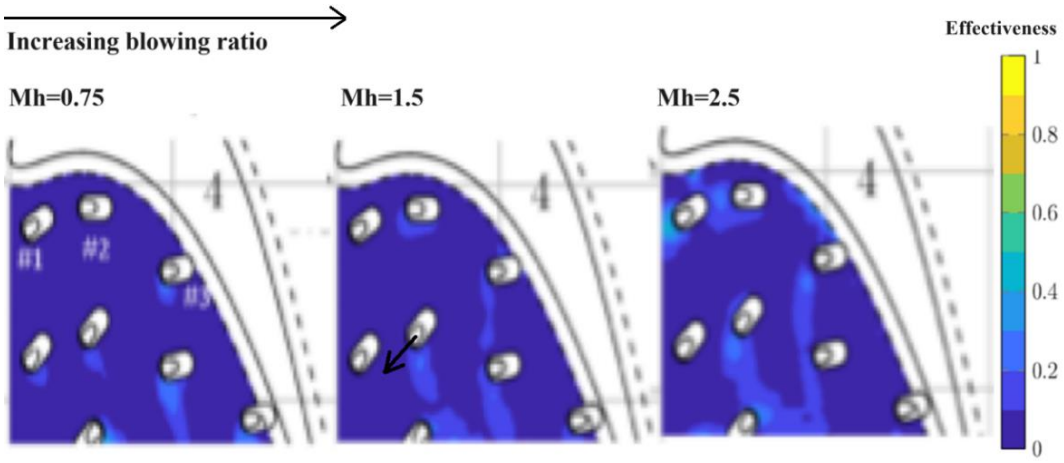

Figure 2.11: Film cooling effectiveness values for the "perpendicular" holes. Pressure side of passage. The coolant average velocity to passage velocity ratios, Mh, are shown for three cases, Stinson (2019). The arrow shows the direction of coolant exit-flow.

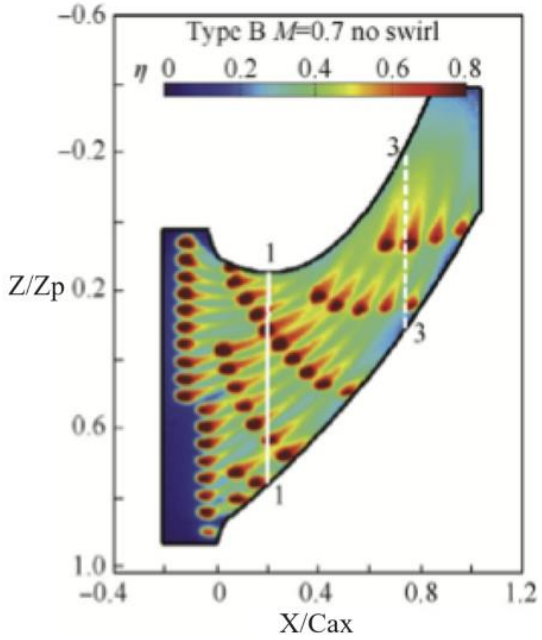

Figure 2.12: Film cooling effectiveness distribution on the endwall (Case for M=0.7). Z, Zp pitchwise, (Yang, et al., 2018)

Suction surface

Data for discrete expansion-shaped hole case of the Stinson (2019) study are shown in Figure 2.13. Of particular interest to this study is the film cooling effectiveness distribution near the suction side of the passage. The approach flow upstream of the holes is documented in Figure 2.14 as computational results overlaid on ghosts of virtual holes. It is expected that the asymmetric vortices from the ejected coolant rotate similarly with the suction leg of the horseshoe vortex. This coolant, as a result, energizes the suction leg of the horseshoe vortex. For the cases with the smaller blowing ratio (Mh = 0.75), ejected

coolant from Hole#11 remains on the endwall surface. A possible explanation for this is that the coolant from the shaped hole has small penetration due to the suction leg of the horseshoe vortex. In the vicinity of Holes #12 and 13, is the location where the suction leg of the horseshoe vortex begins to lift up and off of the endwall. High coolant coverage is found due to a different rotational sense with the pressure leg of the horseshoe vortex migrating from the pressure side to the suction side. Ejected coolant around these two holes located beneath the pressure leg of the horseshoe vortex is washed by the pressure-to-suction wall crossflow, and, possibly, these vortices, and accumulates at the junction between the endwall and suction surface. To explain this, a fluid visualization experiment (Figure 2.15) was conducted by Wang, et al. (2022) in the same wind tunnel and with the same secondary flow system as in Stinson (2019), although the flow visualization measurements were conducted at a very low level of turbulence intensity and low chord Reynolds number. It shows the discrete hole locations and their possible interactions with the suction leg and pressure leg horseshoe vortices. Around Hole#14 (Figure 2.13) is lower surface effectiveness. This could possibly be explained by an intense corner vortex located along the rear part of the suction surface-endwall junction. For a case of Mh=1.5, coolant from Hole#11 and Hole#12 energizes the suction leg of the horseshoe vortex. There, upwash is resisted by the pressure leg of the horseshoe vortex and lifting of the suction leg of horseshoe vortex is delayed. As a result, higher film cooling effectiveness values are observed at Hole#13. Also interesting is that better coolant coverage is observed over x/Cax from 0.5 to 1.0. Also, it seems that the corner vortex is possibly weakened or eliminated. For the case of Mh = 2.5, the higher coolant rate seems to lead to an energized suction leg of the horseshoe vortex. One possible explanation is that this leg leaves the surface at a further downstream location, apparently at x/Cax = 0.75, where improved surface coolant coverage is observed.

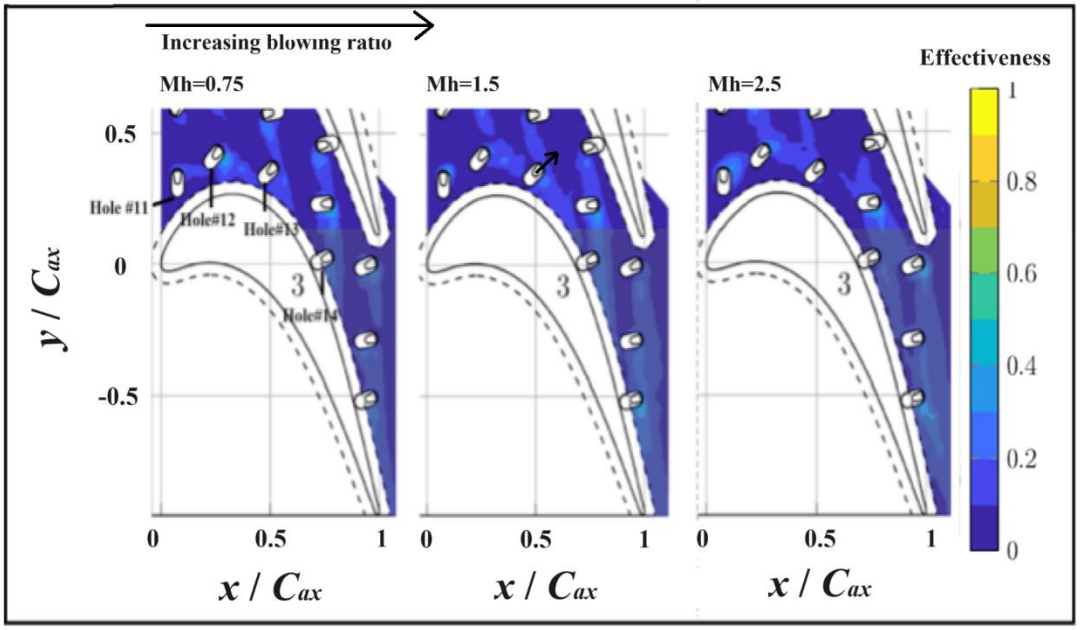

Figure 2.13: Film cooling effectiveness values for the "perpendicular" holes near the suction side of passage. The coolant average velocity to passage average velocity ratios, blowing ratios, Mh, are shown for three cases of Stinson (2019). The hole numbers are identified and the airfoil is the central airfoil #3. The arrow shows the direction of coolant discharge flow.

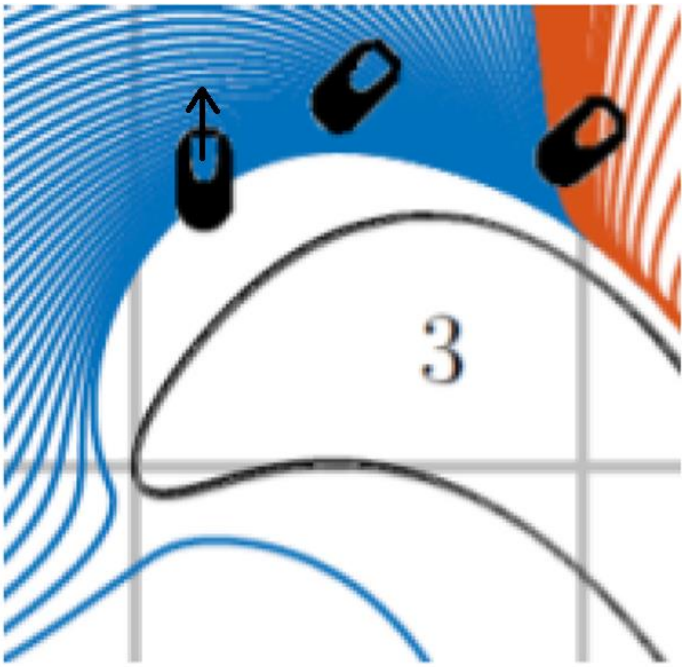

Figure 2.14: Endwall surface streamlines at the suction side, reported by Stinson (2019). The figure shows the outline of the locations of the holes. The airfoil is the central airfoil, #3. The arrow shows the direction of coolant departure flow.

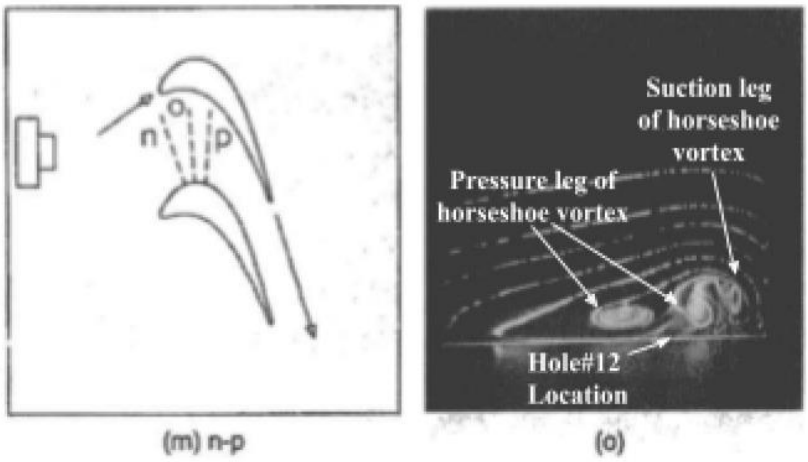

Figure 2.15: Flow visualization (right figure) at the location of plane O (left figure). Reported by Wang, et al., (1997).

2.3.4 Physics of vortex rotational direction

The intent of this section is for further clarify the interaction of secondary flows and discrete hole injection cooling at various locations on the endwall. An area deserving attention is upstream and within the passage throat, particularly near the pressure and suction sides. Discrete hole film cooling data in the literature, and recent new evidence, are used to provide insights into the interacting mechanisms of transport by vortices created by coolant ejection. The predominant other vortex is the horseshoe vortex.

One major finding from the literature is that the relative rotations between the horseshoe vortex and vortices associated with coolant ejection are significant. Studies show merging of vortices with similar relative rotations between the ejected coolant and a nearby horseshoe vortex. Coolant for such cases is swept into the horseshoe vortex, leading to decreased film cooling effectiveness. Such cases are particularly interesting in the upstream portion of the passage on the suction side where the suction leg of the horseshoe vortex resides and merges with the pressure leg of the horseshoe vortex. Here, the passage vortex lifts off the endwall at the suction wall-endwall junction. Recent evidence shows that shaped holes oriented away from the suction surface may delay liftoff of the suction leg of horseshoe vortex and possibly weaken the corner vortex, as documented in Figure 2.13. A possible explanation for this is that the coolant ejected here energizes the suction leg of the horseshoe vortex.

Conversely, vortices with different rotational directional senses between the ejected coolant and the horseshoe vortex, would not merge. Cases like these would restrain the

ejected coolant to the endwall surface, resulting in increased film cooling coverage. Such cases are particularly significant near the leading edge of the pressure side of the passage, an area that is challenging for making coolant coverage due to the presence of the pressure leg of the horseshoe vortex. Recent evidence shows that the distributed, shaped holes oriented toward the leading edge of the pressure surface may retain coolant under the pressure leg of the horseshoe vortex resulting in enhanced film cooling effectiveness performance, as documented by Figure 2.12.

Overall, the literature shows that the discrete hole patterns (geometry, orientation, and the location within the passage), and the vortical interaction within coolant injection vortex and horseshoe vortices should be considered when understanding the effects of a film cooling hole pattern design. Documenting the flow field (including near-hole flows) on the endwall and using that information to determine coolant coverage in a general way is challenging. Presently, coolant coverage is found with experimental or computational documentation of particular settings. Models for generalizing this information require inclusion of all the effects discussed herein which, as noted, is a tall order. However, the material covered here helps our understanding of the processes involved and may lead to a broader perspective on cooling the endwalls of turbine passages.

2.4 Relation to present work

2.4.1 Summary of previous work

In the previous literature review, much attention was devoted to film cooling on the turbine endwall using discrete hole film cooling injection. Typically, in these studies, the discrete holes were placed downstream in the passage near the pressure side of the endwall. Flow is driven by a strong pressure gradient and endwall crossflow results. Thus, upstream of the passage throat (near the pressure side and the suction sides of the passage) discrete shaped-hole film cooling coverage has not been frequently applied and, thus, there is little opportunity for investigating what advantage secondary flows in this region may have. Due to the strong secondary flow residing in the pressure side of the passage, discrete hole cooling injection provides inadequate film cooling coverage, as documented in the current literature. Alternatively, the suction side of the passage is cooled mostly by upstream injection with coolant sweeping toward the suction wall. Thus, because the previous studies considered that injection near the upstream suction side of the passage had little

value, there was a sparsity of discrete hole injection data within the present literature.

Upstream of the passage throat, the major flow features are the horseshoe vortex and the coolant injection vortices (also called jet in crossflow vortices). The difficulty is that there is little opportunity to gain understanding of the interactions of the horseshoe vortex and the jet in crossflow vortices because of lack of data. The nature of the flow physics, three-dimensional and unsteady, is far too complicated for detailed and accurate descriptions with current measurement and computer simulation capabilities. Also, experiments fail because of insufficient spatial and temporal resolution. Spatial resolution is constrained by the characteristic length of the measurements themselves, as the measurements are done in the cascade wind tunnel while wishing to describe flow with coolant injection within the turbine passage. Also, the dimensions of the discrete holes for injection might prevent sufficient documentation due to insufficient spatial resolution. Temporal resolution is constrained by the unsteadiness of the secondary flows in the turbine cascade. This is even more prominent in the mixing layers between the secondary flows and coolant injection flows (jets in crossflow). Finally, RANs modeling fails due to its poor performance in capturing turbulence decay in the passage secondary flows (Nawathe and Simon, 2022) and lateral spreading and jet penetration of the jet in crossflow requires modeling of pressure fluctuations (Mahesh, 2013). LES and DNS models are not practical for such engineering designs due to their high computational cost in simulating the multiple holes involved.

While it seems difficult to understand the detailed flow features for the horseshoe vortex and the jet in crossflow within the cascade wind tunnel, extracting the driving flow features for describing the interactions of the horseshoe vortex and discrete hole injection flows is possible. The key to this is to identify the most important flow physics that drive the mixing processes. From the literature, the vortical effect, particularly the vortex rotational direction, had been identified as important toward describing spreading of coolant in the turbine cascade. Thus, a theory about the vortex rotational direction is proposed, as shown in Figure 2.16. More details about the proposed theory, and further validation of it, can be found in Chapter 7.

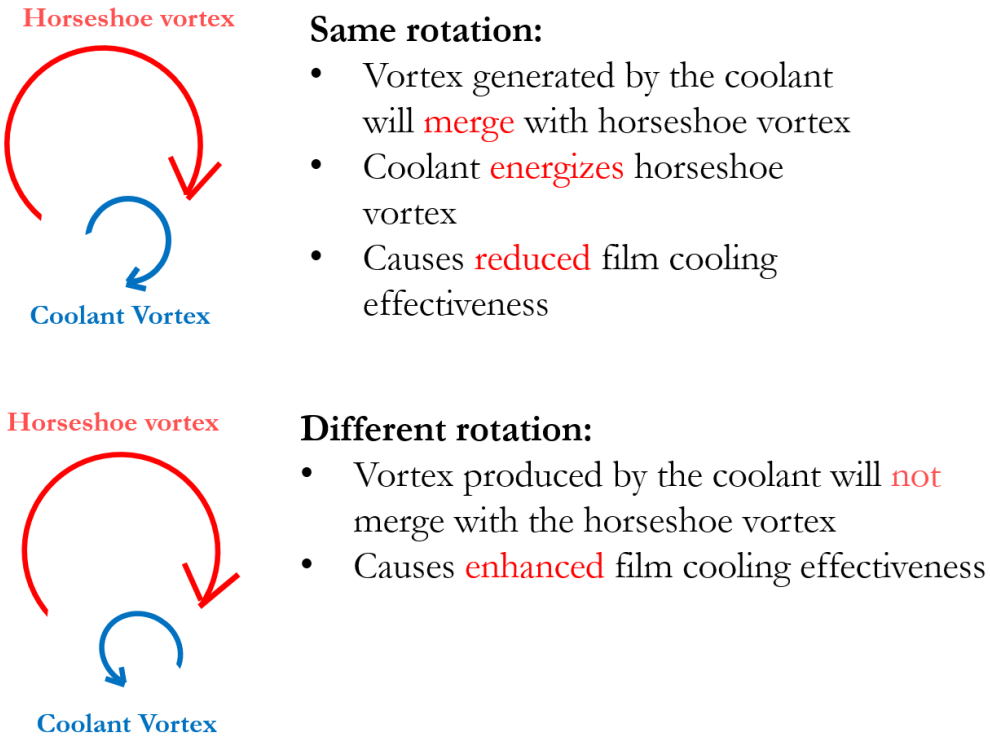

Figure 2.16: Interaction between horseshoe vortex and coolant vortex generated from discrete hole injection.

2.4.2 Present measurements concerning this thesis

Due to the difficulty of taking measurements in the turbine cascade, an alternative is sought to study the vortical effects between the coolant injection vortex and horseshoe vortex on the flat plate wind tunnel. Though many secondary flow features in the turbine cascade are ignored by the modeling, experiments on a flat plate allow taking some information with acceptable spatial resolution about the nature of vortical effects on coolant migration. This simplification provides a chance to assess the nature of vortical interactions in detail and validate the theory of vortical interactions by measurements.

In recent literature, few studies have been devoted to the effects of vortical interactions on coolant migration on a flat plate wind tunnel. Results from Ligrani and Mitchell (1994), Chung, et al. (2009), and Cui, et al. (2022), on flat plate experiments, show relative rotations of horseshoe vortices and coolant injection vortices are critical features to consider. These studies can serve as evidence of vortical interaction of coolant injection vortices and horseshoe vortices in the turbine cascade. Nevertheless, these studies are immature since they are missing in-passage coolant migration with various hole geometries and orientations.

For this reason, this thesis is to experimentally describe the effects of the vortices' relative rotational directions on coolant migration on the flat plate in the wind tunnel as influenced by various hole geometries, orientations, and blowing ratios. The horseshoe vortex is simulated by a longitudinal vortex produced by a vortex generator on the flat plate experiment. It is embedded in a fully developed, thickened, and stabilized turbulent boundary layer. The coolant vortex is simulated by a series of various individual hole orientations producing major asymmetric coolant vortex cores in which the hole axis orients askew to the approach flow direction.

In-passage and near wall coolant concentration measurements are taken by traversing a thermocouple across downstream planes. Also, surface measurements are taken with thermochromic liquid crystal sheets. Time-averaged coolant concentration fields taken by a traversing thermocouple can describe the coolant vortex core characteristics, downstream jet entrainment, and coolant boundary layer growth. The rapid response of coolant migration from the thermochromic liquid crystal sheets provides hints about the unsteadiness of the shear layers and turbulent mixing near the surface.

In general, the present experiment aims to provide coolant concentration data in the passage and on the surface for incoming vortices with misaligned, shaped holes that have not been thoroughly documented in the literature. This measurement will support the descriptions of interactions of horseshoe vortices and coolant injection vortices, particularly with the same and with different senses of rotational direction. In addition, by describing the interaction of vortices with coolant injection, one should be able to describe the coolant trace in the passage and arrange proper discrete hole geometries and orientations on the passage endwall surface, matching with design needs and supplementing upstream coolant injection, where needed.

2.5 Organization of the thesis

Overall, the major contribution of this thesis includes: i) survey of literature of endwall discrete hole film cooling in an organized way. ii) identify avenues for mixing observed and suggested for more study by the community. iii) explain these unknown phenomena with new theory about vortical interactions (explained in the next chapter). iiii) validate the proposed by literature review, presentation in the conference, and measurements.

The work of this thesis is split into different distinct sections:

1. A literature survey about passage secondary flow and endwall discrete hole film cooling in the turbine cascade

2. A theory about the vortex rotational direction between the horseshoe vortex (a crucial feature of passage flow) and coolant injection vortices (a crucial feature of coolant injection flow) generated from discrete hole injections in the turbine cascade

3. A presentation, supported by the literature, of the proposed vortical interaction theory regarding endwall discrete hole film cooling

Results to this point have been documented in an ASME paper (see Chen, et al. (2024)) and presented in a conference (Turbo Expo 2024).

4. Measurements characterizing the effects of vortex rotational direction on coolant migration on a flat plate wind tunnel

5. A validation of vortical interaction in the turbine cascade by detailed coolant concentration measurements on the flat plate

This thesis is organized to explain experimental methods and significant results related to the stated objectives. Chapter 2 introduces a literature review of the work in the field of passage secondary flow features and discrete hole film cooling in the turbine cascade. In addition, discrete hole injection flow patterns, hole orientation effect, incoming vortex effect and crossflow effects are discussed on the flat plate wind tunnel. Chapter 3 outlines the experimental facilities applied in this study. Chapter 4 details the instruments applied to complete the presented experiment. Chapter 5 presents the design of the present experiment and details of coolant concentration measurement. Chapter 6 details the necessary details of the measurement, including the characteristics of the flow, experimental parameter space, qualifications of the experiments, and timescales of on-surface measurements. Chapter 7 discusses the theory of vortical effects in the turbine cascade and further validates the literature. Chapter 8 characterizes the effects of vortical interaction of coolant migration, serving as supporting evidence for vortex interactions in the turbine cascade. Chapter 9 summarizes the key findings of this work and points out a future step to reach full coverage film cooling coverage on the turbine endwall.

Chapter 3. Experimental facility

The experiments for this work were performed in a wind tunnel facility in the Convection Heat Transfer Laboratory at the University of Minnesota. This section details the testing facility, developing approach flow fluid mechanics, and testing piece.

3.1 Wind tunnel

The present experiment was performed in a single discrete hole facility. Passage flow is introduced through a blower, a nozzle, a channel, and a testing section that is open to the atmosphere. The schematic of the wind tunnel is shown in Figure 3.1.

First, air is drawn by a blower in the lab through an inlet filter. The filter is attached at the inlet of a blower to ensure that the air inside the tunnel does not contain damaging debris. This is significant because debris can easily damage the measurement instruments. The blower is a centrifugal fan. The type of this centrifugal fan is LouisAllis, 92245, with a rated power 10HP (7.4W). The blower exit air passes through a diffuser, settling chamber, heat exchanger, a honeycomb section and a screen pack. This heat exchanger was made for previous studies and is not used in the present study. The screens are to break down the flow turbulence and swirl levels. The honeycomb eliminates swirl. Then, air passes through contraction nozzle with an exit cross-section of 71 cm × 11.45 cm. Since turbulence generating grids were not used in the present study, the flow exited the contraction with a low turbulence intensity level and a high degree of flow uniformity.

The mainstream velocity was maintained at a constant value by the rotational speed of a wind tunnel fan. The rotational speed is controlled by a frequency controller, keeping mainstream velocity as a constant value. The frequency range is 0-60 Hz, with 0.1 Hz resolution. The frequency is controlled by a speed controller, connected to a power supply (BK Precision, 1697 DC Power supply), ranging from -5V to +5V. The present experiment was run at 23 Hz, providing a medium level of mainstream velocity of 11.8 m/s.

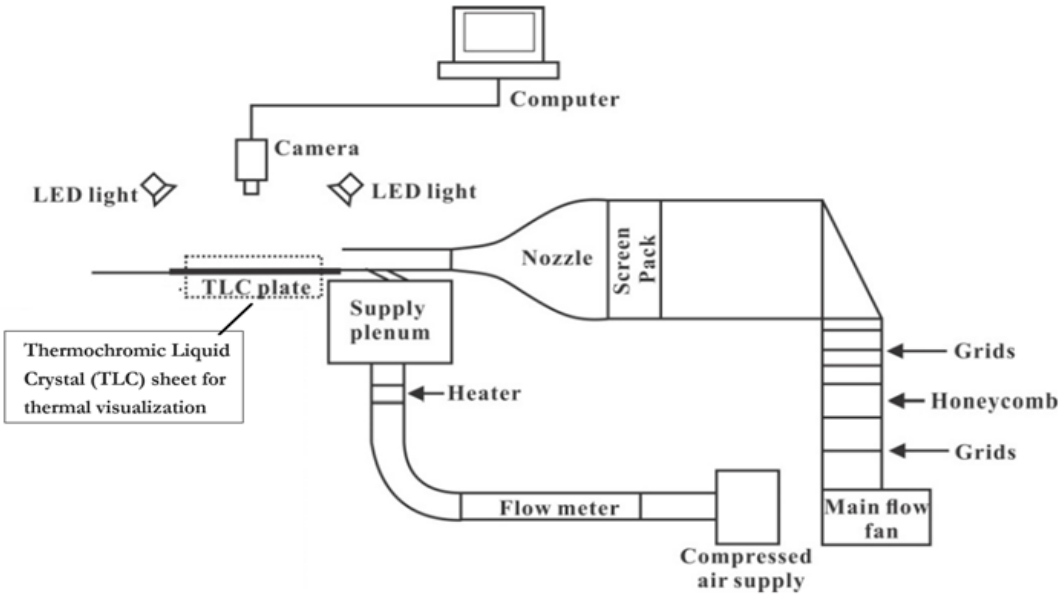

Figure 3.1: Flat plate wind tunnel in the University of Minnesota Convection Heat Transfer Laboratory. Data are taken at the TLC plate, downstream of the supply plenum and film cooling hole.

3.2 Upstream test section

After upstream preparation, the air passes through a wind tunnel contraction section and into a flow prep section that was manufactured for this study. The schematic of this inserted section at the exit of a nozzle is shown in Figure 3.2. An inserted part of the wind tunnel allows approach flow to further develop from one with a laminar boundary layer on the test wall to a mature turbulent boundary layer flow. At the appropriate location, transition is tripped with a step strip. Additionally, a vortex generator was installed in the inserted region, as shown in Figure 3.3. The aim of the tunnel design is to study the interaction of a near wall vortex and a film cooling jet. Details about the vortex generator and transition trip are introduced in the following section.

Figure 3.2: Inserted section of wind tunnel to allow flow development

The coordinate system of the testing section is shown in Figure 3.3. Important to consider are the relative locations of the vortex generator and the trip wire. The major flow features produced by the vortex generator are those needed to simulate a leg of horseshoe vortex, and, by boundary layer growth, a wake flow. Important features are the developing length for the stabilized embedded vortex and the thickness of the turbulent boundary layer.

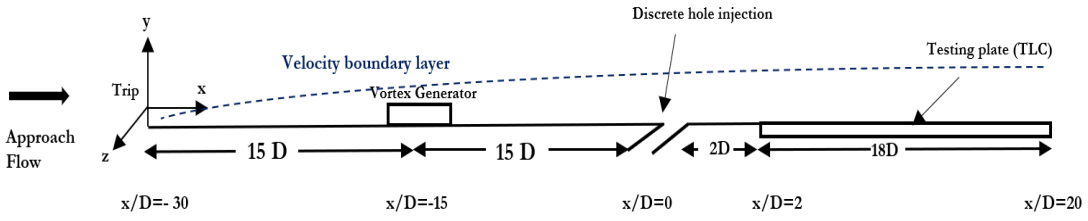

Figure 3.3: Coordinate system and schematic of wind tunnel test section for experiment. (TLC) is Thermochromic Liquid Crystal.

Another factor to consider in the experiment design is the hole testing piece scale and resultant spatial resolution of data, Reducing the testing hole piece scale is simply done without major modification to the wind tunnel, however data accessed are limited by the characteristic length of the measurement techniques. Vital information cannot be

accessed if the spatial resolution is low. An example is the near-wall region where the velocity gradient in the turbulent boundary layer is large.

One could introduce a larger hole testing piece, but this requires more developing length upstream of the testing piece, at the exit of the nozzle of the wind tunnel. This allows more detailed flow and thermal data with increased spatial resolution. The test section scale is restricted, however, by the tunnel delivery section.

Development of approach flow near-wall vortex and turbulent boundary layer

Few studies had been dedicated to this topic, as reported by Ligrani, et al. (1989), Chung, et al. (2009), and Cui, et al. (2022). The uniqueness of these studies is that they introduce a large-scale vortex generator, since they have larger dimensions, especially the height of the vortex generator. Details of these studies are summarized in Table 3.1. Ligrani, et al. (1989) was the first to examine the near wall vortex upstream of the film cooling jet. They introduce a trip with 1 mm, 91.9-hole diameters upstream and a triangular geometry of vortex generator -41.9-hole diameters upstream of discrete hole injection. Then, Chung, et al. (2009) reported a reduce developing length between the trip and the vortex generator. Still, their data show a clean embedded vortex within the thick, turbulent boundary layer. Recently, this was reported by Cui, et al. (2022). They introduced the vortex generator 15 hole diameters upstream of the discrete hole testing piece.

The decision of the distance between the vortex generator and the injection point, 15 hole diameters, was based on studies by Velta, et al. (2016), see Figure 3.4 and 3.5. They examined the vortical flow structure behind a vortex generator (VG) embedded in a turbulent boundary layer and found a pair of vortices behind the rectangular VG. The primary vortex fluid flows over the top of the VG in the primary flow direction. The secondary vortex is a horseshoe vortex that appears at the lower part of the VG.

At the early stage of generation, vortices are a complex developing region that stabilizes into a steady vortical structure in the far region. Thus, in practical applications, if the vortex generator is placed a certain distance upstream of the film cooling hole, it can be used to investigate the interaction between a near-wall vortex and film injection.

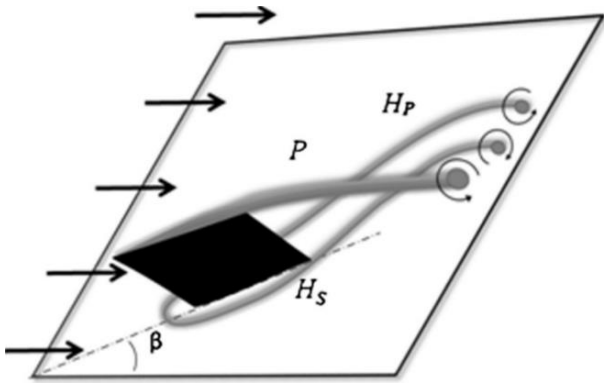

Figure 3.4 Topology of the basic vortex structure found from dye visualization (Velte, et al., 2016)

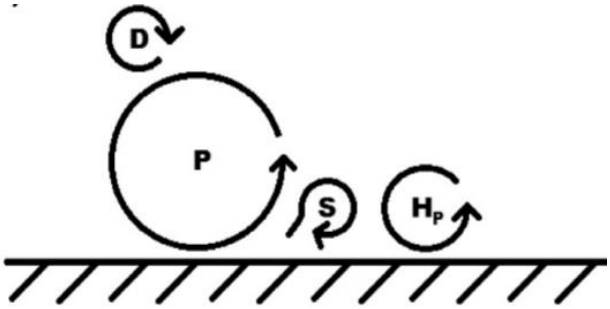

Figure 3.5 Vortex structure topology behind the vortex generator, by direct combination of the basic vortex system and the secondary vortex structure (Velte, et al., 2016)

Table 3.1: Parameters for Trip and Vortex Generator (VG). N/A notes "cannot be found in the literature."

Parameters.	Present Study	(Cui, et al., 2022)	(Chung, et al., 2009)	(Ligrani, et al., 1989))
Trip location	-30D	-30D	N/A	-91.9D
Trip thickness	3mm	3mm	2mm	N/A
VG location	-15D	-15D	-25.7D	-41.9D
VG type	rectangular	rectangular	triangular	triangular
VG height	1.1D	1.3D	2D	3.38D
VG length	3D	3.33D	4D	8.04D
VG Attack angle	10°	10°	20°	18°
Hole diameter	12mm	6mm	15mm	9.45mm
Hole Reynold number	9000	8000	9000	11000

Vortex generator

A rectangular wing was applied as a vortex generator in this study, as shown in Figure 3.6. The height of the vortex generator is 13mm. This value is identical to the hole diameter. The length and the width of the vortex generator are 35mm and the thickness of the baseplate is 0.5mm. It is expected that the baseplate doesn't significantly influence the development of the turbulent boundary layer. The attack angle of the vortex generator is 10 degrees. This vortex generator produces clockwise vortices as seen looking downstream.

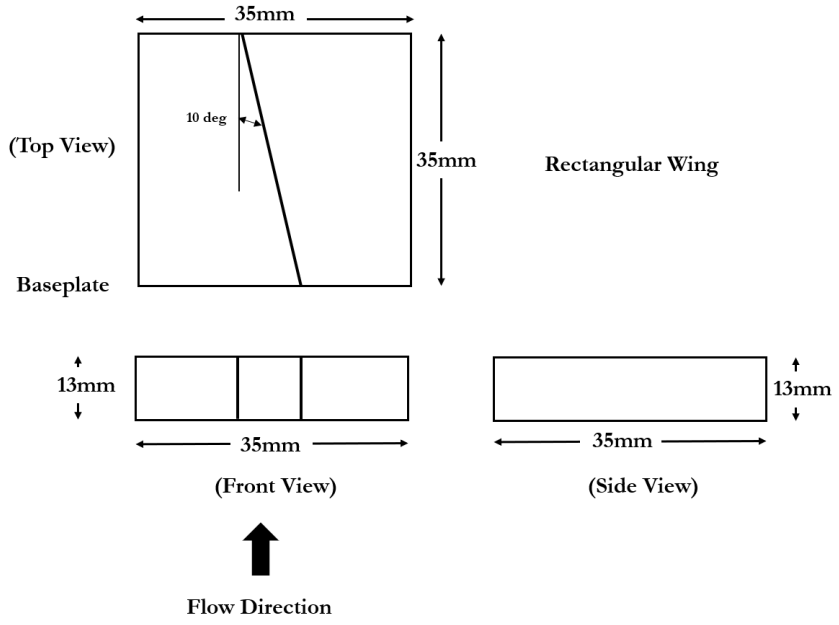

(a)

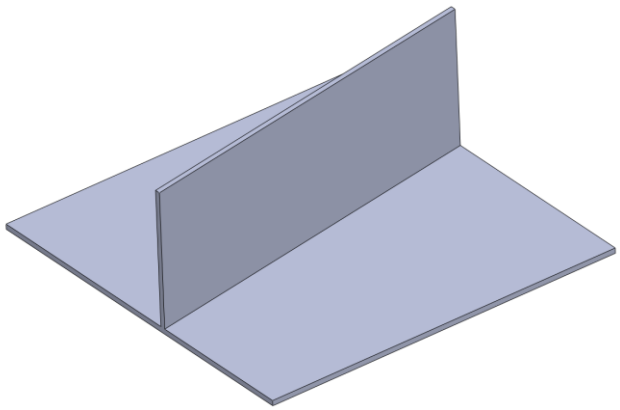

(b)

Figure 3.6: (a) Vortex generator geometry and orientations to produce clockwise vortices (as viewed in pitch/span planes). The dimension of the rectangular wing is shown (b) Vortex generator in three-dimensional view.

Trip

The trip aims at tripping the boundary layer to turbulence and thickening and stabilizing the turbulent boundary layer flow while making it spanwise uniform. The height of the trip is 3mm, with a 0.5mm baseplate. The trip is introduced at the exit of the nozzle, 60-hole diameters upstream of the injection hole centerline. The thickness of the trip is selected by measuring the boundary layer thickness 7-hole diameters upstream of the hole injection. This aims to produce a turbulent boundary layer flow that allows embedding a near-wall vortex produced by the vortex generator. The schematic of the trip is reported in Figure 3.7.

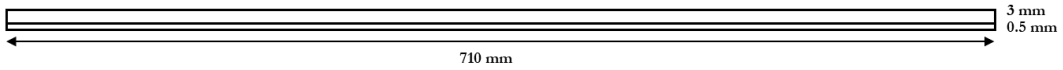

(a)

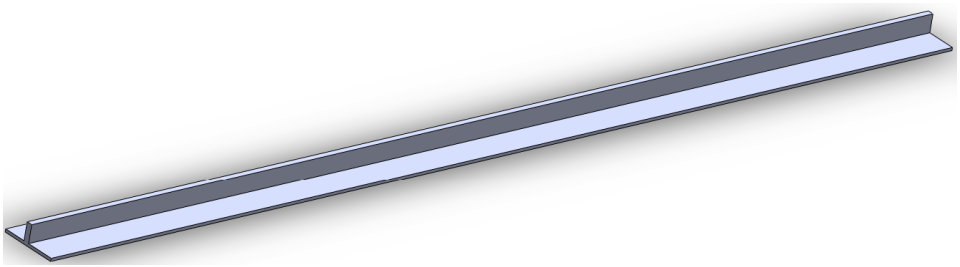

(b)

Figure 3.7: (a) Trip strip with 0.5mm baseplate, and 3mm height. (front view – flow is front to back) (b) Trip strip in three-dimensional view.

3.3 Testing section

Next, the flow enters the testing regime of the wind tunnel at the exit of the inserted development section discussed previously. The testing section is connected to the inserted section and consists of rectangular duct channel with an outer wall that is open to the atmosphere downstream. The wind tunnel channels are made of polycarbonate, a material that provides good thermal insulation. The heat conduction is confirmed negligible in the present experiment. The opened outer wall provides access to thermal and velocity distribution measurements on a testing wall, and cross-sectional planes in the tunnel. Data here were taken by a 3-axis translation device (Velmex Inc, MB4024KIJ-S6), moving a

temperature or a velocity probe, as shown in Figure 3.8.

Though profiles can be taken by using the open wind tunnel facility, velocity variations between the mainstream and the atmosphere require attentive consideration. A resultant shear layer due to velocity gradient is observed between the mainstream flow and the ambient air. To reduce the influence of this shear layer on testing, a mild taper of the outer wall is applied to accommodate the growing boundary layers on the wind tunnel walls. This mild taper can slightly reduce the thickness of the shear layer. Additionally, the velocity profile was measured along the wall-normal direction at three downstream regions. Results show that the scale of the approach flow is far larger than the shear layer and coolant mixing layer thickness, indicating that shear in the open layer is negligible. Overall, the mainstream provides proper insulation between the coolant mixing layer and layer of shear with the ambient air. Thus, it is confirmed that the shear layer doesn't influence the present measurement in the testing region.

Thermal and velocity plane distributions downstream of the film cooling hole injection region were taken by inserted probes. Additionally, temperature distributions on the surface downstream of the film cooling hole were documented by the Thermochromic Liquid Crystal (TLC) technique. The testing section area for the TLC technique is 30cm × 30cm. In general, time-averaged three-dimensional scalar transport between the mainstream and the ejected coolant can be documented in the present experiment. More information about the measurement techniques and data processing is discussed in Chapter 4.

Figure 3.8: Translation device for moving the thermocouples and pitot tube probes

3.4 Injection system

The purpose of this study is to understand the interaction between coolant injection and the mainstream. The mainstream was discussed in the previous section. This section focuses on the coolant injection and discrete hole geometries. Air first exits from the building compressed air system. The mass flow rate of coolant is controlled by a valve and is measured by a laminar flow meter. The air passes through the supply pipe, followed by a laminar flow meter, and then enters a heating plenum. The plenum is heated by an electrical resistance heater, with maximum power of 1.7 kW. The resistance heater is controlled via a variable AC transformer to supply an appropriate level of heating. It is expected to have uniformly, heated flow in the plenum. The heater is to raise the air 10 degree Celsius higher than the mainstream. This heated air is named "coolant" in the present study. This coolant then passes into a discrete hole channel in a discrete hole testing piece, and mixes with the approach (passage) flow. The discrete hole testing pieces are replaceable.

3.4.1 Injection parameters

For discrete hole injection, the coolant's relative flow rate is captured with the blowing ratio, M, defined as:

$$M = \frac{\rho_c U_c}{\rho_m U_m} \tag{3.1}$$

and the density ratio:

$$DR = \frac{\rho_c}{\rho_m} \tag{3.2}$$

Note that the velocity in the numerator in Eq. (3.1) is measured by the laminar flow meter. In this work, the density ratio for the discrete hole flows is near unity, about 0.97, since the discrete hole flow is air that is heated ten degrees Celsius higher than the room temperature.

3.4.2 Discrete hole injection

The intention of this experiment is to examine the effect of cylindrical holes and shaped holes at various compound angles (angle between the hole axis direction and the approach flow direction). The discrete hole is located at the exit of the inserted section of the wind tunnel. The discrete hole pieces are inserted into the test wall of the wind tunnel. Replaceable pieces for discrete hole geometries are introduced in the present experiment, as shown in Figure 3.9. This design permits varying the hole geometry and hole orientation. The discrete hole pieces were 3D printed from polylactic acid (PLA) in the Aderson Student Innovation Labs at the University of Minnesota. The resolution of polylactic acid fabricated pieces is 0.1 mm, a dimension which correlates to the scale of the PLA filament, and the hole surface roughness.

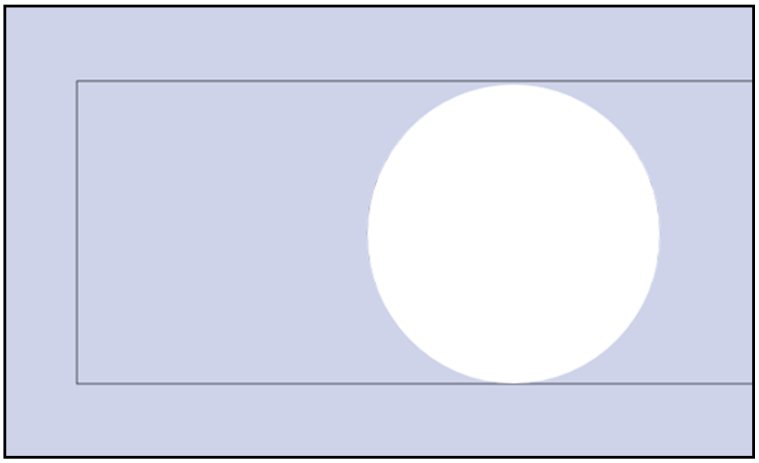

(a) Piece of wind tunnel test wall that receives the inner piece of the film cooling hole test section

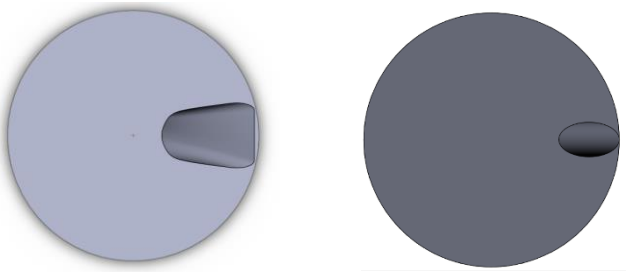

(b) Inner piece: shaped hole (c) Inner piece: round hole

Figure 3.9: Discrete hole testing pieces. (a) Wall section to receive insert (b) Inner piece: shaped hole (c) Inner piece: round hole

In this study, two different discrete film cooling hole geometries were used. In the first geometry, the classical round hole testing piece is chosen. The schematic of the round hole is shown in Figure 3.10. This choice was intended to explore the mixing between the incoming vortex and film cooling injection in a classical film cooling hole geometry. It is widely known that the round hole produces a well-known counter rotating vortex pair (CRVP), jet lift-off, and jet entrainment. This case serves as a baseline for flow qualification and comparison with the shaped hole geometry. The hole diameter is 12mm, and the injection length-to-diameter L/D was 6.64.

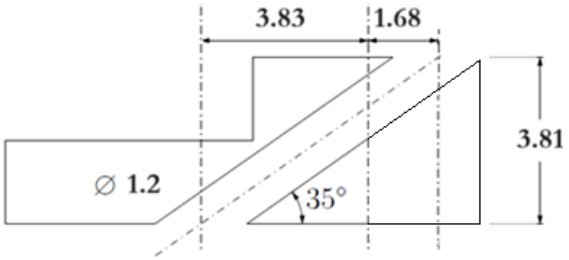

Figure 3.10: Cylindrical Hole Geometry (dimensions in cm)

In the second hole geometry, the laidback fan-shaped hole testing piece is chosen. The shaped hole diameter is 12mm, hole injection length-to-diameter, L/D, is 6.65. These values are identical to the round hole case. The geometry of the shaped hole is shown in Figure 3.11. It is worth noting that the shaped hole dimensional parameters are identical with those of Stinson (2019). Thus, results here can be compared with full coverage film cooling cases with discrete shaped hole injection in Stinson's datasets. In addition, the present hole geometry has similar design parameters with the so-called 7-7-7 baseline shaped hole by (Schroeder & Thole, 2014), as reported in Table 3.2 and Figure 3.11. Thus,

similar fluid and coolant concentration patterns are expected with the 7-7-7 shaped hole in literature in literature and the present shaped hole.

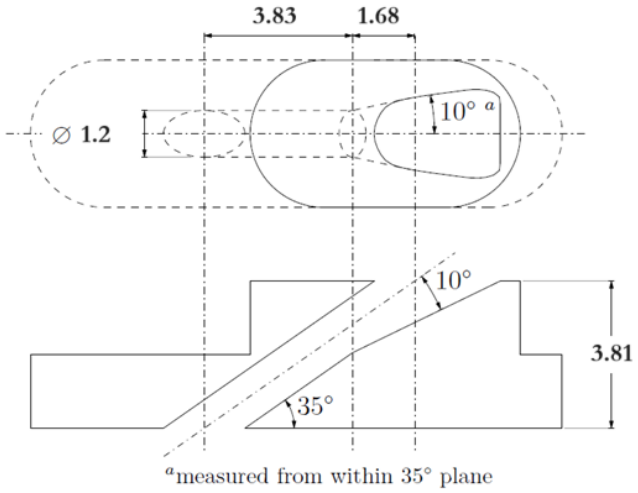

Figure 3.11 Laidback Fan-shaped Hole Geometry of the 7-7-7 design (dimensions in cm), (Schroeder & Thole, 2014)

Table: 3.2 Geometric Parameters for present study and 7-7-7 shaped hole

Parameter	Present Shaped Hole	7-7-7 Shaped Hole
Injection angle	35°	30°
L/D	6.5	6
Laidback angel	10°	7°
Lateral angle	10°	7°

Chapter 4. Instruments for measurement

In this work, various air flow measurements were made. Primary measurements, including pressure and temperature, were required to process the main results of interest. In the following sections, the measurement equipment, the measurement techniques, and any required calibrations for the measurements are described.

4.1 Pressure and velocity measurement

This section documents the instruments for pressure and velocity measurements in the passage. The pressure measurement, taken at the static pressure tap, is done by an inclined manometer. Measurements within the wind tunnel were made with a pitot-static probe for calculating the mean tunnel velocity and measuring the turbulent boundary layer profile. One thing to highlight is that this study does not require absolute pressure, since information documented in this experiment is pressure difference, other than pressure data for property evaluation. Static pressure is used for air property data.

4.1.1 Inclined manometer

The pressure difference in this experiment is documented by displacement of fluid in the inclined manometer. Such cases require an incompressible fluid in the inclined manometer, water and oil are used. A U-tube manometer here has two vertical tubes that are connected at the bottom and contain the same fluid. Different pressures can be applied to the top ends of these two tubes. An unequal pressure applied on the top ends, can be related to the displacement, as defined in Eq. (4.1), where ΔP is pressure difference in the two tubes of the manometer, ρ is the density of the fluid used in the manometer, and Δy is the difference between the heights of the fluid columns in the two tubes.

$$\Delta P = \rho g \Delta y \tag{4.1}$$

The inclined manometer used in this study is made by Dwyer Co. (Mode number 246). The scale for the manometer is "inches of water," indicating the displacement. The specific gravity of Dwyer red gage oil is 0.86. The measurement ranges are from 0 to 6 inches of water column, as 0-1494 Pa. The measurement resolution is 0.01 inches (0.25 mm). Beyond the near wall region, this resolution is sufficient for the present study.

Figure 4.1: Inclined manometer used in this study (Nawathe, 2022)

4.1.2 Pitot tube

The pitot-static probe (Figure 4.2) makes indirect velocity measurements by measuring the pressure difference between the total pressure and the static pressure. The probe is designed to be minimally sensitive to pitch and yaw within several degrees from $0°$. The velocity indicated by the probe can be derived using the Bernoulli equation, which arranges to relate the pressure differential measured to the flow velocity, as shown in Eq. (4.2). This requires steady and incompressible flow conditions.

$$U = \sqrt{\frac{2\Delta P}{\rho}} \tag{4.2}$$

In this experiment, the turbulence level was moderate, and time average steady flow was assumed. However, since the level of the turbulence intensity was low and constant at the measurement location, the velocity is corrected when using the following approach:

$$U_{correct} = \sqrt{\frac{U^2}{1 + Tu^2}} \tag{4.3}$$

Here, Tu is the turbulence intensity level. The correction can be derived by rearranging Eq. (4.3) for ΔP and time-averaging the velocity term. Additionally, as this is a gas flow, there are small differences in gas density between the static and pitot pressure locations. A first-order correction for this effect was applied by averaging the static density and the

pitot density. This correction was considered appropriate here, rather than using a compressible formulation, because of the low Mach numbers (below 0.04) in this experiment.

Figure 4.2: TSI Alnor Telescoping Pitot Probe. The red part is the total pressure port, and the blue part is the static pressure port. (Stinson, 2019)

4.2 Temperature measurement

Instruments for temperature measurement are introduced in this section. The present study intends to document the coolant transport from film cooling injection, and how it mixes with the mainstream. One way to track the coolant concentration is to mark coolant by slightly higher temperature relative to that of the mainstream. In these tests, the coolant temperature is 10 degrees Celsius higher than the mainstream temperature. Thus, the coolant concentration in a mixture of coolant and mainstream flow was found from the local temperature distribution in the flow.

The unique open outer wall in this wind tunnel, and the testing surface being the closed wall, provide access to inflow and surface data. The in-field temperature is taken by an inserted thermocouple, with the surface temperature by the thermochromic liquid crystal technique.

4.2.1 Flow physics to characterize

A common flow feature in film cooling is the Counter Rotating Vortex Pair (CRVP), as a well-known time averaged flow pattern found at the film cooling injection location. This pattern is generated by the shear layer vortices produced at the windward side of the film cooling jet. Researchers in film cooling usually relate CRVP patterns to film cooling

effectiveness, as the counter rotating vortex pair will entrain the mainstream flow into the coolant flow downstream of the coolant injection point. One of the major research topics in film cooling is to reduce CRVP intensity, since doing so will weaken the jet entrainment into the coolant flow downstream of film cooling jet (Coletti, et al., 2013). Nevertheless, there are other instantaneous patterns in film cooling jet that cannot be ignored, such as shear layer vortices, eddies transported in the turbulent boundary layer, and hairpin vortex bursting and breaking and resultant turbulent mixing (Sakai, et al., 2014). These instantaneous features, coupled with the time averaged CRVP feature, must be considered to provide a complete perspective to the physics of film cooling.

One constraint for this study is the time scale measured by the instruments. Data taken here are time-averaged measurements instead of instantaneous measurements. Thus, many important instantaneous features about the jet in crossflow, such as shear layer vortices, hairpin vortices bursting and breaking up, and jet pulsation, cannot be characterized. This is caused by difficulty of accessing instantaneous temperature measurements with thermocouples in the flow and the thermochromic liquid crystal data on the surface. Though the measurements present in this thesis are not instantaneous, they are still useful for evaluating film cooling effectiveness in a general way.

4.2.2 Thermocouple

In-field temperature in this study is documented by thermocouple probes. The thermocouple reading takes time to average data at one point first, then transverse the probe along the entire plane to get a temperature field. The translation device here is a Velmex Inc, MB4024KIJ-S6 that enables three degrees of freedom (x, y, z). Thus, it can document flow temperature at a particular point instead of over an entire cross-section plane at one time.

Details about thermocouples are discussed here. One thing to consider is its low sampling and respond frequency, limiting its capturing of high frequency flow features. Such high frequency flow features, for example shear layer vortices, hairpin vortex, and small-scale eddies, are important to understand the physics behind film cooling injection flow.

The theory of a thermocouple is based on the Seebeck effect. The Seeback effect states that if two dissimilar metals are joined, and the junction is heated relative to the other ends, an electromagnetic field is generated, resulting in a potential difference. This

potential difference is related to the temperature difference between the junction and other end. The value of this potential difference, in Volts, is usually very small. This can be used to accurately measure the temperature of a heated end, or the junction, by way of calibration.

The thermocouple used here is type E, chromel-constant. Its useful temperature ranges from 3-1150K. The range of this study is from ambient, 23℃ to 35 ℃. The two ends of each thermocouple are known as the hot and cold junctions. The hot junction is applied to temperature measurement and the cold junction is maintained in the ice bath. In this study, the data acquisition (DAQ) unit replaces an ice bath, Agilent 34970A electronic equipment. Agilent 34970A can convert the potential difference from the thermocouple to temperature, directly. This correlation is based on NIST data documented by Burns, et al. (1993).

The calibration for thermocouple in this study was conducted by ice bath and liquid-in-glass thermometer setup. Results show that calibration is aligned with cold junction compensation from the DAQ unit. The uncertainty between calibration and DAQ unit is 0.024 ℃.

4.2.3 Thermochromic Liquid Crystal

To evaluate the temperature distribution on a surface, several techniques: thermocouple, infrared thermometer, and so on are widely used. Surface temperature distribution in this study is documented by the Thermochromic Liquid Crystal (TLC). TLC is a measurement technique that can provide rapid (limited by the thermal responsiveness of the TLC) information about the temperature field, and, by extension, film cooling effectiveness distribution on the surface. A thermochromic liquid crystal (TLC) test region is mounted on the test wall downstream of the test piece in which the injection hole resides. The TLC sheet used in this study is from HallCrest Inc. The sheet has a reliable range of 22 ℃- 34 ℃ and came in a sheet with a size of 30.48 cm × 30.48 cm. The picture of TLC on a human's hand is shown in Figure 4.3(a), and the TLC temperature spectrum is shown in Figure 4.3(b). In general, this section details the theory, measurement technique, and calibration of the thermochromic liquid crystal sheet.

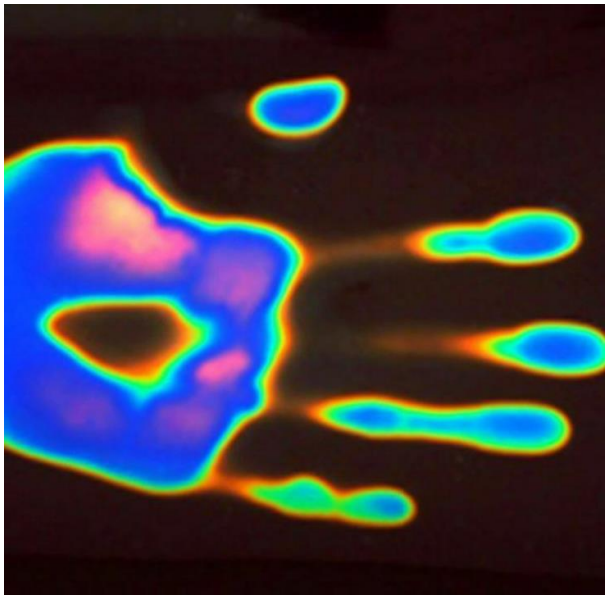

(a)

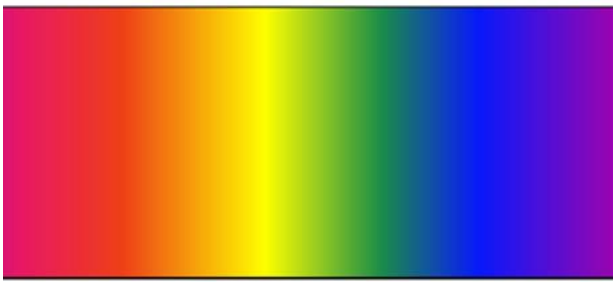

(b)

Figure 4.3: Thermochromic liquid crystal sheet. (a) TLCs response on a human's hand (b) TLCs spectrum. Red is the colder temperature, and violet is the hotter temperature.

Theory of TLC

The measurement layer is formed by TLC particles responding to temperature differences in the area of interest. Thermochromic liquid crystals (TLCs) are a type of cholesteric liquid crystal that changes color in response to temperature changes. When exposed to white light, TLCs reflect different wavelengths of light, causing them to change color. As the temperature increases, the reflected light changes from red to violet, passing through the visible spectrum, as shown in Figure 4.3 (b). TLCs can also be formulated to react to temperature changes as small as 0.1°C and are accurate up to +/- 1°C. The optical response of the TLC layer documents the surface temperature distribution of tunnel wall downstream of coolant injection.

Calibration techniques

The steady state Thermochromic Liquid Crystal (TLC) technique is applied to measure the surface temperature distribution used to obtain the film cooling effectiveness. The digital camera records 450 × 900 pixels images for calibration. The voltmeter (DAQ Agilent 34970A) measures the temperature at a point on the surface at which the thermocouple is positioned on the TLC sheet, located downstream of the coolant injection. Calibration points for this comparison can be found in Figure 4.4. Calibration is done by comparing the temperature, as recorded by the thermocouple with the color at the same location on the plane, over various coolant temperature ranges from 22°- 34°.

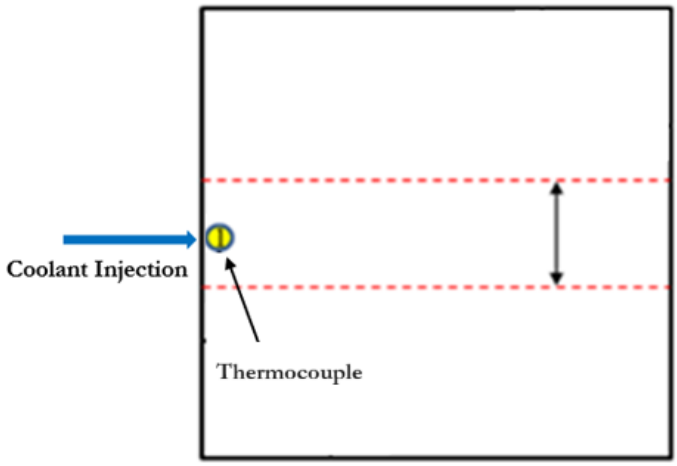

Figure 4.4: The layout of the thermocouple for calibration

Then, the recorded pictures here are converted from the RGB (red, green, blue) format into HSI (hue, saturation, intensity) format. This provides a correlation between the hue values and temperature, by recorded temperature and hue values at the calibration points. These data are then fitted with a second-degree polynomial, deriving a calibration curve for the present study, shown in Figure 4.5.

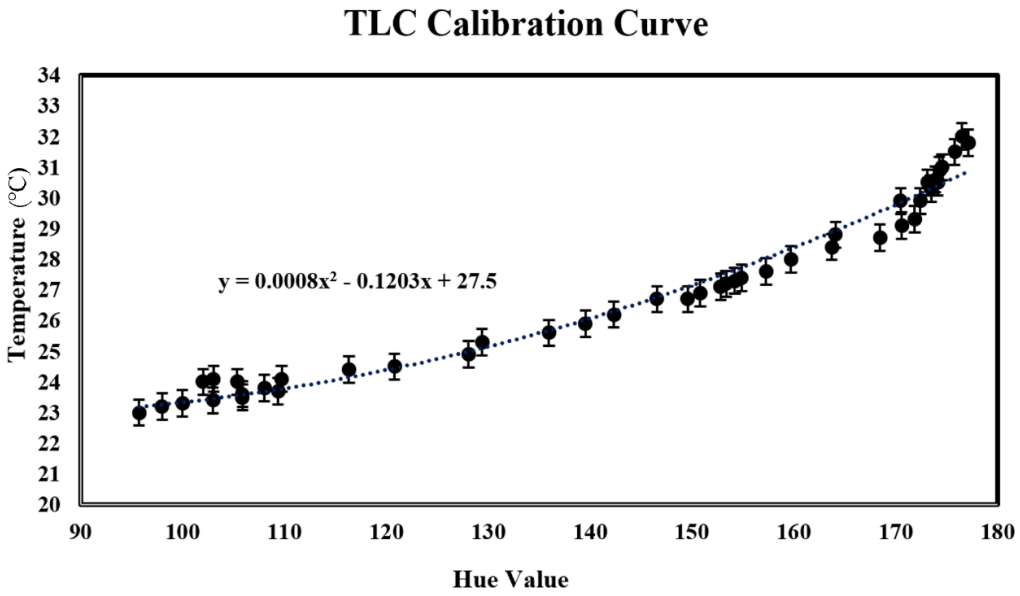

Figure 4.5: The Temperature vs. Hue calibration curve for the Thermochromic Liquid Crystal, is obtained by reference to a thermocouple. Taken on the test plate.

Uncertainty propagation

The calibration uncertainty for temperature is ±0.06°C, with a 95% confidence interval (we are 95% confident that the true value lies within a band of this size). From Hay and Hollingsworth (1996), the uncertainty of TLC measurement is derived from the calibration curve of hue value. The root sum square propagation formula is applied to maintain a similar level of confidence between the measured quantities and the resultant quantities.

$$\Delta T = \sqrt{\left(\frac{\partial T}{\partial Hue}\right)^2 + (\Delta T_{cali})^2} \tag{4.4}$$

The uncertainty of temperature measured by the TLC ranges from 0.06℃ to 0.25℃ over the hue value range. The uncertainty of temperature measured by the thermocouple is 0.024℃. The uncertainty of film cooling effectiveness is 0.0256, that is 25.6% at η =0.1 and 5.12% at η =0.6. The largest uncertainty for dimensionless (recovery) temperature, θ, is 0.006, which is 3% at θ = 0.2 and 0.75% at θ = 0.8, as reported by Zhu, et al. (2021). More detail about the propagation of uncertainty can be found from Moffat (1998).

4.3 Mass flow measurement

Mass flow measurements for film cooling injection were taken using a laminar flow meter. In the experimental facility, one laminar flow meter is installed for measuring the injected

mass flow rate to the discrete hole injection site. The volumetric flow rate here is measured by the laminar flowmeter (Meriam Z50MC2-2), as shown in Figure. 4.6. The correlation between the pressure difference and volumetric flow rate (Q) is,

$$Q = \rho\,(13.7727 \times \Delta P - 0.046\Delta P^2)\frac{\mu_{std}}{\mu_f} \tag{4.5}$$

where μ_{std} is the dynamic viscosity for 21.1℃, and μ_f is the dynamic viscosity for the testing environment, as a function of air humidity and temperature. The pressure difference is documented by the inclined manometer with 0.28% uncertainty.

Figure 4.6 Laminar flow meter.

Chapter 5. Experimental design

The following section introduces the design of the experiments from turbines in the actual engine to linear cascade representations and from linear cascades to flat plate simplifications. Parameters of interest to the investigations and measurements are presented. The intent of such experiments is to document and explain coolant migration.

5.1 Philosophy for experimental work

The advantage of this experimental study is that it provides a chance to document the physics of interest, more realistic (close to mother nature -- also named as "truth") representation than analysis. Experiments may approach problems of interest with reduced bias since they more closely model nature. They also offer greater flexibility and originality when investigating unknown phenomena. An example of this is the experiment work of Jabbari, et al. (1996). These authors investigated, in a general setting, discrete hole injection of coolant distributed uniformly along an entire surface.

The challenge for such an experimental design is that it is too realistic (including too many types of physical processes) to understand all the details. For example, passage secondary flow in the turbine cascade is too complex to understand in detail. This, coupled with jets in crossflow produced by discrete hole injection, is a problem that has more than three parameters to be considered. Another example is the interaction between the approach flow near-wall vortex with the jet in crossflow created by discrete hole injection on the flat plate (endwall). Such problems have more than three parameters, such as hole skew angle away from the approach flow, incoming vortex intensity and rotational direction, parameters of the jet in crossflow. In general, space parameters of interest, when modeling directly from realistic settings, is far beyond the state of the art of our understanding. Thus, the key is to identify a particular and significant perspective that properly simplifies the degree of complexity for the selected problem without being lost in the complexity.

5.2 From engine to turbine cascade to flat plate

Understanding the secondary flow in the hot section of gas turbine is significant for gas turbine designers. To address these types of studies requires applying an experiment design to simulate the important flow features at the engine conditions. A common way to model these flow features in the engine is a stationary cascade wind tunnel modeled stator, or rotor, test rig. This physical model, in a cascade, enables us to understand engine flow from a unique perspective, as shown in Figure 5.1.

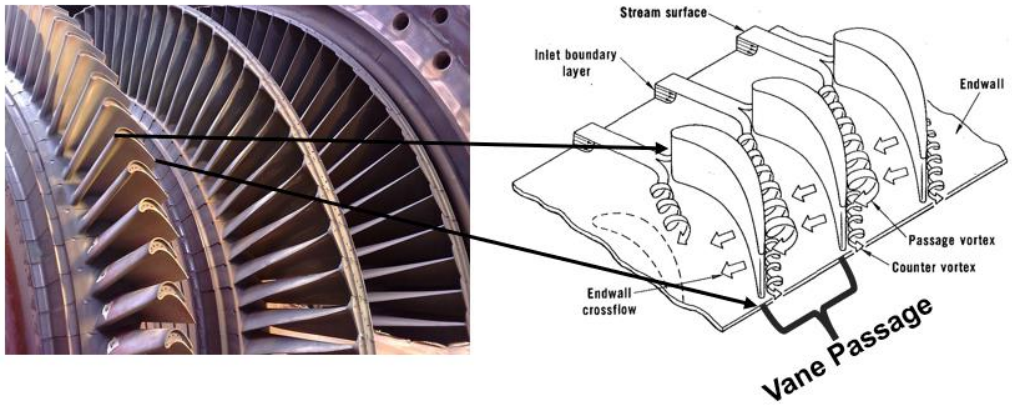

Figure 5.1 Model the turbine in the hot section of engine (left) to capture in a stationary cascade experimental facility (right)

Most measurements in the passage, or cascade were of coolant transport taken on the passage endwall. Difficulties in doing so were due to the tiny discrete hole sizes for

coolant injection, to three-dimensionality and unsteady secondary flows in the passage. These flow features cannot be documented by sufficient spatial and temporal resolution with current measurement techniques. Additionally, interpreting such data requires thoughtful consideration about multiple flow features at various locations of the passage. These flow features are unclear in real engines and even in stationary cascade test rigs. Parameters include inlet Reynolds number, inlet flow turbulence intensity, local acceleration and deceleration due to the converging/diverging of the passage, Mach number, upstream coolant injection, rotation of the rotor, the pressure leg of the horseshoe vortex, the suction leg of the horseshoe vortex, and the crossflow effect from pressure to suction surfaces of the passage on the endwall.

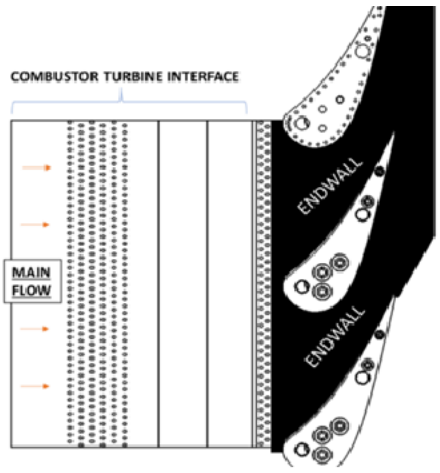

(a)

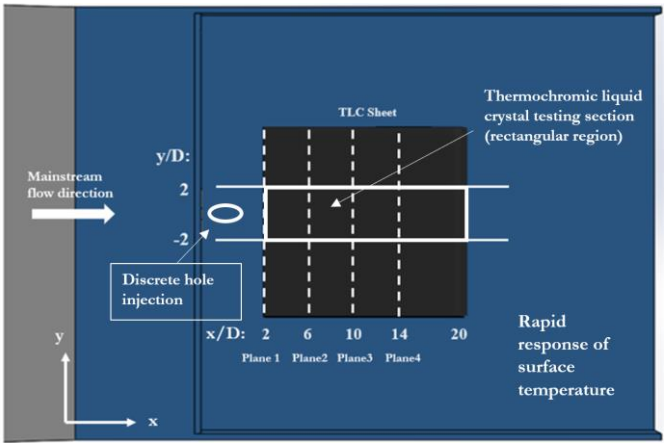

(b)

Figure 5.2: From turbine cascade to flat plate experiment. (a) Turbine cascade wind tunnel (b) Flat plate wind tunnel. Data are taken, in this example, with a TLC Thermochromic Liquid Crystal (TLC) surface mounted on the test wall downstream of a film cooling hole.

Due to the insufficient data resolutions in the turbine cascade, an alternative way is to conduct a film cooling experiment on a simplified flat plate in a wind tunnel, then relate the results back to the turbine cascade, as shown in Figure 5.2. In the flat plate experiment, typically, an enlarged discrete hole test piece is applied. This allows measurement with good spatial and, possibly, temporal resolution. One can extract secondary flow patterns and characterize them in detail. In contrast, a flat plate experiment provides the flexibility to extract the most significant secondary flow features in the turbine cascade and characterize them in detail. Common parameters for such film cooling studies on the flat plate are associated with the discrete hole geometry, discrete hole orientation, coolant density ratio, blowing ratio, approach flow boundary layer thickness, favorable/unfavorable streamwise pressure gradient, turbulence intensity, Reynolds number of coolant injection, crossflow as secondary flow, and embedded near-wall vortices.

5.3 Design of the present experiment

In this thesis, an area that deserved more effort for the endwall discrete hole film cooling is the upstream of the passage where the dominant flow features are horseshoe vortex legs and the coolant-injection-generated vortices. The present experiment aims to characterize the coolant concentration by vorticity in detail from discrete hole injection on a flat plate wind tunnel, then apply this result to validate the model for vortex interaction in the turbine cascade. In an experiment design on a flat plate, a horseshoe vortex is simulated by a streamwise vortex produced by a vortex generator placed upstream of the discrete injection hole. The coolant vortices (vortices generated by coolant injection) are simulated by varying the hole orientation (angle of hole axis skewed away from the approach flow), and hole geometry. However, it is worth noting that variations in many secondary flow features are disregarded, including inflow turbulence intensity, crossflow, coolant density ratio, and approach flow boundary layer thickness. The modeling process is presented in Figure 5.3.

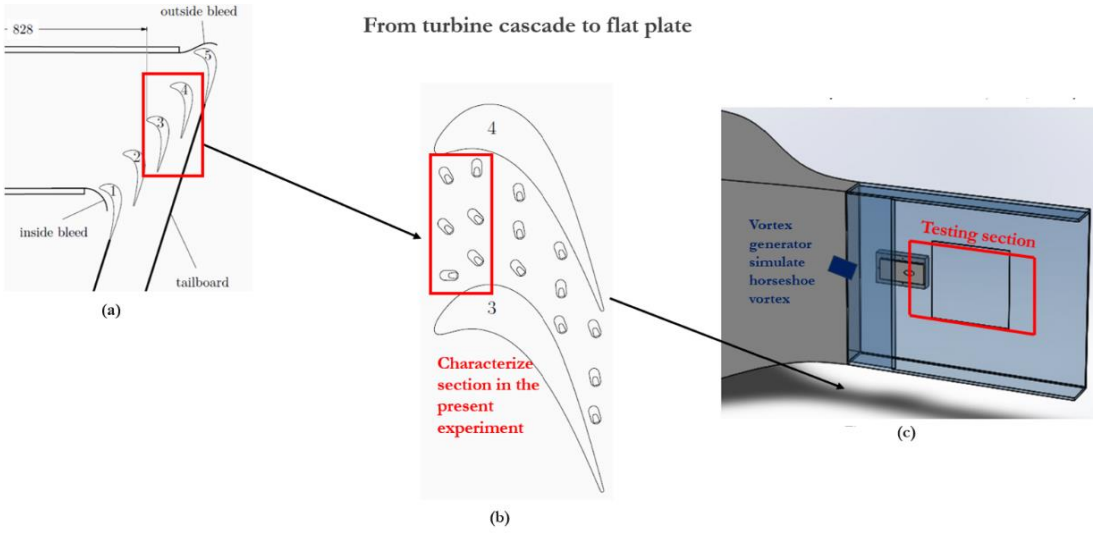

Figure 5.3: Model the secondary flow in the turbine cascade by experiment on the flat plate. (a) Cascade test section (Stinson, 2019) (b) Endwall discrete hole film cooling in the turbine cascade (Stinson, 2019) (c) Flat plate wind tunnel. The horseshoe vortex is simulated by a vortex generator placed upstream of the discrete hole testing piece.

5.4 Experiment parameter space

The parameter space of the present experiment is shown in Table 5.1. The primary factors to vary are embedded vortex locations, discrete hole geometry, discrete hole orientation (angle of skew away from the approach flow) and blowing ratio. The schematic of vortex generator testing location is shown in Figure 5.4. The schematic of hole orientation angles is pictured in Figure 5.5.

The testing blowing ratio ranges from 0.5 to 3.5. Discrete hole orientation angles range from -60^{o} to 60^{o}. The incoming vortex rotates in the clockwise direction when looking downstream. For case "R", the vortex generator is located at y/D =-1.5, looking downstream. For case "L", the vortex generator locates at y/D =+1.5. For case "C", the vortex generator is located at y/D =0. The testing holes are cylindrical and of shaped geometry.

Table 5.1: Selected parameters to study

Embedded Vortex Location	L(y=-1.5D), C(y=0), and R (y=1.5D)
Discrete Hole Geometry	Round Hole and Shaped Hole
Discrete Hole Orientation	60 degrees (+y) to -60 degrees (-y)
Blowing Ratio, M	0.5 – 3.5

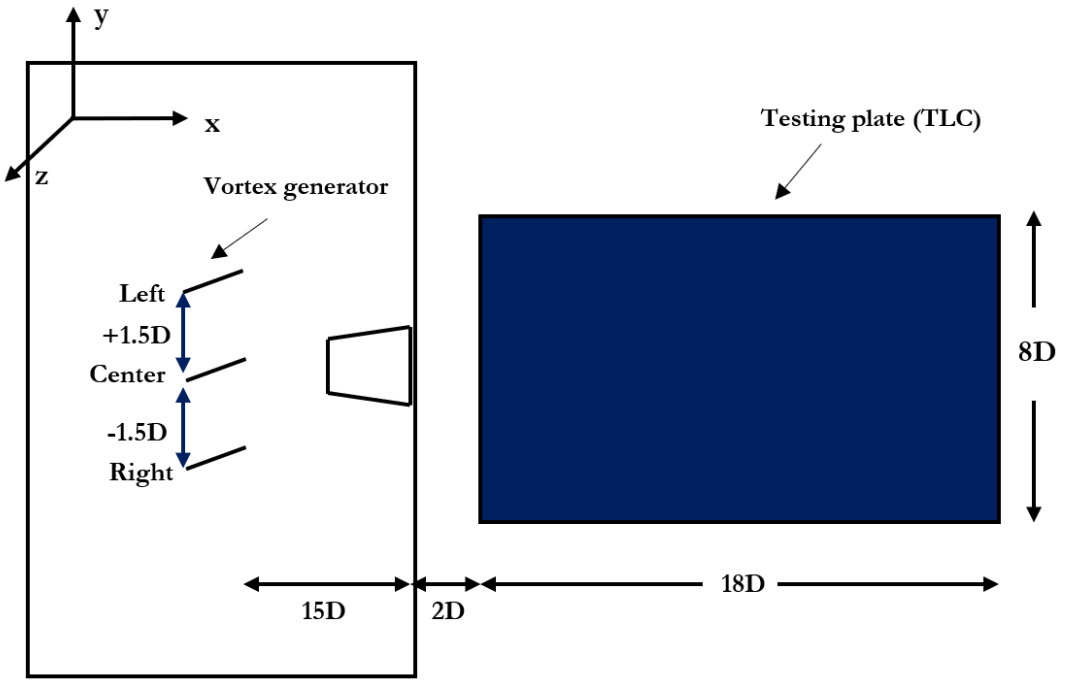

Figure 5.4: Vortex Generator Location. The incoming vortex rotates in the clockwise direction when looking downstream. Left, y/D=+1.5. Right, y/D=-1.5.

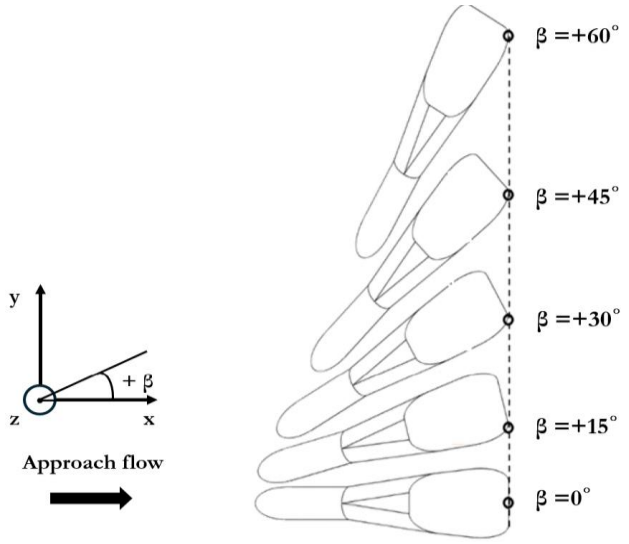

Figure 5.5: Discrete hole orientation angles β (angle skew away from the approach flow)

5.5 Coolant concentration measurement

5.5.1 Coolant concentration measurement

In film cooling studies, coolant is generally ejected from discrete holes and is then mixed with the external flow (passage secondary flow in the cascade, or approach flow upstream on the flat plate). To reduce the mixing between the external flow and coolant, it is important to track the migration of coolant downstream of the injection hole. A

common way to track the coolant migration is to measure on-surface and in-passage scalar transport (temperature distribution or mass concentration) and then relate the results back to film cooling effectiveness. The mass concentration technique includes naphthalene sublimation (Goldstein & Cho, 1995), pressure sensitive paint, PSP, (Han, et al., 2010), planar laser-induced fluorescence (PLIF) (Chyu, 1996) and magnetic resonance concentration (MRC) (Elkins, et al., 2011). The naphthalene and PSP techniques can track the on-surface coolant concentration and the PLIF and MRC can measure in-passage coolant concentration. Alternatively, temperature measurement techniques include on-surface infrared-thermometer (IR) (Ekkad, et al., 2004), thermochromic liquid crystals (TLC) (Ireland & Jones, 2000), and in-passage thermocouples (Nawathe, 2022). In general, due to the heat and mass transfer analogy, all these techniques can track coolant migration from the discrete hole injection point.

5.5.2 Temperature measurement

The present experiment uses temperature distribution to track coolant migration. The in-passage coolant migration is tracked by a thermocouple, and on-surface coolant concentration is taken by thermochromic liquid crystal. It is worth noting that this technique can offer unique in-passage coolant migration in a complicated geometry by a three-axis translation device (Velmex Inc, MB4024KIJ-S6). Though in-passage data can also be taken by more advanced techniques like MRC, or LIF, they cannot be applied in a more complex geometry (like a linear cascade). In addition, on-surface coolant concentration, such as IR, TLC, and PSP, by themselves, are insufficient for us to understand the physics behind coolant migration.

To track the coolant migration by temperature distribution, the coolant is heated 10℃ above that of the approach flow temperature. This can mark the coolant as it migrates in the passage downstream of hole injection. In-passage temperature distributions are taken by transversing a thermocouple across a plane that is perpendicular to the flow, and on-surface temperature distribution is taken by Thermochromic Liquid Crystal, as discussed in Chapter 4. Both measurements are presented as a dimensionless temperature; that is, a film cooling effectiveness (coolant centration). These two types of techniques are generally discussed in the following sections, respectively. More details about the present temperature measurement procedure can be found at Nawathe (2022) and Alqefl (2016).

5.5.3 On surface temperature measurement procedures

Temperature distribution data on the surface show the cooling efficiency accomplished by migration of coolant downstream of the injection hole. The data are documented by the thermochroic liquid crystal technique (TLC), providing rapid response of temperature distributions on the surface. Details of the TLC technique are discussed in Chapter 4. The testing surface covers most of the coolant migration region downstream of the injection hole. The testing region ranges from 2-hole diameters to 20-hole diameters ($2<x/D<20$) downstream of the injection hole. It is confirmed that most coolant leaves the surface further downstream. The lateral measured area ranges from -4 hole diameters to 4 hole diameters ($-4<y/D<4$). This choice of width of test section is to document a wider coolant area of spreading since the discrete hole axis is not always parallel to the approach flow. Instead, the discrete hole axis may be skewed to the mainstream direction. Details of the testing region geometry are shown in Figure 5.6

Surface temperatures were taken from measurements in the near-wall region. The temperature distribution is arranged in a non-dimensional form as the adiabatic film cooling effectiveness, η. The equation for η is:

$$\eta = \frac{T_{(x,y)} - T_m}{T_c - T_m} \tag{5.1}$$

Where, T(x,y) is the surface temperature measured by the thermochromic liquid crystal technique, T_m is the temperature of the mainstream, and T_c is the coolant temperature at the injection hole. Additionally, the lateral-averaged film cooling effectiveness is calculated by averaging the film cooling effectiveness values over an area. The general area for this is $-2<y/D<2$, as:

$$\eta = \frac{1}{L}\int \eta \, dA \tag{5.2}$$

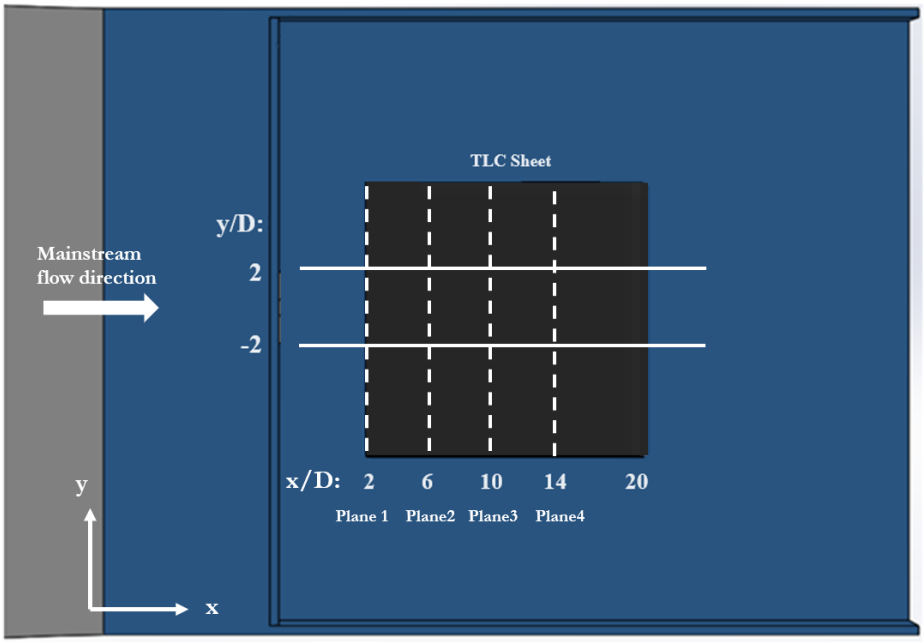

Figure 5.6: Thermochromic liquid crystal data taken in the present study. TLC measurements ranges over -2<y/D<2 and 2<x/D<20. Axial location of the measurement planes, x/D, values are shown for each plane.

5.5.4 In-passage temperature field measurement procedures

Temperature fields on multiples planes perpendicular to the flow and throughout the passage show the migration of coolant as it moves through the passage. As expected, coolant will lose its effectiveness due to jet entrainment with the mainstream by the counter rotating vortex pair (CRVP), and many other flow features such as turbulent mixing, the hairpin vortex, and shear layer vortices.

The time-averaged temperature planes were taken by a thermocouple traversed by the translation device, as discussed in Chapter. 4. This required thoughtful consideration about the measurement grid of the cross-stream planes. The present measurement grid is like that of Zhu, et al. (2021). These two experiments were performed on the same test rig and hole diameter, expecting a similar scale of coolant and mainstream mixing layer. Thus, a similar measurement grid scale is chosen.

One thing to highlight for such measurements is the spatial resolution on the test plane, particularly in the near-wall region. The present experiment possesses a large velocity gradient near the wall due to mature turbulent boundary layer development downstream, jet penetration into the approach flow, shear layer vortices, and jet entrainment downstream of the hole injection point (downwash secondary flow vector). Thus, a fine grid spacing is applied in the present experiment. Another item to highlight

is the wall-normal coverage of such measurements. The present measurement was taken up to 32% of the channel height starting from the endwall. This is where the thermocouple temperature equals the mainstream temperature, representing the edge of boundary layer.

Details of thermal plane data are documented in Table 5.2. Overall, 2-5 planes, corresponding to station 2, 6, 10, 14, and 18, were measured. The axial locations of various planes are shown in Figure 5.6. The actual measurement locations are shown in Figure 5.7.

The data measured here give temperature distributions. To further document concentration distributions of coolant migration, and further compare with the surface effectiveness values introduced in the previous section, the non-dimensional temperature (recovery) coefficient, θ, is introduced. It is arranged in a similar format to that of the surface film cooling effectiveness, as defined in Eq. (5.3).

$$\theta = \frac{T_{y,z} - T_m}{T_c - T_m} \tag{5.3}$$

One thing to highlight is its distinct physical relationship to film cooling effectiveness on the surface. The film cooling effectiveness shows the cooling efficiency on the surface by migration of coolant downstream of the injection hole. Instead, the recovery coefficient shows concentration distribution while coolant migrates downstream of the hole (x/D=0).

Table 5.2: In-passage Temperature Measurements.

Plane	1	2	3	4
Location (x/D)	2	6	10	14
Measurement Points	136	136	136	136

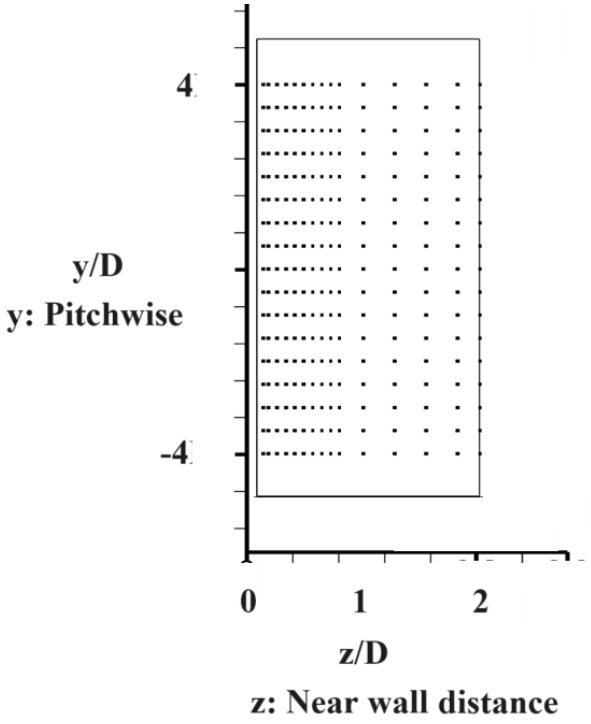

Figure 5.7: Measurement grid for thermal measurements. Note that all planes are taken with the same grid resolution.

Chapter 6. Experiment qualification

This chapter details the experimental work performed to qualify the wind tunnel used in this study. First, the approach flow profile is characterized. Then, the results of surface film cooling effectiveness are compared with the literature.

6.1 Characteristics of flow

This section introduces flow physics related to measurement, including approach flow velocity, turbulence intensity, boundary layer thickness, flow, and coolant density, etc. These parameters are reported in Table 6.1.

Table 6.1. Approach Flow Characteristics

Approach Flow Hole Reynolds Number, Re_D	9500
Turbulence Intensity, TI	0.8%
Mainstream Velocity, U_m	11.78 m/s²
Density Ratio, DR	0.97
Approach Flow Temperature, T_m	23℃
Coolant Temperature, Tc	33℃
Boundary Layer Thickness, δ	15mm

Approach flows discrete hole Reynolds number and velocity

The discrete hole inlet Reynolds number, Re_D, based on the mainstream velocity and film cooling hole diameter, is 9.5×10^3. The viscous effect is negligible at this Reynolds number. The Reynolds number is calculated as Eq. (6.1), as:

$$Re_D = \frac{\rho U_m D}{\mu} \tag{6.1}$$

Where, U_m is the mainstream velocity, D is the hole diameter, ρ is density and μ is the dynamic viscosity.

The main flow velocity, U_m, as measured by a pitot tube connected to an inclined manometer, was kept at 11.78 m/s for the entire set of experiments. The pitot tube is applied to measure the velocity profiles at several downstream positions, confirming the streamwise boundary layer development with uniform approach flow.

Approach flow boundary layer thickness

The boundary layer thickness is 15 mm at -7D upstream of the hole, as documented by a pitot tube. The measurement results fit the 1/7 power law profile of a turbulent boundary layer. The profile of the boundary layer is presented in Figures 6.1 and 6.2. In addition, the boundary layer thickness and integral thickness were confirmed to match the standard zero-pressure-gradient, turbulent boundary layer development documented in the literature. The approach flow boundary layer profile is reported in Table 6.2.

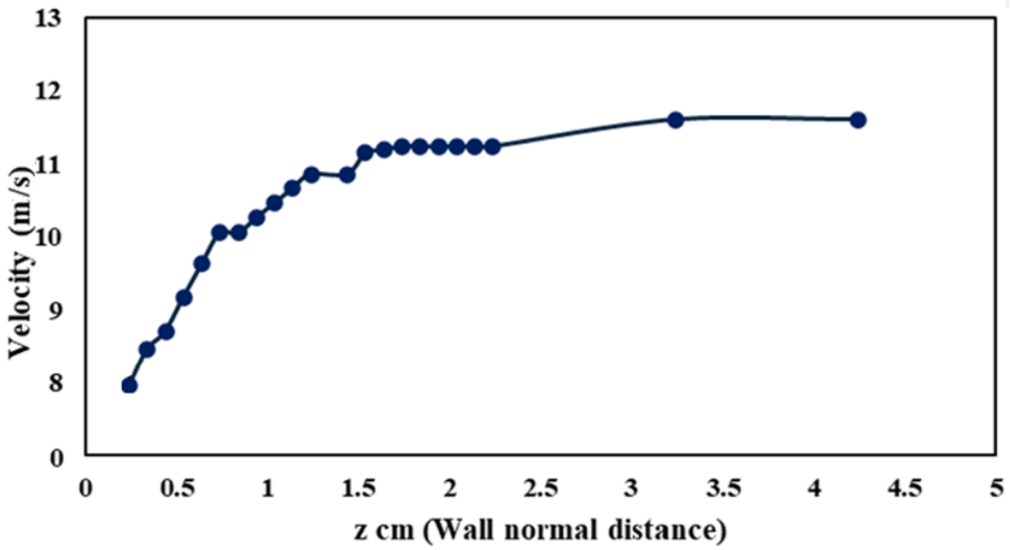

Figure 6.1: Velocity profile at x/D= -7, z/D=0. Trip is introduced at x/D=-30. No vortex generator is placed upstream for this measurement. Velocity measurement cannot be taken near the wall (origin) due to the diameter of the pitot tube. Um=11.78 m/s

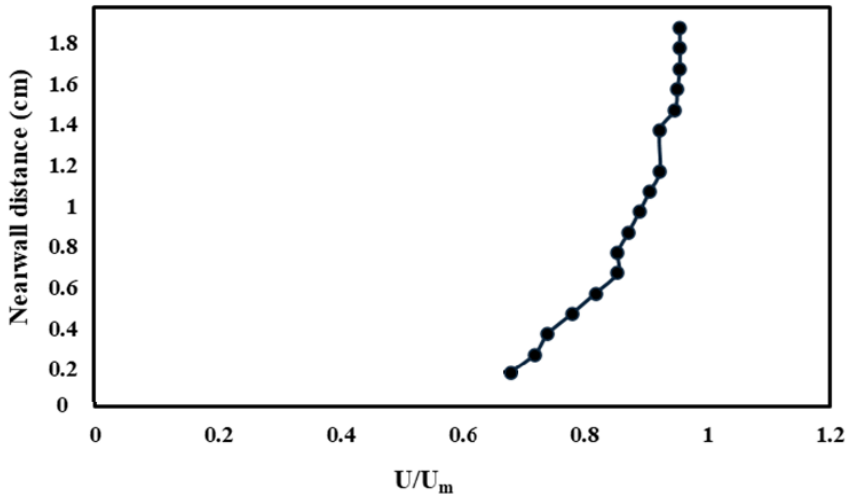

Figure 6.2: Velocity profile at x/D= -7, z/D=0. Trip is introduced at x/D=-30. No vortex generator is placed upstream. Measurement cannot be taken near the wall due to the diameter of the pitot tube. Um=11.78 m/s

Table 6.2 Approach flow boundary layer profile

	x/D = 3	x/D = 8	x/D=18
$Re\delta_1$	2167.64	4356	7124
$Re\delta_2$	210	422	691

Turbulence intensity

The turbulence intensity in this experiment is 0.8%, documented by a hotwire anemometer (TSI Inc, Model 1210). This was previously measured by Zhu, et al. (2021) on the same wind tunnel. In the engine, higher turbulence intensity induces increased mixing due to larger eddies in the boundary layer flow. Nevertheless, it is not a primary focus of this experiment when understanding the vortical interaction between various vortices. Such a condition of low turbulence intensity level is a proper simplification to extract the flow (vortical) physics of interest.

Coolant density ratio

To study mixing between the coolant with the approach flow, the coolant was heated to 33 ℃, while the approach flow temperature was at 23 ℃. This marking can distinguish the coolant from the mainstream, highlighting the concentration mixture of coolant with the mainstream. The aim of heating "coolant" here is to track the coolant migration. In reality, the coolant temperature should be smaller in the approach flow coming out of combustor.

The coolant was heated in the plenum chamber, providing a temperature greater than ambient temperature. Thus, the coolant density ratio is 0.97, a value beneath the realistic engine conditions. The effect of coolant density ratio has been fully studied in the literature. In general, increased density ratio provides better film cooling coverage, as documented by Stratton and Shih (2018). The present study, however, focuses on unsteady patterns on film cooling effectiveness. Examples are leakage flow (Chowdhury, et al., 2017), and swirl flow (Werschnik, et al., 2017). Among these studies, the density ratio is about unity, around 1.0-1.04, as the focus is on the unsteady fluid mechanics on film cooling. It is confirmed that the density ratio is not the primary parameter here, influencing the mixing mechanism of film cooling by the embedded vortex upstream.

6.2 Thermal measurement qualifications

To ensure the credibility of the present experiment, the result of the lateral-averaged adiabatic effectiveness on the surface is qualified by Anderson, et al. (2017). These two cases were performed under similar boundary layer thicknesses, turbulence intensities, hole geometries, blowing ratios (M=1.0), and Reynolds numbers. Details of these two cases are summarized in Table 6.3.

Table 6.3 Experimental Qualification

	Present Experiment	Anderson, et al. (2017)
Coolant Density Ratio, DR	0.97	1.2
(δ /D)	1.2	1.4
Turbulence Intensity, Tu	0.8%	0.5%
Free Stream Velocity, U_m	11.78 m/s	22 m/s
Hole Reynold Number, Re_D	9500	7300
Hole Geometry	10-10-10 Shaped Hole	7-7-7 Shaped Hole
Trip	3 mm	1.0 mm

The present experiment has a relatively small coolant density ratio compared to that of Anderson, et al. (2017). Thus, a relatively lower surface adiabatic effectiveness is expected in the present experiment. This is because the lighter coolant tends to lift off the surface at a smaller coolant density ratio. Nevertheless, the lateral-averaged adiabatic effectiveness from the present study shows similar trends with those of Anderson, et al. (2017). The laterally-averaged film cooling effectiveness is reported in Figure 6.3. This confirms the credibility of the present experimental results.

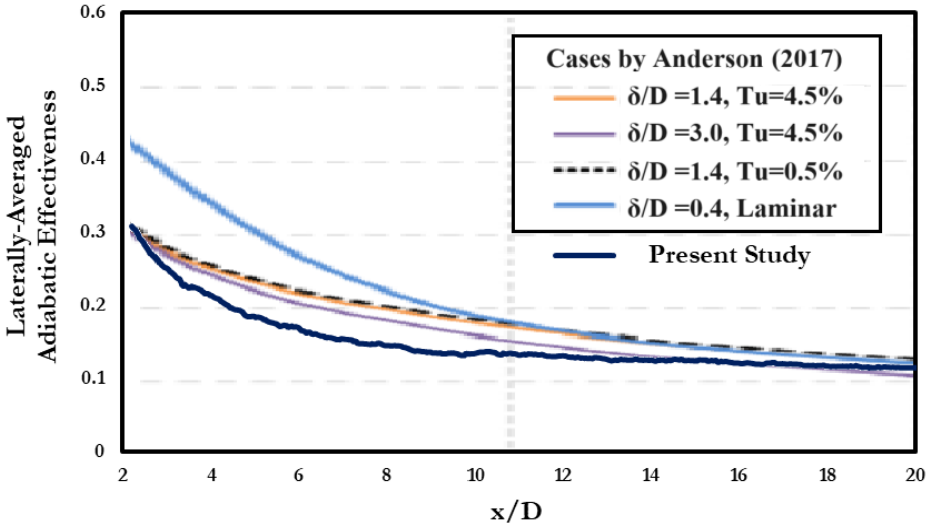

Figure 6.3: Lateral-averaged adiabatic effectiveness. Blowing ratio, M, = 1.0. A particular

focus is case Tu=0.5%, δ/D = 1.4 reported by Anderson, et al. (2017)

6.3 Time scale of on-surface coolant concentration

The on-surface measurements presented in this thesis are mostly single-shot data (based on one photograph), instead of the time-average surface effectiveness. To ensure the credibility of data, the single shot value is compared with time-averaged surface effectiveness values of various averaging time scales, as reported in Figure 6.4. It is confirmed that the surface effectiveness has nearly the same value and range whether single-shot or averaged over different and small time scales. Thus, using single shot data in the results section of this thesis doesn't influence our conclusion when interpreting the flow physics. Single shot TLC data have higher measurement variability and show some characteristics of unsteadiness of the jet in crossflow physics, such as hints of the unsteadiness of the hairpin vortex and shear layer vortices. These cannot be observed when taking time-average data over a larger time scale.

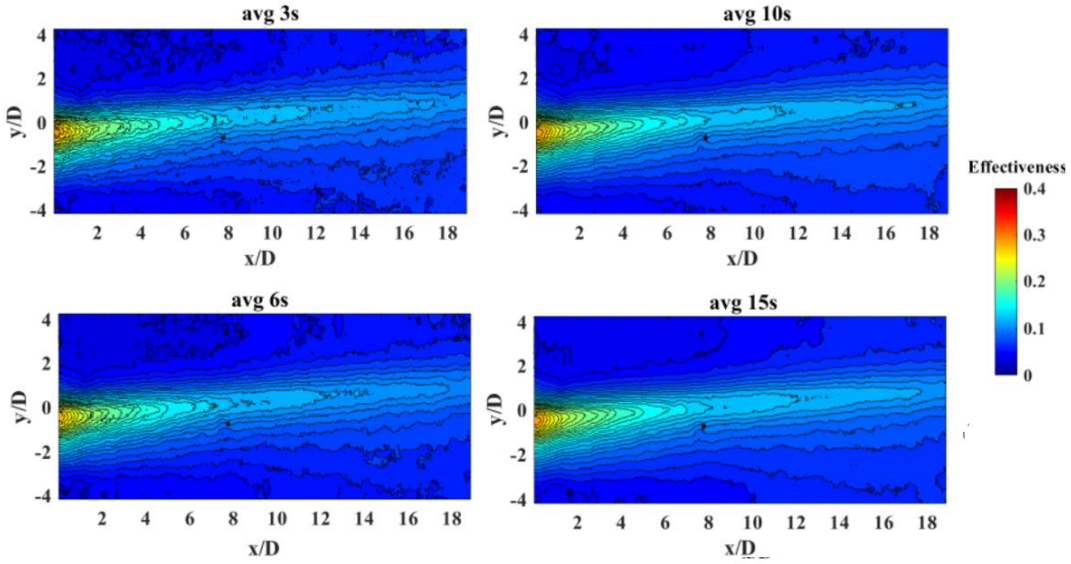

Figure 6.4: Time-average surface film cooling effectiveness over various time scales. Sampling times are 3 seconds, 6 seconds, 10 seconds, and 15 seconds. The vortex generator is located at y/D=-1.5. The hole is skewed at -30∘, away from the approach flow.

Chapter 7. A literature study on endwall discrete hole film cooling in the turbine cascade

7.1 Motivation

Beyond combustor coolant carried from upstream and injected ahead of the passage, endwall discrete hole film cooling is another important technique to reach full coverage film cooling. Its importance is to apply endwall discrete hole film cooling supplementing the upstream injection. This relies on careful consideration of the passage secondary flows at various locations of the turbine passage, and its interaction as a jet in crossflow produced by the discrete holes' coolant injections. As discussed in Chapter 2, an area that deserves more attention is the upstream portion of the passage, upstream of the throat, where the horseshoe vortex is the major secondary flow feature. Such regions are too complicated to study in detail both experimentally or computationally, thus a theory about the vortical effect between the passage secondary flow and discrete hole injection is proposed, to justified flat plate results in a turbine cascade. Then, the proposed theory is further verified with evidence in the turbine cascade. Overall, the aim of this section is to identify the prominent flow pattern between the secondary flow and discrete hole injection. This serves as a crucial step to develop strategies for discrete hole film cooling to apply in the realistic turbine cascade environment.

In the following section, the significant secondary flow patterns are first discussed in the context of endwall discrete hole film cooling. A particular focus is upstream of the passage throat, where the pressure leg of the horseshoe vortices is lifting off the surface. Then, the interaction between the passage secondary flow by discrete hole film cooling is stated. The difficulty is to understand such complex features in detail. Alternatively, accessible information by present experimental techniques in the literature are introduced. Accordingly, a theory about vortical interaction with the passage flow is presented. Then, related data in the turbine cascade are discussed, focusing on the validation of these data.

7.2 Secondary flow features in the turbine cascade

The key secondary flow feature on the passage endwall is the migration of the pressure leg of the horseshoe vortex from the pressure side to the suction side surfaces

due to the crossflow driven by the pressure gradient. As the pressure leg of horseshoe vortex migrates, it sweeps into the endwall crossflow and is further energized. The path of its migration is named the endwall separation line. Endwall crossflow is the primary feature downstream of the endwall separation line. Alternatively, the horseshoe vortex is the major feature upstream of the endwall separation line. Once it reaches the suction side surface, it stagnates at the wall and further lifts off the surface. The pressure leg of horseshoe vortex sweeps the mainstream to the suction wall, resulting in increased heat transfer and reduced film cooling on the endwall and suction surface.

Energized by the endwall crossflow, the pressure leg of the horseshoe vortex grows stronger as it goes further downstream in the passage. The pressure leg of the horseshoe vortex, also called the passage vortex, governs migration of secondary flow features near the suction side surface. An example is the suction leg of the horseshoe vortex, driven by the pressure leg of the horseshoe vortex. This is because the suction leg possesses a different sense of rotational direction from that of the pressure leg. Another important flow feature here is the suction side corner vortex. As the pressure leg of the horseshoe vortex lifts off the suction surface after its traverse, the crossflow stagnates at the suction endwall corner, forming an intense suction corner vortex which is responsible for increased heat transfer on the suction wall.

Alternatively, film cooling is a technique to provide cooling by injection through discrete holes, separating the mainstream hot gas from the surface in the vicinity of the hole. A prominent feature is the counter rotating vortex pair (CRVP) generated by discrete hole injection (described as a jet in crossflow, as pictured in Figure 2.2). When the hole is not oriented in the direction of the approach flow, one of the two vortices will strengthen and dominate the coolant injection pattern, while the other will weaken. This hole-orientation effect on discrete hole injection forms an asymmetric vortex pair, as an important part in developing a descriptive theory for this section of the thesis. The rotational direction of this asymmetric vortex is similar to those of both the round hole and shaped hole injection geometries, though the shaped hole shows distinctively higher film cooling effectiveness due to its reduced jet penetration and enhanced lateral spreading.

7.3 The effect of vortex rotational direction

The flow for endwall discrete hole film cooling is an addition to the passage

secondary flow in the turbine cascade and the jet in crossflow is created from the discrete hole injection. The nature of this problem is three-dimensional and unsteady and is far more complicated than our current capacity to measure or analyze in detail. Nowadays both experimental and numerical techniques are insufficient to understand such flow features in detail.

One way to address this is to extract the most representative flow features and estimate (model) the flow interactions. A particular focus here is the vortical interaction of various vortices. Details of this theory are shown in Figure 7.1. It is suspected that vortices with similar senses of rotational direction will merge. The smaller vortex (coolant injection vortex) will be swept into the larger vortex (i.e. a horseshoe vortex leg), and will further energize the horseshoe vortex. Accordingly, reduced film cooling is expected. Instead, vortices that possess different senses of rotational direction will not merge. Then the coolant injection vortex is suppressed, or held on the surface by the horseshoe vortex and, thus, retains coolant on the surface. Such cases show increased film cooling effectiveness values. More information about this vortical interaction can be found in Section 2.2.5.

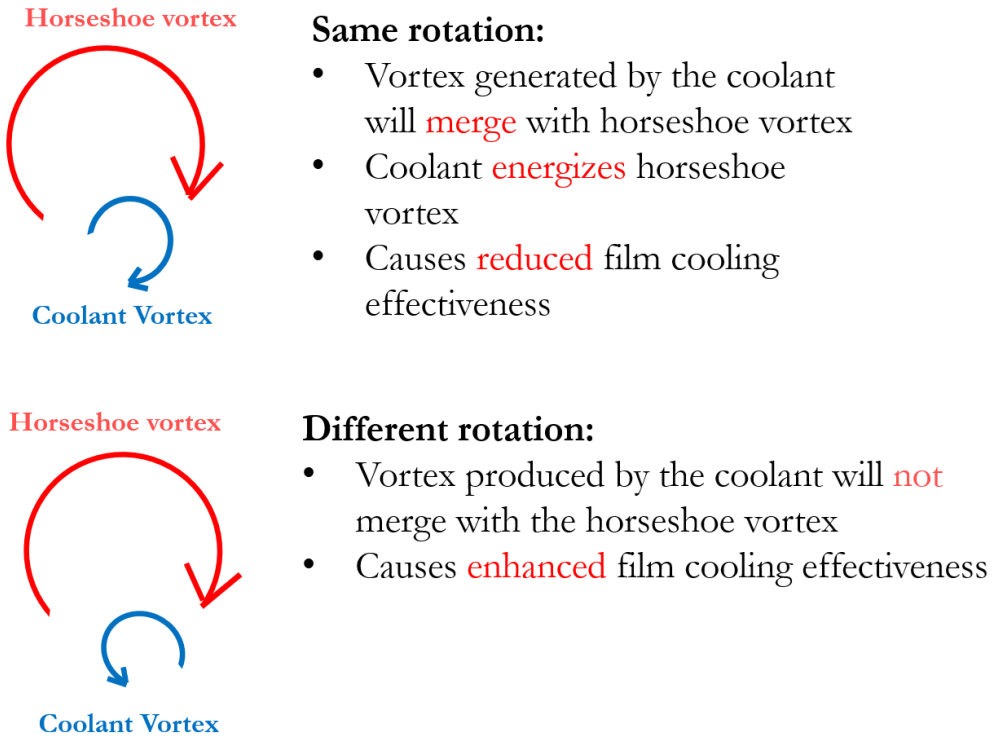

Figure 7.1: Interaction between horseshoe vortex and coolant vortex generated from discrete hole injection.

Another item to highlight is to apply the nature of vortical interaction from the case

of a flat plate, where it can be easily studied, into the turbine cascade, which is more representative of the engine. The oil dot visualization technique shows the approach flow direction near the endwall upstream of a discrete hole. The hole axis direction, combined with the flow direction given by the oil dot visualization, can determine the hole orientation angle with respect to the approach flow, to consider along with the coolant vortex rotational direction and its intensity information. One thing to point out is that oil dot visualization can only show approximately the approach flow direction around the discrete hole, as the crossflow is not uniform due to the geometric complexity of turbine passage. Thus, there is a major difference between cases on the flat plate and the turbine, since the flat plate wind tunnel cannot model geometric effects and the resultant crossflows in the turbine cascade. Details of angle between the approach flow direction and hole axis direction are pictured in Figure 7.2.

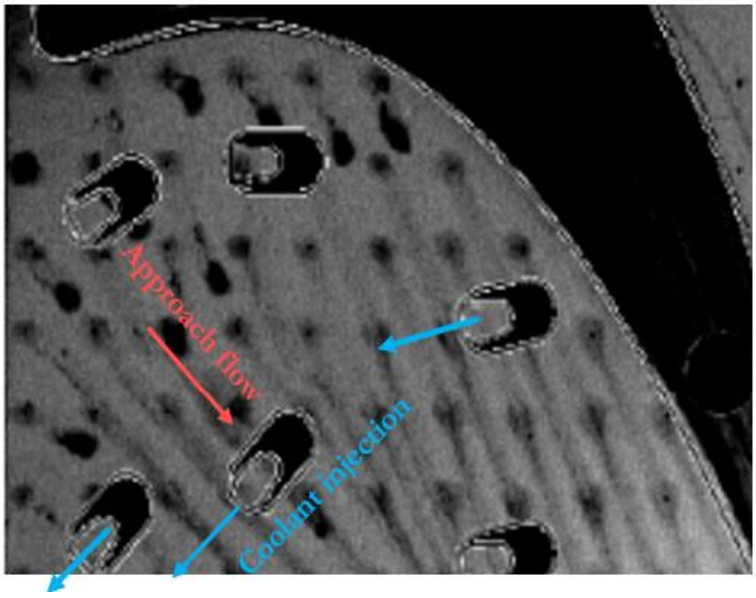

Figure 7.2: Hole orientation angle on the endwall of turbine cascade. The red angle is approach flow direction, documented by oil dot visualization (Papa, et al., 2011). The hole axis (blue angle) is the direction of coolant injection (Stinson, 2019).

7.4 Vortical rotational effect in the turbine cascade

The theory of vortical effects on vortex rotational direction was proposed in the previous section. This section intends to apply this theory into various turbine cascade cases in the literature. Representative cases are Friedrichs, et al. (1999), Colban, et al. (2008), Stinson (2018), and Yang, et al. (2018). One thing to note is that studies in discrete hole film cooling rely heavily on particular needs from industry, such as cooling on the endwall. These studies normally only cover specific regions on the endwall surface. Thus,

more than one study is cited here. It is expected that these discussions can serve as baselines for the full coverage of endwall discrete hole film cooling.

Discrete round hole by Friedrich et al. (1999)

One of the earliest and representative works for discussing discrete hole film cooling is reported by Friedrichs, et al. (1999). They examined cooling performance with discrete holes uniformly distributed within the turbine passage at x/Cax = 0.1, 0.3, 0.5, and 0.7. In Figure 7.3, the pressure leg of the horseshoe vortex, the suction leg of the horseshoe vortex, the passage vortex, and the endwall separation line are clearly seen. Their results show that discrete round hole injection shows poor film cooling effectiveness on the surface upstream of the endwall separation line, as reported in Figure 7.4. One of the major features from their data is the streamwise delay that moves downstream of the endwall separation line identified at x/C_{ax} = 0.3 and 0.5, where the path of the pressure leg of the horseshoe vortex overlaps with a discrete round hole. It appears that these "delays" of the endwall separation line had not been previously recognized, and, thus, the design communities generally believed that the discrete round hole was ineffective in retaining the coolant under the strong secondary flow and horseshoe vortex in this region. In general, as a result, discrete, round holes were rarely introduced upstream of the endwall separation line due to the reduced film cooling effectiveness observed by Friedrichs, et al. (1999).

The major reason for reduced film cooling effectiveness and the delay of the endwall separation line can be explained by the effect of vortical interaction proposed in the previous section. The relative rotational direction of the coolant injection vortex can be decided by the angle between the approach flow, as documented by oil dot visualization and the hole axis direction. Here, it is suspected that the coolant vortex possesses a similar sense of rotational direction with that of the pressure leg of horseshoe vortex. Thus, the coolant vortex is swept into the horseshoe vortex, further energizing it and causing reduced film cooling effectiveness immediately downstream of the hole. Here, as the horseshoe vortex is energized by the coolant vortex, it is expected to grow in scale and size. Thus, the horseshoe vortex core is expanded, causing the "delay" or "shift" of the endwall separation line, as reported in Figure 7.3. This case is one of the pieces of evidence used for discussing the vortical rotational direction effect on the interaction in the turbine cascades of the horseshoe vortex and vortices generated by coolant injection.

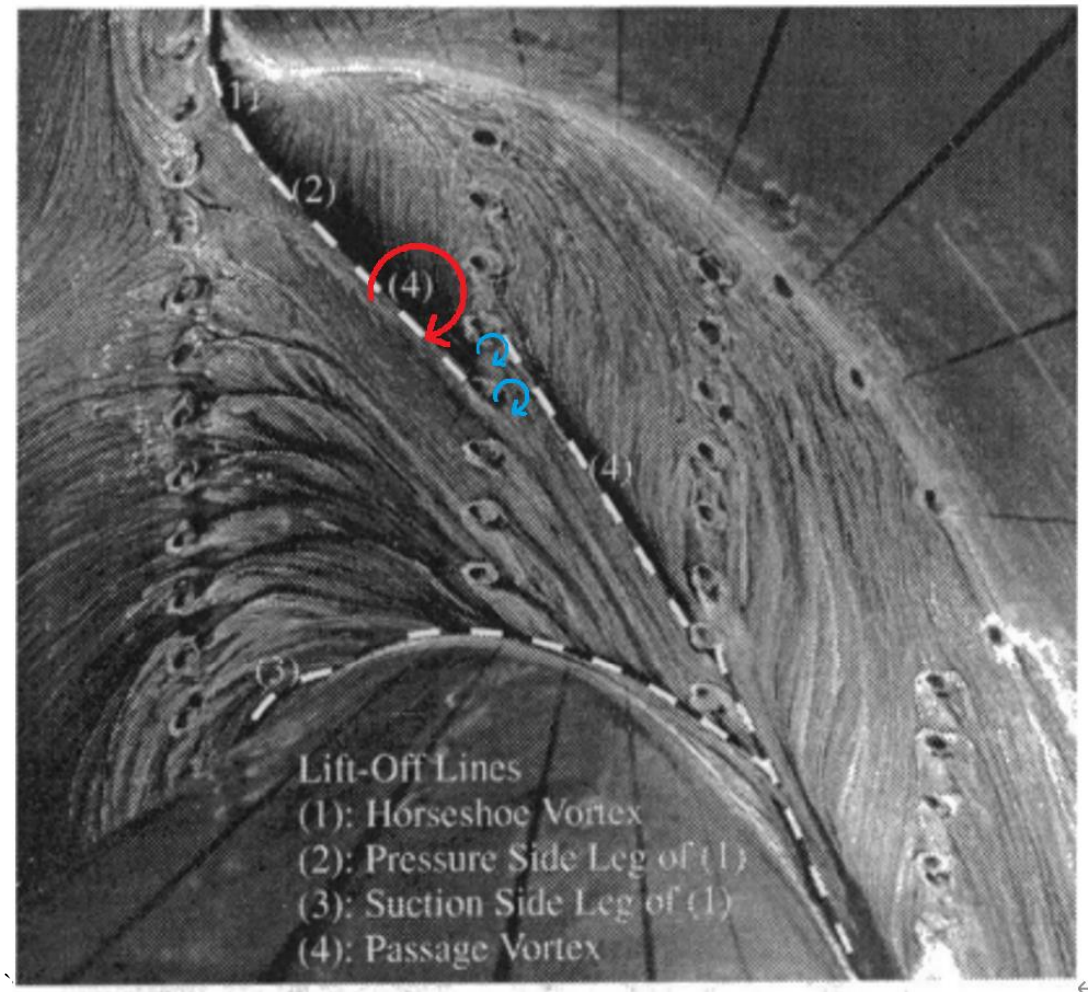

Figure 7.3: Oil and dye surface flow visualization for the film-cooled cascade endwall, reported by Friedrichs, et al. (1999). Red arrow, added to the original picture, is a rotational direction of the pressure leg of the horseshoe vortex. Blue arrow, added to the original picture, is a rotational direction of coolant injection vortex.

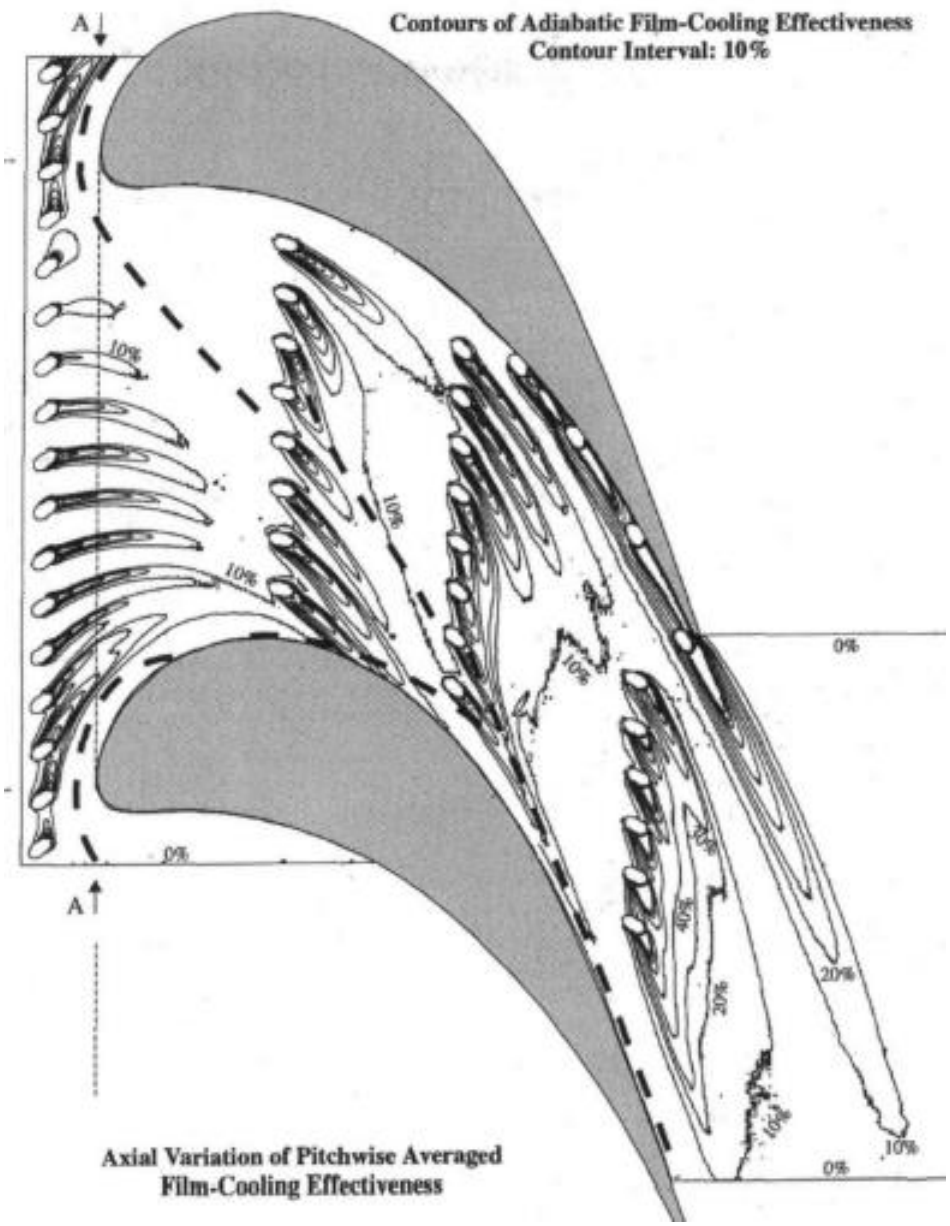

Figure 7.4: Endwall film cooling effectiveness measured using the ammonia and diazo technique (Friedrichs, et al., 1999). Reduced film cooling effectiveness can be identified at x/Cax = 0.3 and 0.5, at the path of the pressure leg of horseshoe vortex.

Discrete shaped hole from Colban, et al. (2008), Stinson (2018), Barigozzi, et al. (2005), and Yang, et al. (2018)

As shaped holes are known to provide better film cooling effectiveness than round holes due to their reduced jet penetration and increased lateral spreading (Goldstein, et al., 1974), various representative works about endwall discrete shaped hole are discussed here. The foci are on the upstream of the passage pressure and suction side surfaces, and are taken from results of Colban, et al. (2008), Stinson (2018), and Yang, et al. (2018). Details about these works were described in Chapter 2.

Important areas for use of discrete, shaped holes are upstream in the passage on the pressure side. Here, the shaped hole is oriented to inject flow away from the pressure wall in cases documented by Colban, et al. (2008), and Stinson (2018). Their results show reduced film cooling effectiveness. This is partially because the vortex generated by the coolant injection possesses a similar sense of rotational direction to that of the horseshoe vortex. Thus, the coolant vortex is swept into the horseshoe vortex, and horseshoe vortex is energized, as shown in Figure 7.5 and Figure 7.6. In contrast, an opposite case is reported by Yang, et al. (2018) and Barigozzi, et al. (2005), in which the hole is oriented so that coolant is injected toward the pressure surface. It is suspected that the coolant vortex core possesses, in this case, a different sense of rotational direction compared to that of the horseshoe vortex. Thus, suppressed coolant on the endwall surface and resulting increased film cooling effectiveness are found in their data, as shown in Figure 7.7 and Figure 7.8. Here, the nature of vortical rotational direction can describe an interaction between the horseshoe vortex and vortex generated by coolant injection in the turbine cascade.

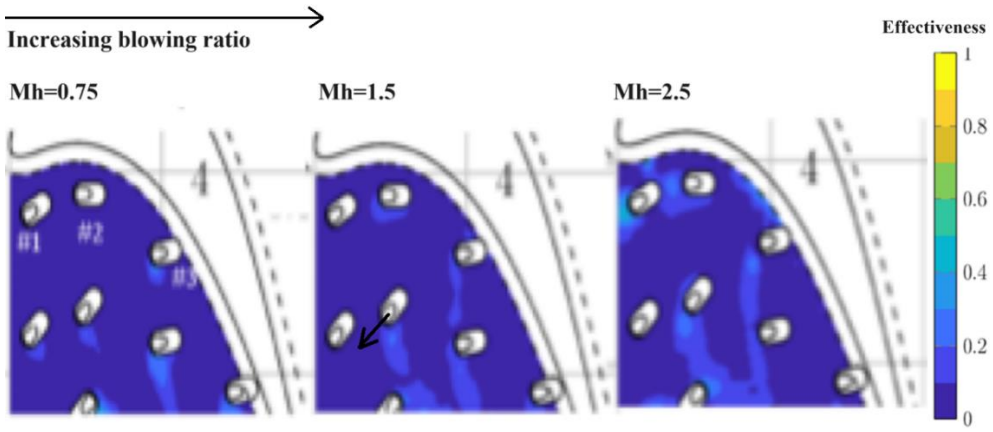

Figure 7.5: Film cooling effectiveness on the pressure side of passage reported by Stinson (2018). Holes were oriented away from the pressure wall (as shown by coolant path). The black arrow, added to the figure, shows the direction of the coolant flow along hole axis.

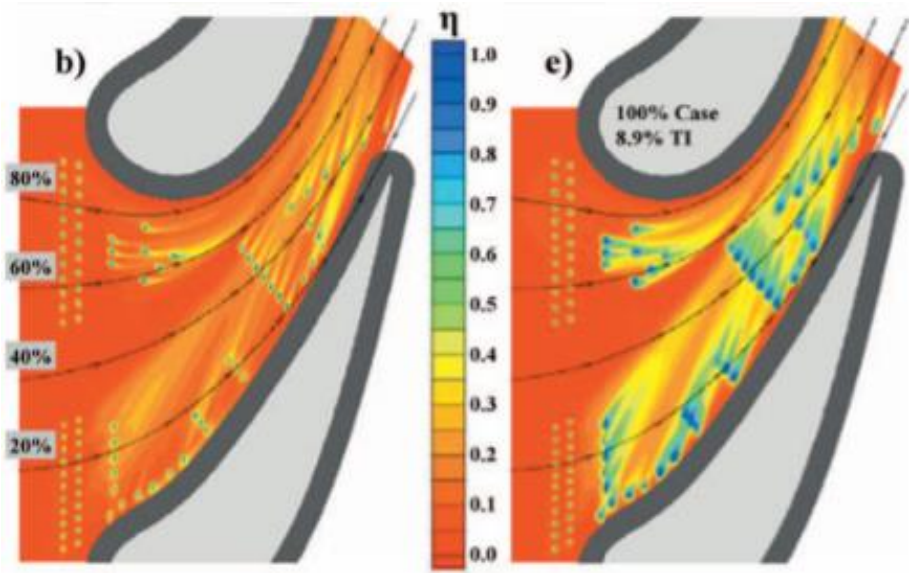

Figure 7.6: Effectiveness contours at high freestream turbulence for the cylindrical hole (b) and fan shaped hole (e). Reported by Colban, et al. (2008). Blue represents higher coverage. Holes are oriented away from the pressure wall. Coolant mass flow rate is the same as the mainstream mass flow rate.

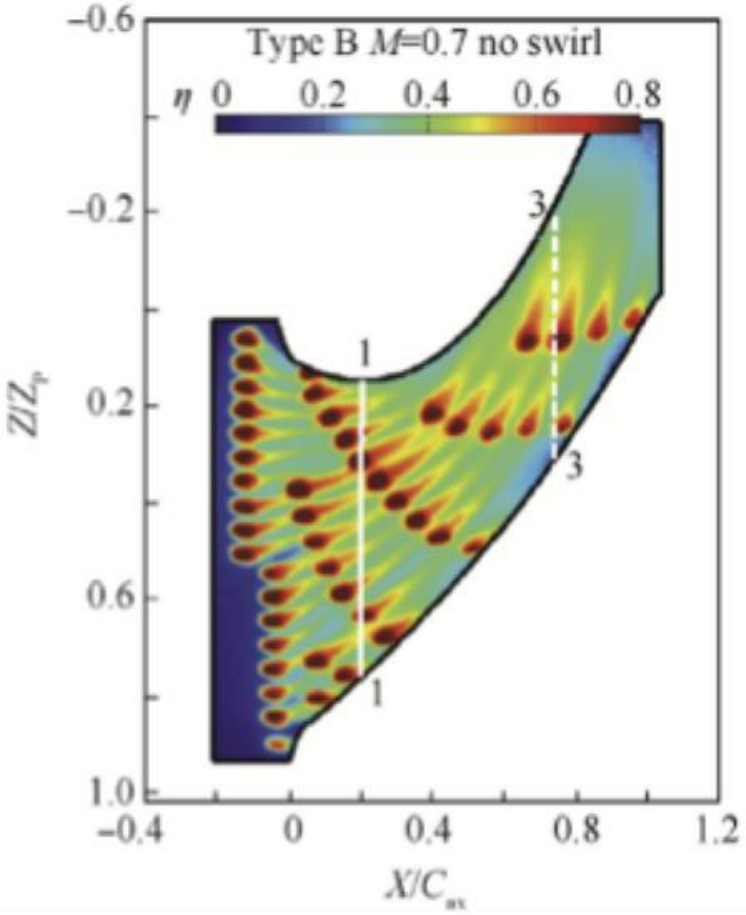

Figure 7.7: Film cooling effectiveness distribution on the endwall (Case for M=0.7), (Yang, et al., 2018). Holes are oriented toward the pressure wall. Red represents higher

coverage.

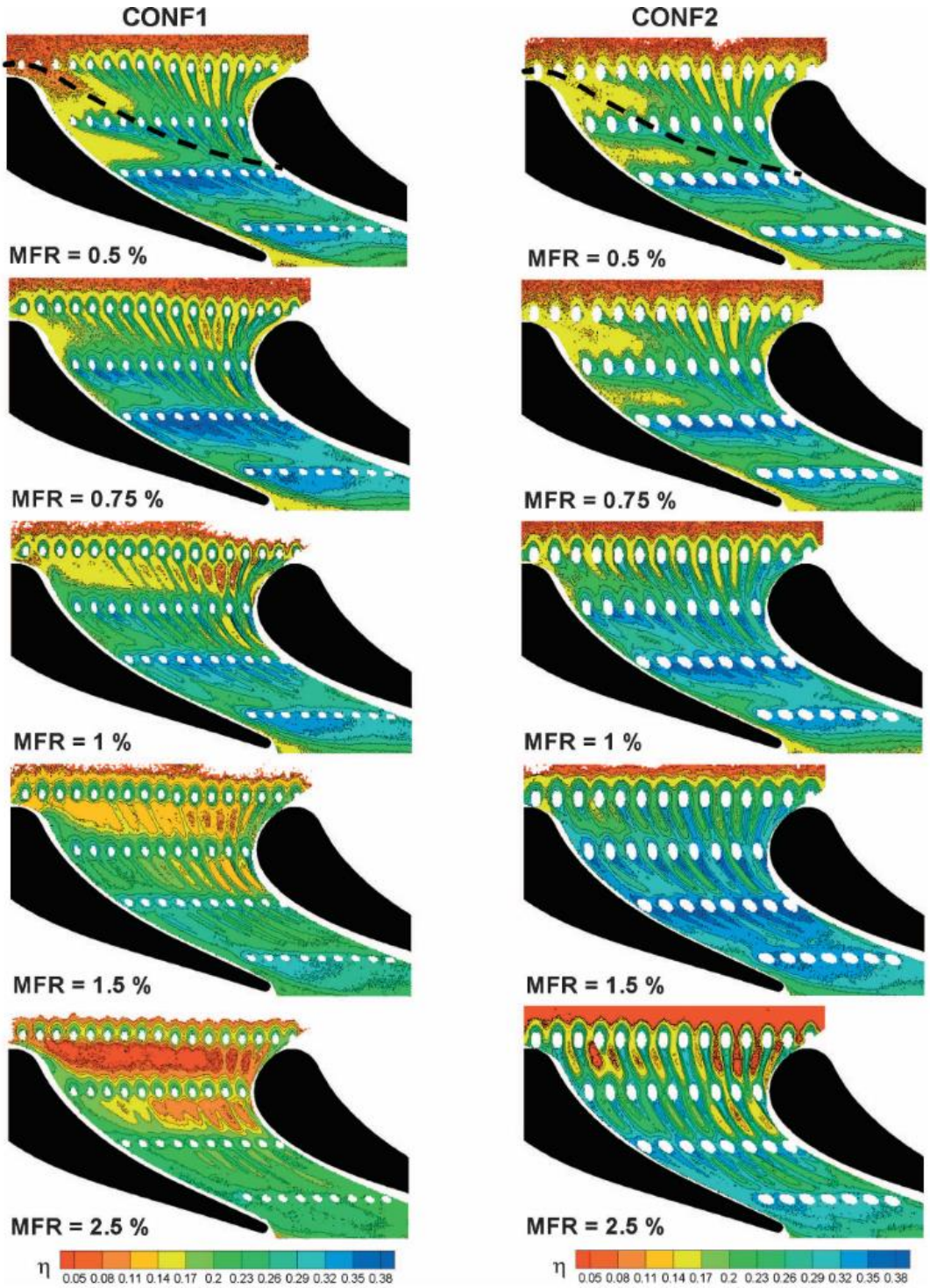

Figure 7.8: Adiabatic effectiveness distributions for the different injection conditions and the two geometries. Reported by Barigozzi, et al. (2005). CON1 is for discrete, round holes, and CON2 is for discrete, shaped holes. Shaped holes near the upstream pressure side of the surface are oriented toward the pressure wall. MFR is coolant mass flow to mainstream mass flow ratio.

Another area to highlight is the upstream region of the passage on the suction surface. Evidence for performance of discrete shaped holes in this area has recently been reported by Stinson (2018), as, apparently, the only source of information of such in the literature. The theory presented herein is that the results of Stinson's doctoral work are directly beneficial in viewing this region. Herein, the author uses Stinson's data as the foundation for the present discussion regarding vortex effects on cooling. Stinson examined discrete shaped hole injection with holes oriented away from the suction surface. The approach flow direction is clearly shown in Figure 7.9. The shaped hole locations and hole axes are shown in Figure 7.10. The approach flow direction, and the shaped hole axes, show the hole orientation angle with the angle of approach flow, and the rotational direction of the coolant wake from the shaped hole. It is suspected that the coolant vortex possesses a similar sense of rotational direction to that of the suction leg of horseshoe vortex. Thus, the coolant vortex is swept into the suction leg of the horseshoe vortex. Near the suction side surface, it is expected that the pressure leg dominates the suction leg as these two vortices possess different senses of rotational direction. More details about this can be found in Chapter 2.1. In general, competing effects are expected between the pressure and suction legs of the horseshoe vortex, as shown in Figure 7.11. As coolant blowing ratio is increased from 0.75 to 2.5, the suction leg of horseshoe vortex is further energized by coolant and the suction leg resists lift-off of the pressure leg and remains on the endwall. Accordingly, the pressure leg of the horseshoe vortex might remain on the surface, instead of lifting off. Additionally, the corner vortex possibly weakens or disappears when M reaches 1.5. The delay of suction leg lift-off is shown in Figure 7.10. Overall, the importance of Stinson's dataset is that it demonstrates the potential to cool the triangular region that possess high heat transfer (mass transfer) coefficients on the suction wall, as documented by Goldstein and Chen (1987), without intentionally placing cooling holes there. The streamline track of the pressure leg of the horseshoe vortex (also called passage vortex) and resultant high mass (heat) transfer region are pictured in Figure 7.12. This is because the pressure leg of the horseshoe vortex didn't reach the suction wall and, thus, had the potential to inadvertently improving cooling of the suction surface.

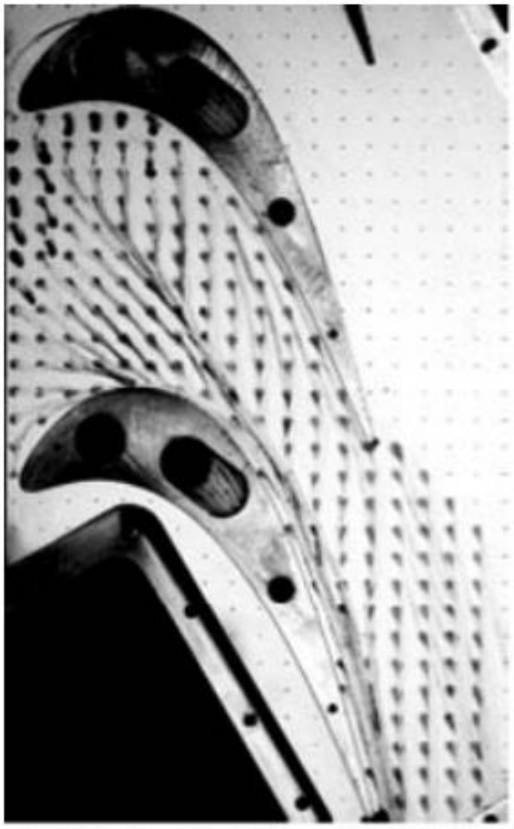

Figure 7.9: Oil dot visualization shows the approach flow directions on the endwall of the turbine cascade (Papa, et al., 2011).

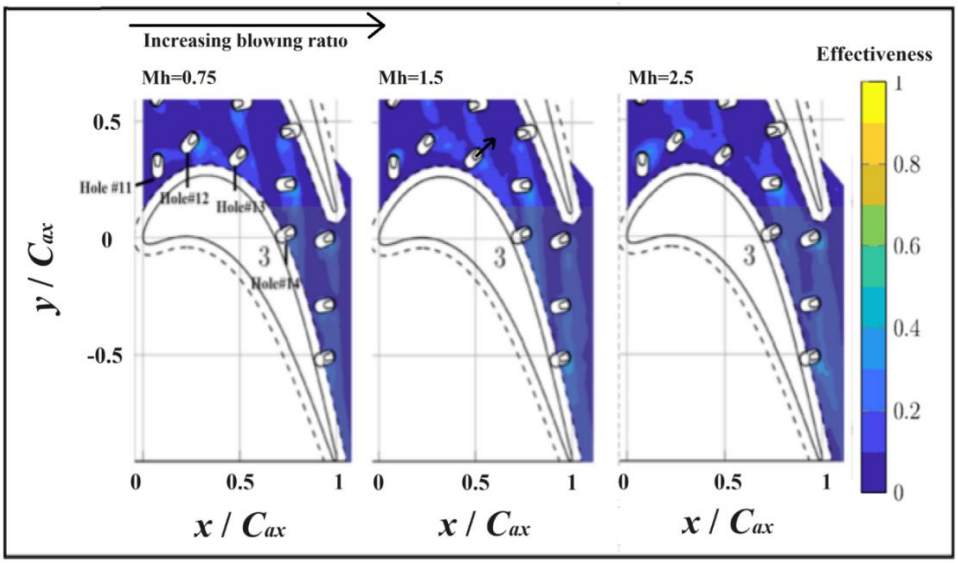

Figure 7.10: Film cooling effectiveness values for the "perpendicular" holes near the suction side of the passage. The coolant average velocity to passage average velocity ratios, blowing ratios, Mh, are shown for three cases of Stinson (2018). The hole numbers of Stinson (2018) are identified, and the airfoil is the central airfoil #3. The angle is the coolant injection direction.

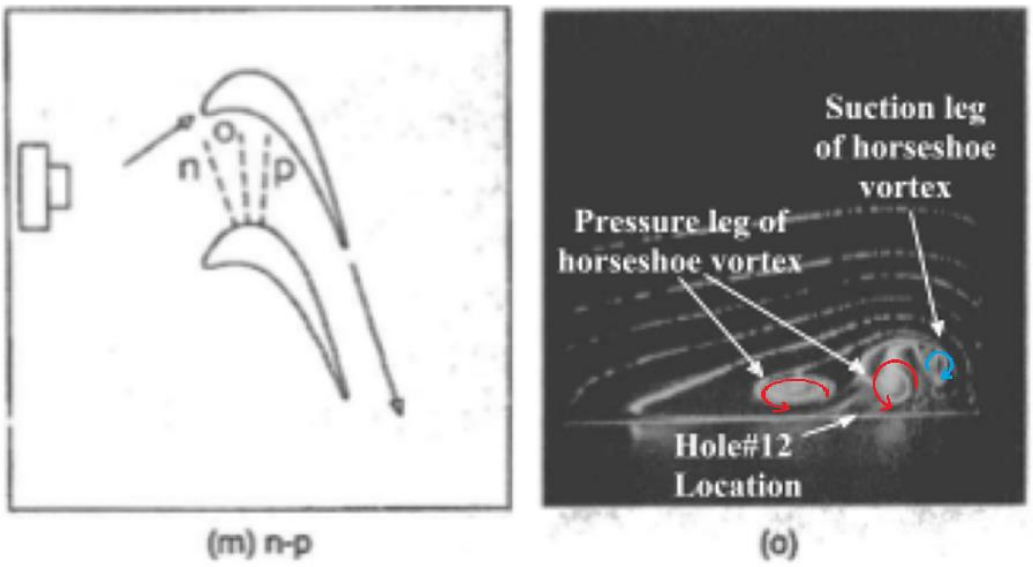

(a)

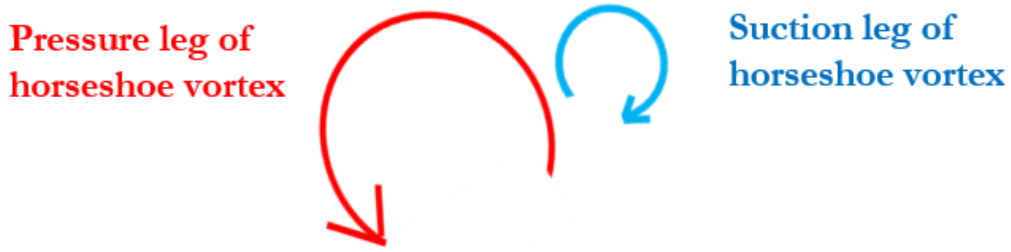

(b)

Figure 7.11: (a) Smoke visualization (right figure) at location of plane O (left figure). Reported by Wang, et al. (1997). The red arrow, added to this picture, is the rotational direction of the pressure leg of the horseshoe vortex. (b) Competition between the pressure and suction legs of the horseshoe vortex.

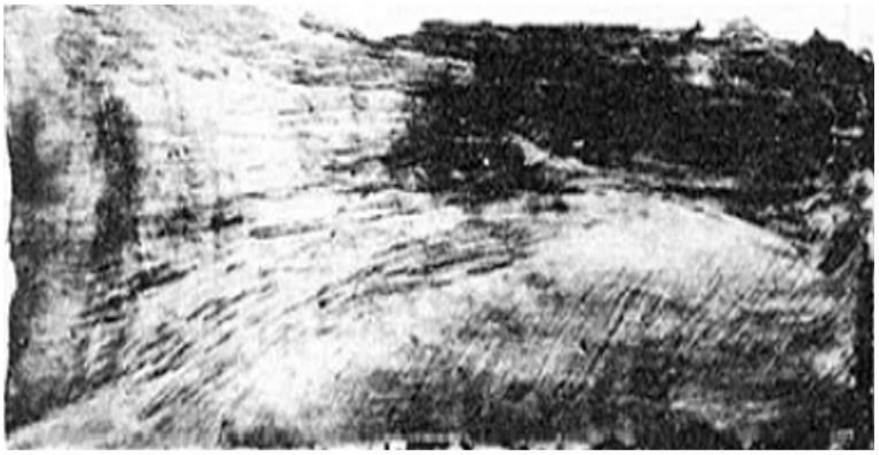

(a)

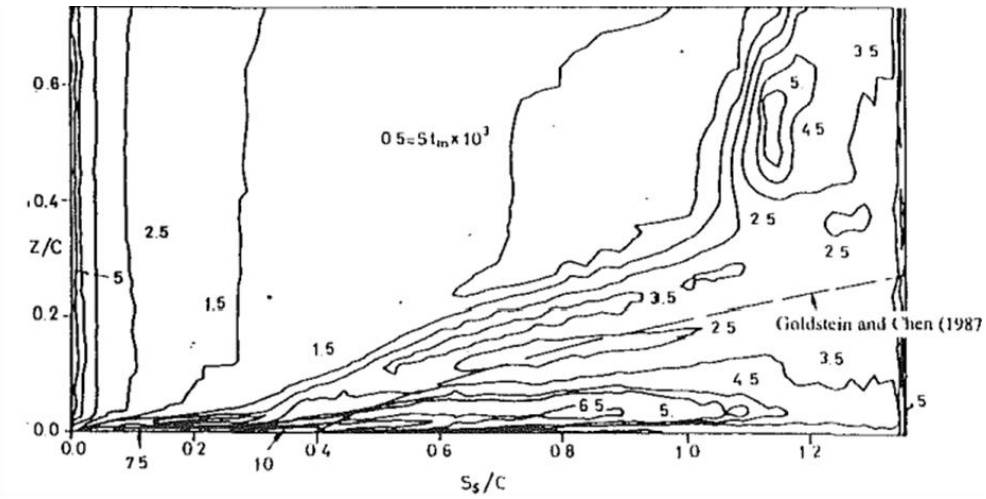

(b)

Figure 7.12: (a) Streamline tracks on the convex (suction) surface of a gas turbine blade (b) Suction surface Sherwood Number (mass transfer equivalent to Nusselt number). Reported by Goldstein and Chen (1987).

Similar physics on modifying the suction leg of horseshoe vortex can be found at Han and Goldstein (2006). They investigated the leading-edge fillet (modification) effect near the suction side. Their results show that the suction leg of the horseshoe vortex is weakened by adding a fillet to the leading edge, resulting in enhanced heat transfer on the suction wall. A possible explanation is that, as the suction leg of horseshoe vortex is weakened, the competition between pressure and suction legs is no longer prominent. Thus, the pressure leg is further strengthened as it reaches the suction wall, causing increased heat transfer on the suction wall.

7.4 Conclusion

The objective of this chapter is to show how to improve endwall film cooling by discrete hole injection, striving to reach full coverage endwall film cooling. An area that deserves more attention is upstream and near the passage throat, especially on the pressure side and suction side. Accordingly, the interaction of passage secondary flow vortices and endwall discrete hole film cooling injection vortices is investigated through a literature survey. Here, the predominant secondary flow feature is the horseshoe vortex. The discrete hole generates a major asymmetric vortex that dominates the coolant vortex rotational direction when the holes are oriented away from the wall and skewed to the approach flow direction on the endwall.

Describing such complicated physics between passage secondary flow and jet in crossflow relies on proper simplification of the problem. The key is to identify the representative flow pattern that drives such interaction. The importance of vortex relative rotational direction between the horseshoe vortex and coolant injection vortex is highlighted by the results from flat plate wind tunnel experiments. Then, such vortical interaction is justified with the evidence of film cooling effectiveness on the endwall from the turbine cascade. Oil dot flow visualization, coupled with discrete hole orientation patterns, offers a unique perspective to describe the coolant vortex at the exit of discrete hole on a turbine endwall.

The competing effect was found when the horseshoe vortex has a different sense of rotational direction to that of the vortex generated at coolant injection. Such a case shows enhanced film cooling effectiveness, as the coolant injection vortex is restrained to the endwall due to different vortex rotational direction. Such cases are particularly significant near the leading edge at the pressure side, an area that is challenging for coolant coverage due to the presence of the pressure leg of the horseshoe vortex. This application is especially important on the first stage of the rotor because of the rotational effect and the resultant skewed inlet boundary layer flow. Examples for distinct vortex rotational directions and increased film cooling effectiveness values near the pressure side of the surface can be found at Barigozzi, et al. (2005) and Yang, et al. (2018).

Alternatively, the merging effect was found when the horseshoe vortex had a similar sense of rotational direction relative to that of the vortex generated at coolant injection (the "coolant vortex"). In such a case, the coolant vortex is swept into the horseshoe vortex, energizing the horseshoe vortex. Though intuitive, such cases were considered to not be

important for cooling the turbine endwall as the coolant lifts off the surface. However, they seem to provide a unique way to modify the passage secondary flow in the turbine. This is, possibly, the most important finding of this thesis. The only pieces of evidence in the literature to describe this can be found in Stinson (2018), when discrete shaped holes distributed near the suction surface were oriented to emit flow away from the suction wall. The several findings can be addressed as:

i) Modifying the coolant blowing ratios can control the intensity of the suction leg of horseshoe vortex, and, in turn, promote the competing effect between the pressure and suction legs of the horseshoe vortex. The most prominent evidence can be found, when increasing the coolant blowing ratio from 0.75 to 1.5 and 2.5, and the suction leg is lifted and shifted, delaying it downstream.

ii) Energizing the suction leg of the horseshoe vortex properly can weaken the influence of suction corner vortex. This feature is identified from Stinson's data at a coolant blowing ratio, Mh, of 1.5, since enhanced film cooling effectiveness is found at the endwall-suction corner, where the literature generally agrees that the suction corner vortex should be located. This finding is significant as it has the potential to explain to gas turbine designers the high heat transfer near the suction corner with the present design. A possible reason for such phenomenon is the competing effect between suction leg and pressure leg of horseshoe vortex. Since the suction and pressure legs of the horseshoe vortex remain on the surface, the crossflow cannot reach the suction corner. Thus, the suction-endwall corner vortex is weakened, or possibly eliminated.

iii) Energizing the suction leg of the horseshoe vortex can introduce competition between the suction leg and pressure leg vortices. As the suction leg of horseshoe vortex is further energized, it can resist the upwash from the pressure leg of the horseshoe vortex, and remain on the endwall surface. Thus, it can obstruct the pressure leg of the horseshoe vortex as it reaches the suction wall and maintains the pressure leg of the horseshoe vortex on the pressure side of the passage endwall. Accordingly, reduced heat transfer and improved cooling is expected on the suction wall, a long-lasting problem reported by Goldstein and Chen (1987). This is because the pressure leg of the horseshoe vortex can no longer reach the suction wall, forming a passage vortex that may damage the suction wall with enhanced heat transfer. Such modification of the suction leg of the horseshoe vortex is found also from the leading-edge fillet modification study reported by Han and Goldstein (2005). Though this design with fillets is aimed at weakening the suction leg of

the horseshoe vortex, it causes increased heat transfer coefficients on the suction wall due to a strengthened pressure leg of horseshoe vortex by weakened competition between the suction leg of the horseshoe vortex and the pressure leg of the horseshoe vortex.

Overall, the present section discusses vortical interaction between different vortices. Such phenomena can be found in various cases, from the pressure and suction legs of horseshoe vortex in the turbine cascade, to the horseshoe vortex and coolant injection vortex on the turbine cascade endwall, to the incoming near-wall vortex produced by the vortex generator and a coolant injection vortex on the flat plate wind tunnel, and to the counter rotating vortex pairs emerging from the jets in crossflow. From the author's point of view, this is one of the most elegant and fascinating themes one can observe from nature, as such an interaction is governed by universal laws of nature in various scales and scenarios. As stated in the start of "The mathematical Principles of Natural Philosophy (1846) / Book III – Rules", Newton proposed four rules of reasoning in philosophy, as the effective methodology for handling unknown phenomena in nature and reaching toward explanations for them. The four rules of the 1726 edition are cited here, applied in this thesis, as:

1. *We are to admit no more causes of natural things than such as are both true and sufficient to explain their appearances.*

2. *Therefore, to the same natural effects we must, as far as possible, assign the same causes.*

3. *The qualities of bodies, which admit neither intensification nor remission of degrees, and which are found to belong to all bodies within the reach of our experiments, are to be esteemed the universal qualities of all bodies whatsoever.*

4. *In experimental philosophy we are to look upon propositions inferred by general induction from phenomena as accurately or very nearly true, notwithstanding any contrary hypothesis that may be imagined, till such time as other phenomena occur, by which they may either be made more accurate, or liable to exceptions.*

7.5 Future work

Evidence in the literature about endwall discrete hole film cooling in the turbine cascade is discussed in the context of vortex rotational direction. Nevertheless, more effort is

necessary to further our understanding about the importance of the vortical effect between the horseshoe vortex and coolant injection vortex.

One important work that requires validation is the film cooling effectiveness on the suction wall when discrete, shaped holes are oriented away from the suction side surface. Such experimental data can validate the competing effects between the pressure and suction legs of the horseshoe vortex and the resultant delayed lift-off of the suction leg of the horseshoe vortex.

Another important item to note is the vortical effect on the impingement vortex, as reported by Nawathe, et al. (2023). Presently, the literature includes sufficient evidence of the effects vortices have on passage secondary flows, as proposed by Wang, et al. (1987). Nevertheless, the effect of endwall discrete hole film cooling on an alternative passage secondary flow system (impingement vortex) cannot be found in the literature. Such a case requires an increased inlet injection momentum ratio as reported by Papa, et al. (2011), or the additional upstream combustor coolant, as reported by Nawathe, et al. (2023), that were not thoroughly covered in the literature, until recently, are not covered in this report.

A comparative study between the leading-edge fillet modification and case of the discrete shaped hole injection oriented away from the suction wall and near the suction surface can be justified. This is proposed as a continuation. The leading-edge fillet weakened the suction leg of horseshoe vortex, causing increased heat (mass) transfer on the suction wall. The discrete, shaped hole injection oriented away from the suction wall and near the suction surface strengthens the suction leg of horseshoe vortex and, thus, leads to reduced heat transfer on the suction wall. Both of these settings modify the suction leg of the horseshoe vortex, either intensifying or weakening it and, thus, influencing cooling of the suction wall.

An important application is on the upstream portion of the passage on the pressure surface, where the coolant injection vortex has a distinct rotational direction with respect to the pressure leg of the horseshoe vortex. Such a case is significant as the leading edge of rotor endwall near the pressure surface remains an urgent thermal issue for the gas turbine designer. Further investigations on use of the shaped hole near the leading edge of the pressure surface are necessary when considering the coolant injection vortices rotational directions and the rotation of the pressure leg of the horseshoe vortex.

An interesting perspective to supplement the present work is to describe in detail the

interaction of the horseshoe vortex and the coolant injection vortices. These data may include velocity measurements or coolant concentrations in a turbine cascade. In reality, such velocity data are constrained by the spatial resolution for the unsteady features between the interaction of various vortices. Though the in-passage coolant concentration measurement can characterize the influence of coolant injection vortices (generated from the discrete hole injection) on passage secondary flow development, it requires further investment in human labor and funding an alternative design of the endwall discrete hole film cooling scheme in the test rig of the linear cascade wind tunnel might be sought.

A step forward is to describe the interaction between the horseshoe vortex and the coolant injection vortices on a flat plate in the wind tunnel. Such an experiment provides a chance to investigate vortex interaction on coolant migration and, possibly, relate the experimental results to the turbine cascade. Such experiments on the flat plate wind tunnel are the second focus of this thesis, as discussed in Chapter 8.

Chapter 8. Experiments on coolant concentration as modified by vortical effects on a flat plate in a wind tunnel

8.1 Motivation

The effects of vortical activity in the turbine cascade are discussed in the previous chapter. It is expected that the relative rotational direction of vortices is a critical feature. This section aims to characterize the vortical effect on coolant migration between the horseshoe vortex and vortices generated by coolant injection (named as "coolant vortices" in this report). Accordingly, the effects of near-wall vortex locations, hole geometries, hole orientations, and coolant blowing ratios are investigated experimentally on the flat plate in a wind tunnel. Experimental results taken here serve as solid evidence for vortical interaction that can be taken to the turbine cascade environment, to further support the theory proposed in the previous chapter.

To model the turbine cascade with the flat plate, the horseshoe vortex is simulated with a vortex generator placed upstream of the film cooling hole. The coolant injection vortices are produced by injection through a hole that may have its axis in-line with the approach flow, or skewed to it. Round holes and shaped holes are applied. They have universal patterns described by coolant vortex rotational directions, as noted by Aga, et al. (2008) and Haydt and Lynch (2018). The advantage of the flat plate wind tunnel is that it allows taking detailed coolant migration data with high spatial resolution and allows further investigation of the most important secondary flow features, revealing vortical effects on coolant migration. One thing to note is that many minor secondary flow factors are disregarded, including variations in the inlet turbulence intensity (which for this study is low), variations in the inlet flow Reynolds number, and variations in approach flow boundary layer thickness.

In the following sections, the effect of an incoming vortex on round hole injection is discussed. These cases can clearly describe the migration of coolant due to an incoming near-wall vortex, simulating a leg of the horseshoe vortex. Then, the effects of vortex relative rotational direction and coolant blowing ratios are introduced.

8.2 Vortical effect on coolant migration

Parallel (aligned with the flow) round hole and shaped hole cases

The first item to introduce is the influence of vortical flow on coolant migration. This section aims to verify the theory about vortical interaction and serves as a baseline for discussion in the following chapter. To achieve this, the effects of an incoming vortex on parallel (aligned with the flow) holes are performed, as the simplest cases within the experimental parameter space.

The hole axes is parallel to the approach flow direction. The coolant blowing ratio, M, is 1.5. The rotational direction of the incoming vortex is clearly shown in Figure 8.1 (clockwise when viewed from the upstream). Round hole and shaped hole geometries are tested. The surface film cooling effectiveness Eq. (5.1) and in-passage coolant migration are reported. (Figure 8.1)

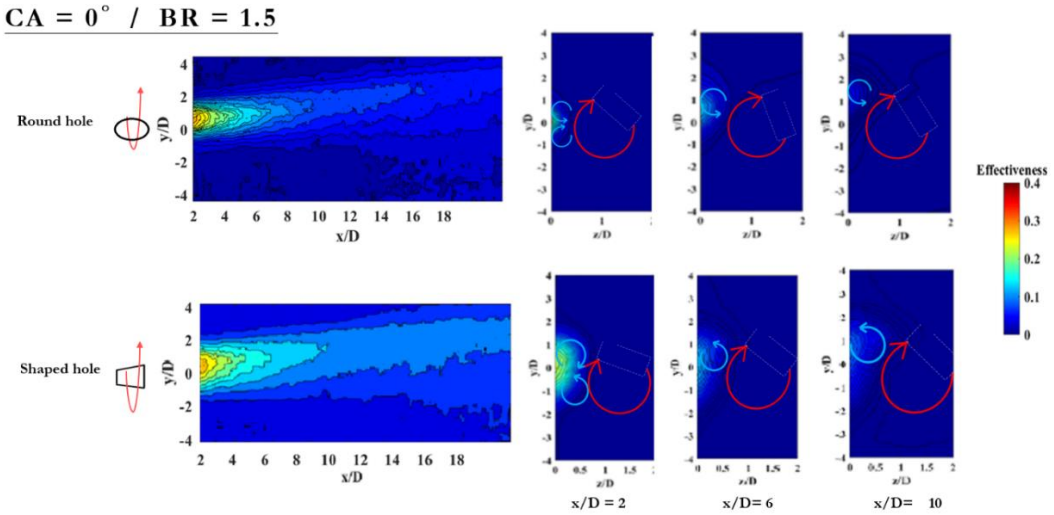

Figure 8.1: Parallel (aligned), shaped hole and round hole. Hole is oriented at 0°. The vortex generator is located at y/D = -0. The migration of coolant is documented at cross planes x/D=2, 6, and 10. The coolant blowing ratio is 1.5.

A counter rotating vortex pair (CRVP) was generated by the cylindrical hole. Here, it is shown that the coolant vortex that possesses a similar sense of rotational direction to that of the incoming vortex will merge. A coolant vortex core that possesses a distinct sense of rotational direction remains on the surface and is driven by the incoming vortex. The reduced film cooling effectiveness is due to the strong jet penetration, lifting the coolant off the surface.

Alternatively, the anti-counter rotating vortex pair is produced by the discrete shaped hole.

Similar to the round hole case, it is observed that the coolant injection vortex has a similar sense of rotational direction and will merge with the incoming vortex. The coolant injection vortex core that has a different sense of rotational direction to that of the approach flow vortex will not merge with the approach flow vortex. This coolant vortex, however, is still governed by the local incoming vortex, as the size of this incoming vortex is much larger than the coolant vortex. The comparison of these two cases (CRVP and anti-CRVP) is shown in Figure 8.2.

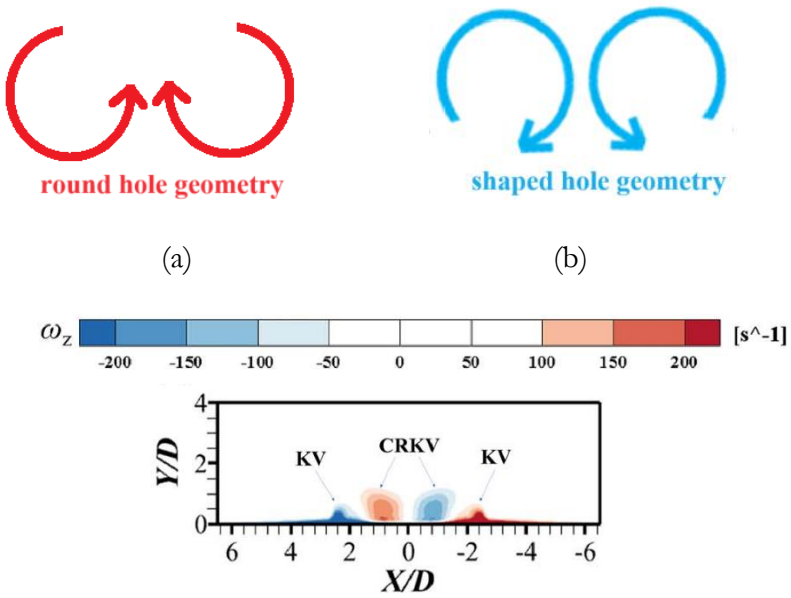

Figure 8.2: Comparison of vortex pair from round hole and shaped hole geometries. (a) Round hole geometry – counter rotating vortex pair, as shown in Figure 2.2 (b) Shaped hole geometry – anti-counter rotating vortex pair (c) Shaped hole geometry – anti-counter rotating vortex pair, reported by Cui et al. (2022). KV, kidney vortex, is counter rotating vortex pair. CRKV, counter rotating kidney vortex, is anti-counter rotating vortex pair.

In general, the experimental data taken on the flat plate show an effect of the incoming vortex on coolant migration and can support the principle about vortex interactions discussed above. As supporting evidence for the theory proposed in the previous section about the turbine cascade, the vortex with a similar sense of rotational direction will merge with the approach flow vortex. This applies to either of the two legs of the horseshoe vortex near the pressure side surface that has merged as one major pressure leg of the horseshoe vortex. Another case is the merging between the coolant-generated vortex and

the horseshoe vortex present in a turbine cascade. Alternatively, vortices possessing distinct senses of rotational directions will not merge. These include the pressure and suction legs of the horseshoe vortex, the pressure leg of horseshoe vortex, and corner vortex, and the horseshoe vortex with coolant injection generated vortex in the turbine cascade. It is expected that all these vortices, of various scales and either in a turbine cascade or on a flat plate, should be governed by a universal principle, regarding vortex rotational directions.

The key difference between the round hole and shaped hole cases is the relative rotational direction of the counter rotating vortex pair. One item to highlight is the counter rotating vortex pair (CRVP) from the round hole. The center of the vortex pair possesses an up-wash flow vector, showing stronger jet penetration and resultant reduced film cooling effectiveness. An opposite case is the anti-counter rotating vortex pair from the shaped hole. The center of the vortex pair possesses a down-wash flow vector, driving coolant toward the surface. The difference between the central up-wash flow vector (round hole) and central down-wash flow vector (shaped hole) is the separation bubble generated in the shaped hole channel (Gunady, et al., 2021). The separation bubble in the shaped hole channel is pictured in Figure 8.3.

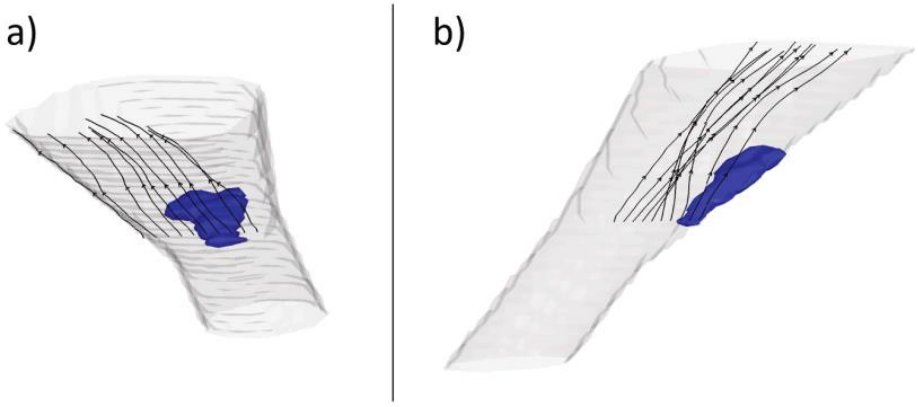

Figure 8.3: (a) The 3D extent of the separation bubble in the diffuser based on mean velocity data taken using MRV (magnetic resonance velocimetry) is highlighted in blue viewed from slightly below y/D=0 on the -z side and slightly above y/D = 0 on the +z side (b) Streamlines are shown starting near the wall upstream of the bubble (Gunady, et al., 2021).

Thus, beyond increased lateral spreading due to the expanded hole exit area, more coolant ejected from the shaped hole remains on the surface, resulting in increased film cooling on the surface. Overall, shaped holes show superior film cooling effectiveness by way of

the incoming near-wall vortex due to increased coolant lateral spreading and reduced coolant jet penetration. The experimental results for parallel (aligned with the flow) round hole and shaped hole injection can serve as evidence of results of studies by Colban, et al. (2008) and Barigozzi, et al. (2005), as shown in Figure 7.6 and Figure 7.8. Their data show that the shaped holes give superior film cooling effectiveness over that of round holes, particularly where the discrete hole is located under the pressure leg of the horseshoe vortex.

Misaligned (skewed to the approach flow) round hole and shaped hole cases

The effects of relative rotational directions between the incoming vortex and vortex generated by the coolant is further investigated. Round hole and shaped hole geometry cases are presented. The incoming vortex is located at ± 1.5D, for two cases, respectively. The coolant blowing ratio, M_h, is 1.5. The hole is oriented with skewing of its axis of ± 30°. The surface effectiveness and in-passage coolant concentrations are presented in Figures 8.2 and 8.3.

As the hole axis orients away from the approach flow direction, one of the counter rotating vortices will strengthen, and the other will weaken. The strengthened vortex will serve as the primary vortex (named as "asymmetric vortex") and dominate the weakened vortex in the coolant injection flow. The rotational direction of the asymmetric vortex is identical between the round hole and the shaped hole. The focus in this section is to consider the relative rotational direction between this asymmetric coolant-generated vortex and the incoming vortex.

First, the results for round hole cases are presented. The coolant vortex generated from the round hole has a similar sense of rotational direction to that of the incoming vortex. As shown in Figure. 8.4, reduced film cooling effectiveness is shown as the coolant injection generated vortex rotates similarly with the incoming near-wall vortex. It is suspected that the coolant is swept into the incoming vortex and energizes it. This can be clearly seen from the migration of coolant at various in-passage planes, as the size of the incoming vortex grows further downstream. Another item to discuss are cases with a distinct sense of rotational direction. As the coolant vortex possesses a different sense of rotational direction, it can resist merging with the incoming vortex. It is expected that the coolant vortex is suppressed near the surface as a result of the presence of an incoming near-wall vortex. Thus, such cases show enhanced film cooling effectiveness on the

surface.

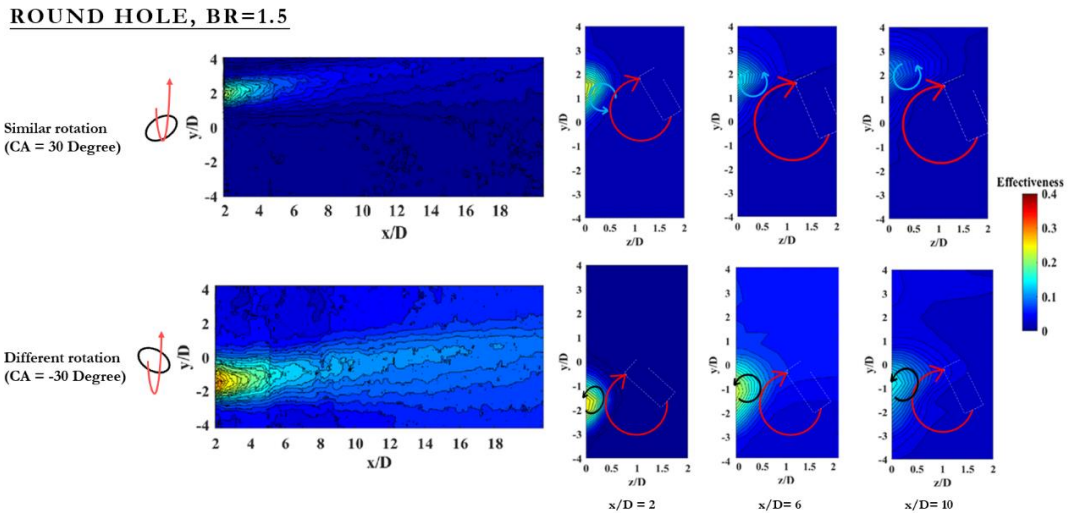

Figure 8.4: Misaligned round holes. Hole oriented at ± 30°. The vortex generator is located at y/D = ± 1.5. The migration of coolant is documented at cross planes x/D=2, 6, and 10. The coolant blowing ratio is 1.5.

The experimental results for the vorticity effect on shaped holes are next reported, as shown in Figure 8.5. Similar to those of round hole, cases with similar rotational directions between the coolant-generated vortex and the incoming vortex will show merging of these vortices. This results in reduced film cooling effectiveness on the surface. As the coolant-generated vortex is swept into the horseshoe vortex leg, the incoming vortex is further energized. One interesting feature is that the incoming vortex is more energized for the shaped hole case compared to that of the round hole case. A possible explanation for this is that the ejected coolant from the shaped hole has reduced jet penetration and enhanced lateral spreading. Oppositely, cases with a distinct sense of rotational direction were also presented. As the coolant vortex possesses a distinct sense of rotational direction, it will not merge with the incoming vortex. Instead, the coolant-generated vortex is suppressed and held on the surface to be further driven by the incoming vortex, as the coolant migrates further downstream.

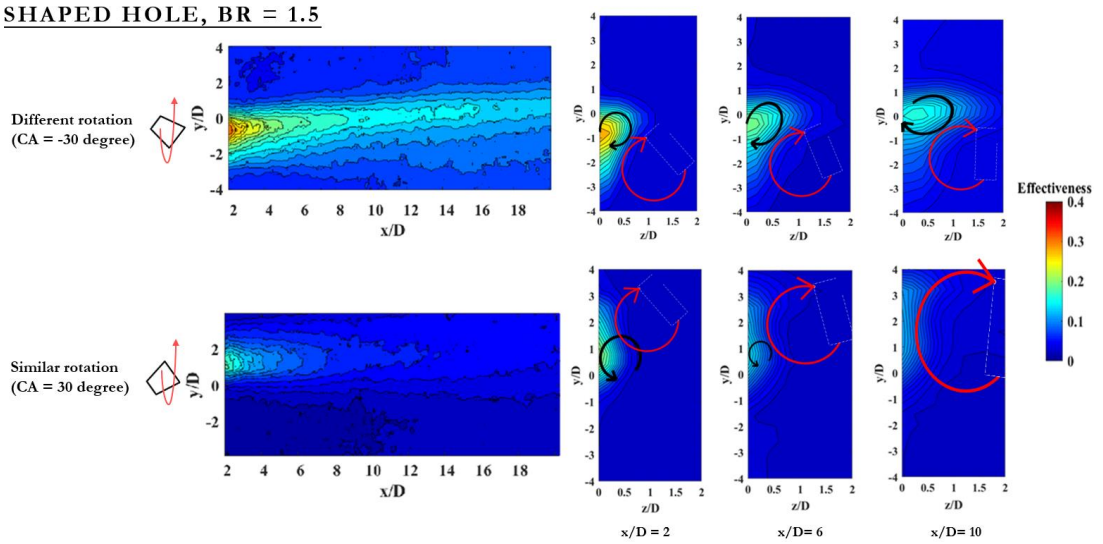

Figure 8.5: Misaligned shaped holes. Hole orients at ± 30°. The vortex generator is placed at y/D = ± 1.5. The migration of coolant is documented at cross planes x/D=2, 6, and 10. The coolant blowing ratio is 1.5.

In general, throughout all the experimental parameter space, the highest film cooling effectiveness is seen in cases with different rotational directions between the coolant-generated vortex and incoming near-wall vortex. This feature is seen from both the round hole and shaped hole data. Accordingly, the effect of the coolant-generated vortex and horseshoe vortex rotational directions is a crucial feature that should be considered in evaluating coolant coverage in a turbine cascade. In considering these features, one can see a potential to cool the leading edge of the pressure surface on the rotor platform of a turbine, a region that film cooling designers find mostly difficult to cool, as the coolant is naturally driven toward the suction surface due to the curvature effect of the airfoils and rotational effect of a rotor. Inlet injection, and the use of combustor coolant, are not possible options on the first stage of the turbine on the rotor platform compared to the first stage of the stator. These cases can show further value to the experimental results from Barigozzi, et al. (2005), and Yang, et al. (2018), where increased film cooling effectiveness can be found near the pressure side of their endwall surface. It is expected that among the cases, the coolant vortex has different senses of rotational direction with regard to the pressure leg of the horseshoe vortex.

Oppositely, reduced film cooling effectiveness is observed when there is a similar rotational direction between the coolant-generated vortex and the incoming near-wall vortex. This feature is shown in both round-hole and shaped-hole data. Though it may seem insignificant, this outcome is the most original and unique finding of all the results

of cases performed herein. Applying this in the turbine cascade cooling design has the potential to manipulate hole layouts within the passage secondary flow system observed from Wang, et al. (1997), and pictured in Figure 2.1. One practical engineering application is to energize the suction leg of horseshoe vortex by interaction with a coolant vortex having a similar sense of rotational direction. An example is to orient the discrete hole away from the suction side of surface, as reported in a case by Stinson (2018). By doing this, the energized suction leg of the horseshoe vortex can further compete with the pressure leg of the horseshoe vortex. It is expected that the suction leg and pressure leg may both remain on the surface as they compete with one another. Thus, various difficult regions to cool that possess high heat transfer rates in the traditional cooling designs of the last decades can be resolved. These include the suction corner vortex and the suction wall due to washing of the pressure leg of horseshoe vortex and the passage vortex. That is, one can expect a completely distinct secondary flow pattern in the turbine when considering the energizing effect of various vortices with similar senses of rotational direction. Overall, these cases can serve as solid evidence of the vortical effect for the Stinson (2018) shaped holes and Han and Goldstein (2005) leading-edge fillet inlet modification experimental data.

The effect of coolant blowing ratio on coolant migration

The effect of vortex rotational direction was discussed previously. The next thing to investigate is the vortical effect with various blowing ratios. The general aim of this discussion is to identify proper coolant blowing ratios for better cooling efficiency and secondary flow manipulation in a turbine. This enlightens the general trend of coolant concentration by various relative vortex rotational directions and blowing ratios. For this reason, round hole and shaped hole cases are presented. The cases are performed at coolant blowing ratios of 1.5 and 2.5. The incoming vortex is located at y/D = -1.5, 0, and 1.5, as shown in Figure 8.9.

The effect of blowing ratio on coolant migration is first investigated, with different senses of vortex rotational direction. The migration of coolant is reported in Figure 8.7. The hole oriented at -30^{o}, generating a major asymmetric coolant injection vortex dominating the coolant injection. The incoming vortex is located at y/D=-1.5 (see Figure 8.7). Here, the coolant-generated vortex has a different sense of rotational direction than that of the incoming vortex. Thus, the coolant-generated vortex will compete and be suppressed near the surface by the incoming vortex. One thing to highlight is that, as the

coolant blowing ratio increases from 1.5 to 2.5, a prominent enhancement on film cooling effectiveness is observed in the data. This enhancement on cooling is a similar pattern in the data for both of the hole geometries, though the highest cooling effectiveness is identified for the shaped hole. It is very interesting as the gas turbine community usually believes that the horseshoe vortex (incoming vortex) is an unfavorable feature for film cooling. Instead, the present data show that the near-wall vortex can, in fact, have some benefits for film cooling. Consequently, to reach a higher effectiveness for film cooling purposes, shaped holes with different rotational directions between the coolant-generated vortex and incoming vortex should be further investigated.

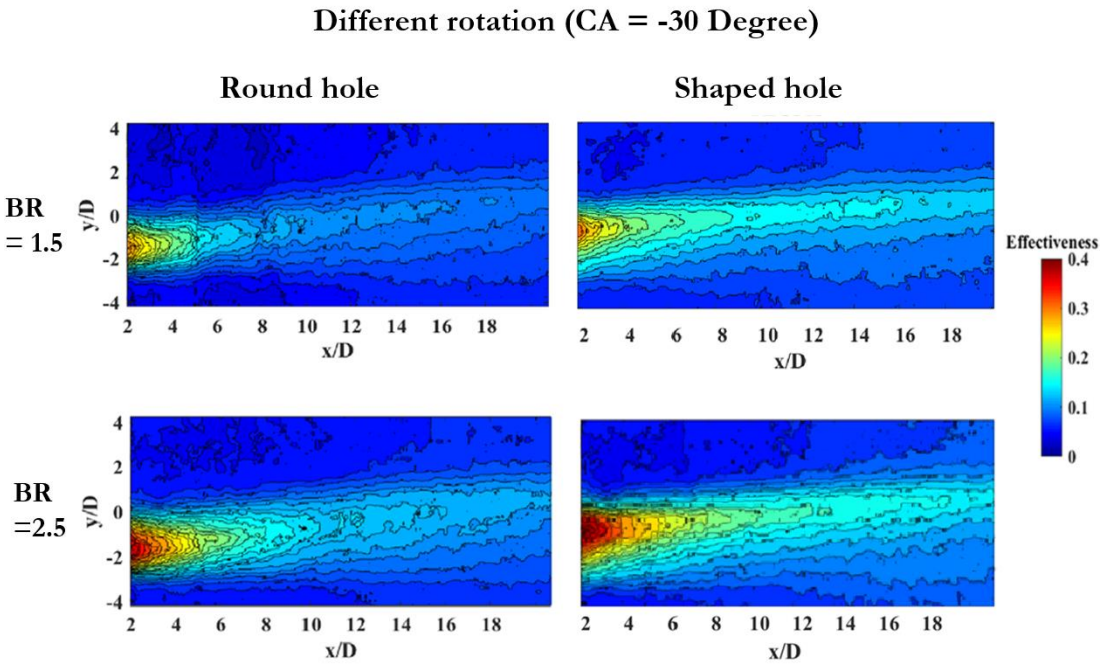

Figure 8.7: The effect of blowing ratio on coolant migration, with different senses of vortex rotational direction.

Next, the effect of coolant migration with a similar sense of vortex rotational direction and various coolant blowing ratios is experimentally investigated. The coolant concentration on the surface is reported in Figure 8.8. The hole is oriented at +30°. The incoming vortex is located at y/D=1.5. Here, the coolant vortex has a similar sense of rotational direction to that of the incoming vortex. Thus, the coolant vortex will merge with the incoming near-wall vortex and further energize the incoming vortex. Here, reduced film cooling effectiveness on the endwall surface was found with increasing coolant blowing ratios for both hole geometries. Thus, the coolants are swept into the incoming near-wall vortex, further energizing it, instead of remaining on the surface.

Though the coolant injection vortices are swept into the incoming near-wall vortex and energize the incoming near-wall vortex, resulting in a reduced film cooling effect level, energizing the near-wall vortex has the potential to manipulate and modify the horseshoe vortex system in the turbine passage. One example is to properly energize the suction leg of horseshoe vortex by the coolant-generated injection vortex to compete with the pressure leg of the horseshoe vortex and, as discussed before, cool the endwall-suction surface corner and the suction surface. Thus, the focus here is to understand the extent of energizing near-wall vortices by coolant injection with various coolant blowing ratios. With this, an interesting pattern is shown with the shaped hole and a coolant blowing ratio is 2.5. Such a case shows distinct spreading of coolant on the surface. The coolant vortex core is swept into the near-wall vortex and disappears at x/D=10. In general, increasing coolant blowing is beneficial for energizing the near-wall vortex. The shaped hole shows a stronger capacity to energize the incoming near-wall vortex compared to its performance with the round hole. Nevertheless, to identify the proper coolant blowing ratio for this purpose, more cases with various coolant blowing ratios using shaped holes should be investigated.

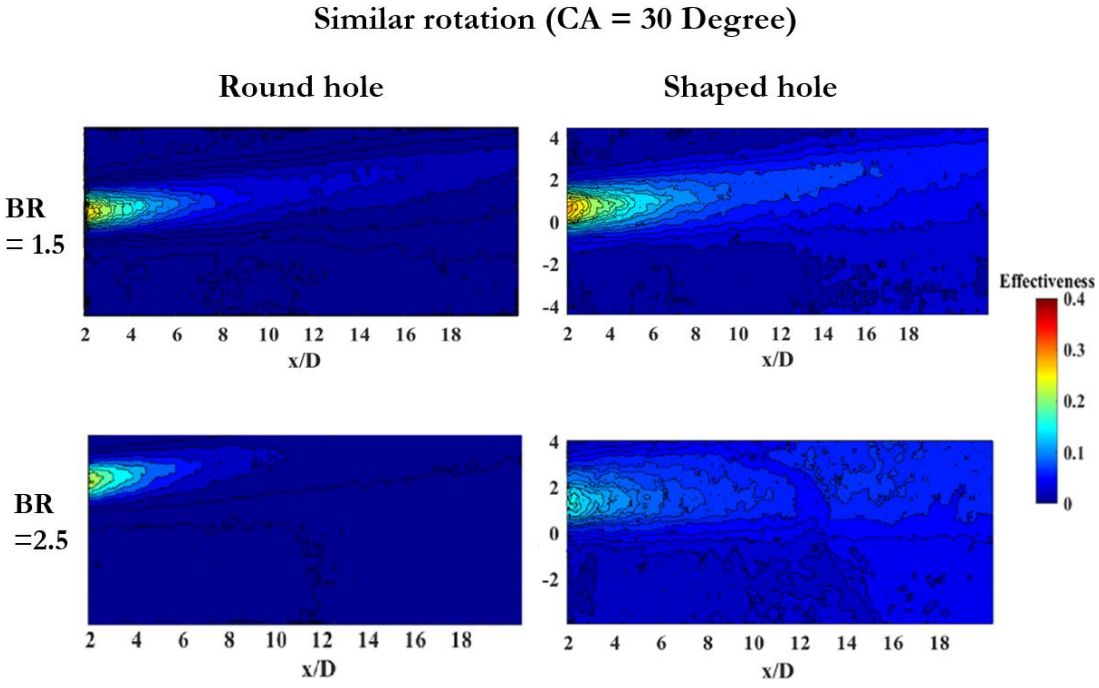

Figure 8.8: The effect of blowing ratio on coolant migration, with the same sense of vortex rotational direction.

Overall, the effects of the blowing ratio and vortex rotational direction with the shaped hole and the round hole geometries have been reported by experimental data. Increasing

the coolant blowing ratio is instrumental for cooling purposes, with various different relative rotational directions between the coolant-generated vortex and the incoming near-wall vortex. Nevertheless, more effort is necessary to identify improved hole orientations for shaped holes at different vortex rotational directions. Conversely, though increasing coolant blowing may be detrimental for cooling due to the possible blow-off from the surface, it can energize the near-wall vortex. This, in turn, has the potential to manipulate the suction leg and the pressure leg of the horseshoe vortex in the turbine. More work is needed to understand and optimize the energizing effect on the near-wall vortex, when injecting with a similar sense of coolant vortex rotation with the shaped hole.

8.3 Competing vortical effects on film cooling enhancement

Within the performed experimental parameter space, the highest film cooling effectiveness was found with a shaped hole and a different sense of rotational direction between the coolant injection-generated vortex and the incoming vortex, as reported in Figure 8.9. The shaped hole is oriented with -30° skew. Additionally, as discussed in the previous chapter, increasing the coolant blowing ratio from 1.5 to 2.5 results in enhanced film cooling effectiveness. Hence, the present section aims to identify improved hole-orientations and coolant blowing ratios, resulting in higher film cooling effectiveness values.

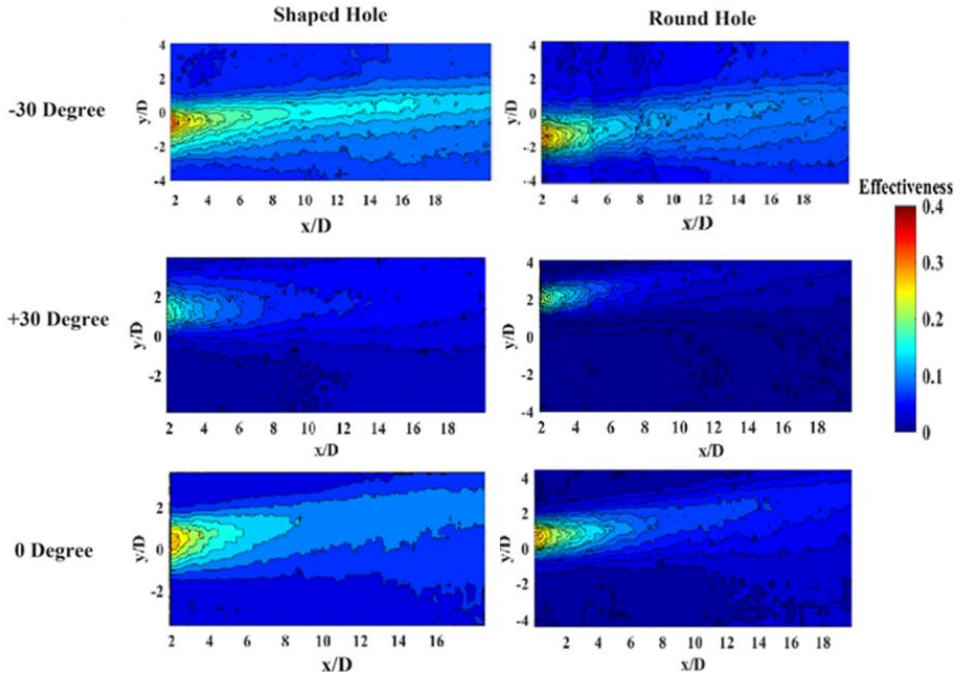

Figure 8.9: The effect of vortex rotational direction with shaped hole and round hole geometries.

Sensitivity to hole orientation

To identify the proper hole orientation for film cooling effectiveness enhancement, the effect of hole orientation angle is performed with skewing angles of -15^0, -30^0, -45^0, and -60^0. The surface effectiveness is shown in Figure. 8.10. The results show that the highest film cooling effectiveness is found when the hole is oriented from -30^0 to -45^0. The coolant vortex core is clearly seen in the -30 degree case. However, as hole orientation angle is further increased, coolant lateral spreading increases, but cooling effectiveness reduces. Hence, it is expected that the highest effectiveness value is from -30 to -40 degrees, when the coolant-generated vortex has a distinct sense of rotational direction with the incoming near-wall vortex.

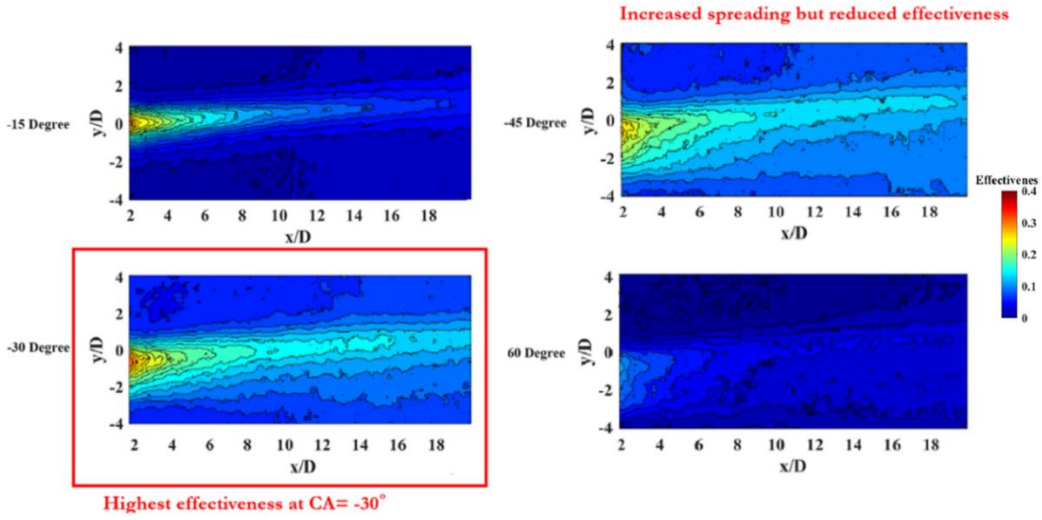

Figure 8.10: Film cooling effectiveness values for various hole orientations. The skewing angles are -15^0, -30^0, -45^0, and -60^0. Shaped hole geometry. The blowing ratio is 1.5.

Continued search for improved cooling effectiveness with a study having various coolant blowing ratios

Another item to examine is the coolant blowing ratio while searching for the highest film cooling effectiveness values. Here, the effect of coolant blowing ratio was documented with values of 1.0, 1.5, 2.5, and 3.5. As the highest effectiveness was found from -30 degree to -45 degree, cases were run with a shaped hole oriented at -30^0. The coolant injection-generated vortex has a distinct sense of rotational direction with the incoming vortex. The surface film cooling effectiveness is shown in Figure 8.11. In general, increasing coolant blowing ratio from 1.5 to 2.5 shows increased film cooling effectiveness. Nevertheless, reduced film cooling is also observed when the coolant blowing ratio is

further increased from 2.5 to 3.5. Thus, the highest effectiveness is found when coolant blowing ratio is 2.5.

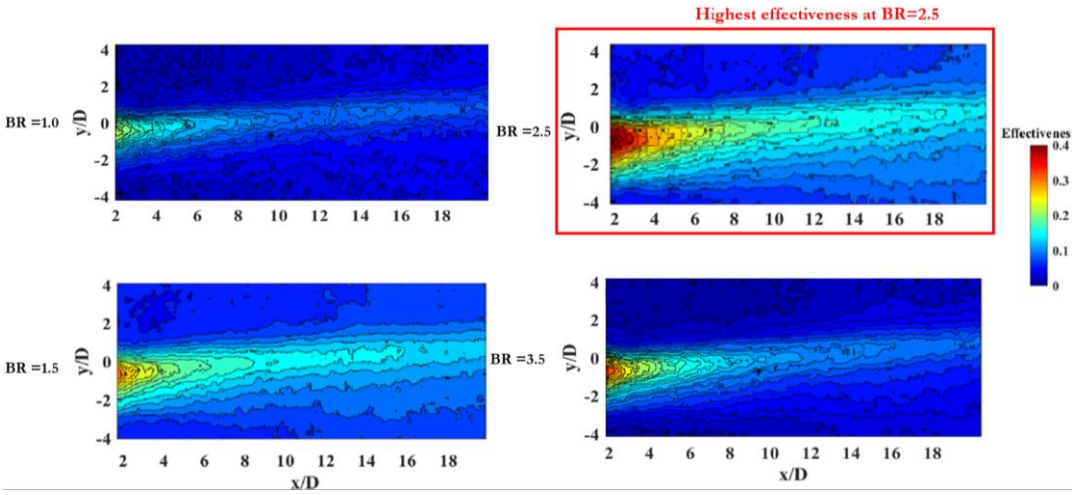

Figure 8.11: Film cooling effectiveness for various hole orientations. BR, blowing ratios are 1.0, 1.5, 2.5, and 3.5. Shaped hole geometry. The skew angle of the hole is -30^{0}.

This section intends to survey the coolant blowing ratios and discrete hole orientations for particular rotational directions between the coolant-generated vortex and the incoming near-wall vortex. The experimental results show that the highest film cooling effectiveness is achieved when the hole is oriented with a skew of about -30^{0}, and the coolant flow ratio is about 2.5. This combination of hole orientation and coolant blowing ratio should be considered using discrete hole film cooling on the endwall in turbine design.

8.4 Conclusion

This thesis aims to understand the migration of coolant at the exit of endwall discrete film cooling holes in the upstream of a turbine passage. The dominant secondary flow feature here is the horseshoe vortex. Disregarding other minor secondary flow features such as approach flow Reynolds number, crossflow, boundary layer thickness, turbulence intensity, acceleration and deceleration due to converging and diverging passages and coolant density. The experimental results here characterize the vortical effects on coolant concentration distributions (film cooling effectiveness values), that can be related back to the turbine environment from the flat plate wind tunnel measurements.

The experiments document coolant concentration distributions with various hole orientations ranging from -60^{0} to 30^{0}, coolant blowing ratios from 1.5 to 3.5, shaped and round hole geometries, and relative rotational directions between the coolant-generated

vortex produced by discrete hole injection and the incoming near-wall vortex produced at the passage leading edge. Thermochromic liquid crystal measurements were taken on the surface to characterize coolant migration on the surface in a time-average sense. Thermocouples were transversed within the flow downstream of injection recording the in-passage coolant concentrations on various downstream planes, as time-averaged distributions.

First, the discrete hole axis was oriented parallel to the approach flow direction. This aims at investigating the effect of an incoming vortex on coolant migration. The results show the migration of the coolant injection generated vortex produced from the film cooling hole with their distinct rotational direction. It is proved that vortices with a similar sense of rotational direction will merge, causing reduced film cooling effectiveness. Alternatively, vortices with the opposite sense of rotational direction will not merge, resulting in increased film cooling effectiveness on the surface. Additionally, cases of high film cooling effectiveness were found on the surface which had shaped-hole injection. This is because of reduced jet penetration due to a velocity vector toward the wall at the center of the counter-rotating vortex pair, and increased coolant lateral spreading due to the expanded hole exit. This case can serve as evidence of the approach vortex rotational effect on coolant migration that can be applied to realistic conditions in the turbine from the simplified flow in a flat plate wind tunnel. Comparable cases were reported by Ligrani and Mitchell (1994), Chung, et al. (2009), and Cui, et al. (2002) in the literature on a flat plate wind tunnel.

Then, discrete hole cases, with holes oriented at -30^{0}, generate a coolant injection vortex with a particular sense of rotational direction relative to that of the approach flow vortex. Such cases investigate the effect of relative rotation direction between the coolant-generated vortex and incoming near-wall vortex. It was found that the coolant was held to the surface by the incoming vortex, increasing film cooling effectiveness. Shaped holes show superior surface effectiveness values over those of round holes due to their reduced jet penetration and improved lateral spreading. Within the performed experimental parameter space, superior effectiveness was found for shaped holes at negative hole angle orientations. Thus, more cases were performed to find more optimal coolant blowing rates and hole orientations. Improved film cooling effectiveness values were found when hole orientations were from -30^{0} to -45^{0} and blowing ratios from 2.5 to 3.5. Overall, these cases help describe the cases performed by Barigozzi, et al. (2005) and Yang, et al. (2018), near

the pressure side of the turbine endwall when the holes are oriented toward the pressure side surface. This case is most significant for the rotor platform of the first stage of the turbine where upstream injection, such as purge flow, cannot penetrate to the downstream part of the passage due to rotational effects and resulting skewing of the inlet boundary layer flow. Cooling such a region is a major challenge for the gas turbine cooling designer.

Alternatively, the discrete hole was oriented at 30^{0}, producing a coolant injection vortex that possessed a similar sense of rotational direction to that of the incoming near-wall vortex. These cases show the effects of similar rotational direction between the incoming near-wall vortex and the coolant injection vortex. Results from in-passage coolant distributions show that the coolant-generated vortex was swept and merged into the incoming near-wall vortex, resulting in reduced film cooling effectiveness values on the surface. The coolant vortex core thus energizes the incoming near-wall vortex. Though energized, the incoming vortex was previously considered to be of no value or negative value for surface cooling purposes, but it is shown to have cooling value by the results of this thesis. In the turbine cascade, an increased heat transfer region was found at the suction side of endwall-suction wall corner due to the corner vortex there and the suction surface (vane or blade) due to the passage vortex there. Such a case has potential to resolve a critical issue, through energizing the suction leg of the horseshoe vortex, and, thus, modifying the passage turbine film cooling flow. By doing so, benefits are attained. As the suction leg of horseshoe vortex is energized, it can compete with the pressure leg of horseshoe vortex, thus delaying lifting off from the endwall. Additionally, it can obstruct the endwall crossflow which impinges upon the endwall-suction wall corner, thus weakening the suction corner vortex. In general, the data of these cases support evidence that describes coolant migration in the Stinson (2018) case, where the discrete, shaped hole oriented away from the suction wall leads to improved coverage.

Overall, the present experimental results investigate coolant migration as affected by several vortical effects. They are described mostly by time-averaged, in-passage and on-surface measurements. Nevertheless, to gain more insight into physics, it is necessary to consider the most realistic features of the flow. This requires further consideration of unsteady vortical interaction. Thus, investigation of unsteadiness is one important step following the experimental work reported in this thesis.

8.5 Future work

To understand the vortical effect on coolant migration in detail, more effort is needed on these several themes.

The first item is a case with optimal film cooling effectiveness that was found when the incoming near-wall vortex has a different sense of rotational direction to that of the coolant injection-generated vortex. A major focus is to identify the unsteady and three-dimensional vortical interaction between these two vortices.

The second theme that requires further investigation is the energizing effect on the incoming near wall vortex. As reported in this section, the coolant-generated vortex from the shaped hole energizes the incoming near-wall vortex most effectively when both of them have the same sense of vortex rotational direction. The optimal blowing ratio and the hole orientation were not identified in the present experimental parameter space, but knowing them would be important. Additionally, understanding the process when the coolant-generated vortex is swept, merges with, and energizes the incoming near-wall vortex is beneficial toward modifying the suction leg of horseshoe vortex under discrete hole injection and to possibly modify the competing effects between the pressure leg and suction leg of the horseshoe vortex. Such a merging process is an unsteady and three-dimensional process that is generally hard to document by time-averaging techniques.

A survey of the present capabilities of the community, as documented by a search of the literature, reveals a near impossibility of documenting the unsteady features of the vortices, due to measurement constraints in temporal resolution. Most of the in-flow measurement techniques, ranging from intrusive measurements, such as the five hole probe to non-intrusive techniques, such as PIV (Particle Image velocimetry) or MRV (Magnetic Resonance Velocimetry), are insufficient to record detailed unsteady flow features.

Presently, increased/decreased film cooling effectiveness values are mainly explained by time-averaged features, particularly the counter rotating vortex pair and the resultant jet entrainment (Coletti, et al., 2013) downstream of the film cooling jet. Nevertheless, the time-averaged measurements cannot capture many instantaneous features of jets in crossflow, such as eddy transport in the turbulent boundary layer, shear layer formation at the windward side of jet, shear layer breakdown at the leeward side of jet (Zhong, et al., 2016), and hairpin vortex bursting/breaking and resultant turbulent mixing (Sakai, et al., 2014). Understanding instantaneous features is significant toward improved finding film

cooling effectiveness values. An alternative way is to gain insight into the unsteadiness process from Computational Fluid Dynamics. An example is that of Large Eddy Simulation (LES) (Wang, et al., 2022), which provides information about the unsteady flow features. For simplified problems such as the interaction of the incoming near-wall vortex and the coolant (jet in crossflow), is sufficient to resolve the flow by current LES flow solvers. In general, to gain a clearer understanding of the jet in crossflow, and how that influences the film cooling effectiveness value, the instantaneous patterns from unsteady flow simulations should be considered and compared with time-averaged features from measurements. Such an approach must recognize the prevailing patterns from instantaneous processes and relate them back to the representative time-averaged features.

Overall, formation of the jet in crossflow remains an open question in both the heat transfer and fluid mechanics communities. This, coupled with the incoming near-wall vortices, represents a complicated flow with features that have not been resolved in the communities yet (Wang, et al., 2022). Nevertheless, the jet in crossflow remains a fundamental flow feature in various industrial and natural scenarios, ranging from the heating section of the gas turbine to the volcano eruption to the hypersonic scramjet to aortic heart valve flow in the cardiovascular system. To further our understanding of such physics is an enjoyable exploration with real-world impact.

Chapter 9. Closing remark

9.1 Summary

The general aim of this thesis is to cool the turbine endwall by discrete hole film cooling injection, as a complementary way for cooling by upstream injection. Literature about discrete hole film cooling in the past decades was discussed, providing a comprehensive perspective that must be explained by more than one study. A representative feature, "vortex rotational direction," is identified as driving secondary flow features upstream of the passage throat, dominating the migration of coolant from discrete hole injection points in the turbine cascade. Migration of coolant was documented herein by in-passage and on-surface coolant concentration measurement on the flat plate wind tunnel. The unsteady vortical effect on coolant migration is discussed. These thoughtful discussions, and measurements, provide sufficient perspective to describe the flow physics between passage secondary flow and discrete hole injection flows. More information about these findings is detailed in the conclusions of Chapters 7 and 8.

9.2 Future work

Several avenues can be investigated using results discussed in this thesis. One perspective is to apply endwall discrete hole film cooling on the suction side of the passage to complement the upstream injection, particularly by the "impingement vortex system (as shown in Figure 9.1)" as found in the design of close-coupled (in which the combustor and turbine are combined to be one unit) combustor-turbine interface (as shown in Figure 9.2). This impingement vortex, and the close-coupled combustor design have not been addressed in the thesis. However, large amounts of effort have been dedicated to the topic in the past few years at the Turbulent Convection Heat Transfer Laboratory at the University of Minnesota, as reported by Martinez Pajuelo (2024), Nawathe (2022), and Alqefl (2019).

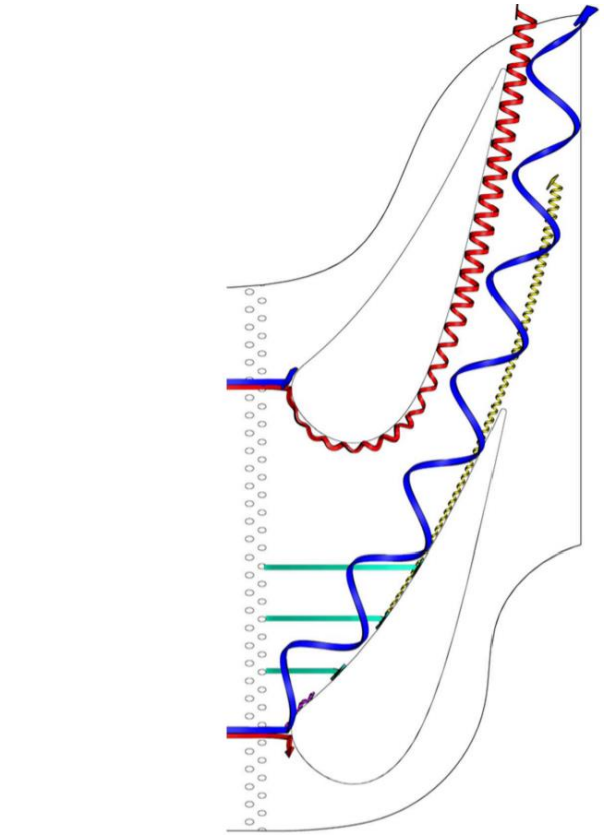

(a)

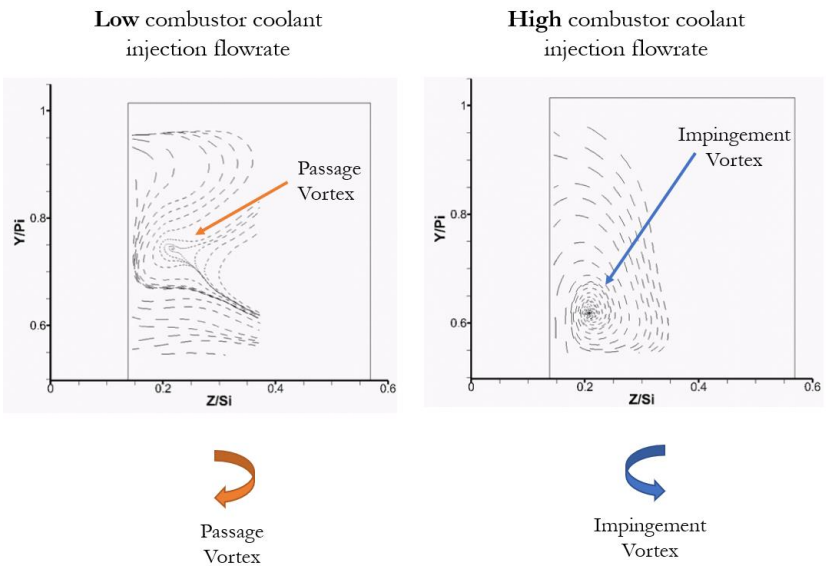

(b)

Figure 9.1: (a) Impingement-vortex-dominated secondary flow system. The vortex along the pressure surface is the impingement vortex. The larger vortex along the suction surface is the suction side leg of the horseshoe vortex, Nawathe, et al. (2023). (b) This figure shows the passage vortex at a low injection flow rate (left) and the impingement vortex at a high injection flow rate (right).

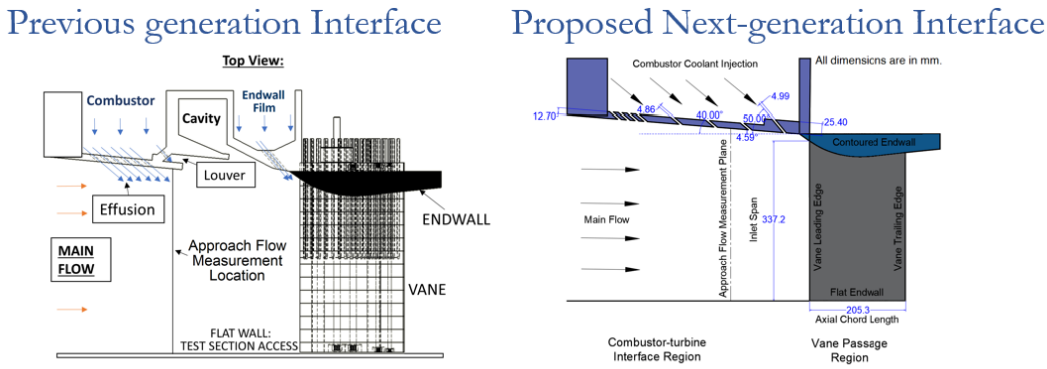

Figure 9.2: (a) The previous design of combustor turbine interface (left). The next generation or closed-couple, combustor-turbine interface (right). (Nawathe, 2022). This thesis is based on the "previous generation interface," which presently is the most common.

The challenge for such a scheme is the reduced cooling performance due to the lack of coolant migration toward suction surface, as shown in Figure 9.3. A step forward is to apply endwall discrete hole film cooling, reduce the influence of the conventional passage vortex secondary flow system on the suction wall (particularly at its transition toward the impingement vortex secondary flow system), and increase the upstream injection and combustor coolant flowrates. A transition in passage secondary flow takes place in the passage of the present study at MFR values of about 4.6%, as identified by Nawathe (2022). The present study about endwall discrete hole film cooling, combined with upstream coolant injection, offers a unique strategy to expand full-coverage endwall film cooling similar to that of Stinson (2018), as shown in Figure 9.4.

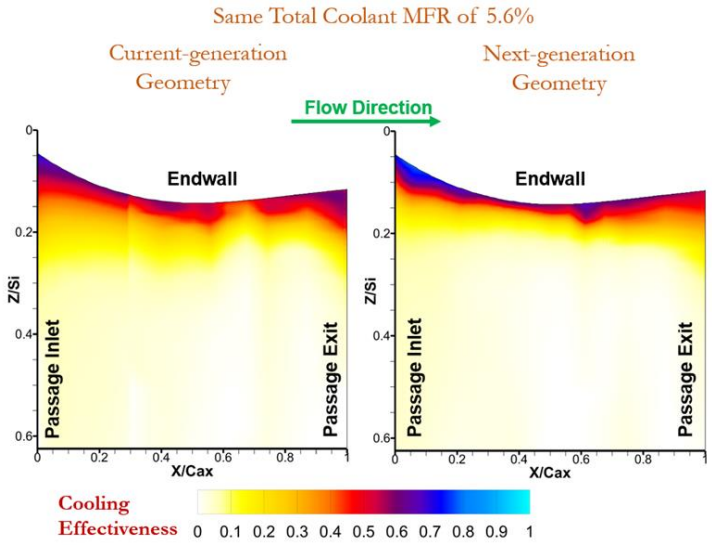

Figure 9.3: Suction surface film cooling effectiveness. Conventional passage vortex system (left). Impingement vortex system (right). (Nawathe, 2022).

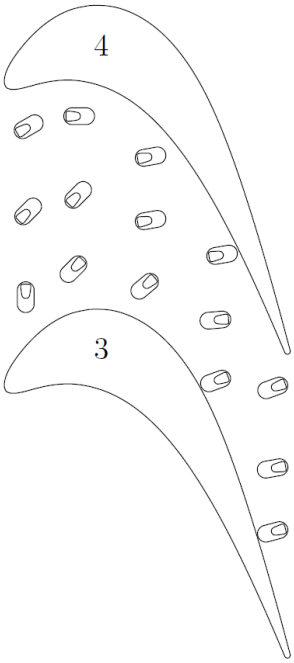

Figure 9.4: Endwall discrete hole film cooling scheme from Stinson (2018).

Gas turbines remain unreplaceable elements for nowadays energy systems and in the foreseeable future. A step toward net zero emission is to apply hydrogen to replace fossil fuel, which needs a redesigned combustor chamber. This will flatten the combustor exit temperature profile and increase the heat load on the turbine endwall. The first stage of turbine endwall (rotor and stator) is thus a region must be cool more efficiently (Barigozzi, et al., 2022). New understanding of secondary flow from this thesis is expected to benefit the cooling on the turbine endwall, and, in turn, reduce the emission from the gas turbine.

Bibliography

Aga, V. & Abhari, R. S., 2011. Influence of Flow Structure on Compound Angled Film Cooling Effectiveness and Heat Transfer. *ASME Journal of Turbomachinery,* Volume 133, p. 031029.

Aga, V., Rose, M. & Abhari, R. S., 2008. Experimental Flow Structure Investigation of Compound Angled Film Cooling. *ASME Journal of Turbomachinery,* Volume 130, p. 031005.

Alqefl, M. H., 2016. *An Experimental and Numerical Investigation of Endwall Aerodynamics and Heat Transfer in a Gas Turbine Nozzle Guide Vane with Slot Film Cooling,* s.l.: s.n.

Alqefl, M. H., 2019. *Aero-thermal Aspects of Endwall Cooling Flows in a Gas Turbine Nozzle Guide Vane,* s.l.: s.n.

Alqefl, M. H. et al., 2021. Aero-Thermal Aspects of Film Cooled Nozzle Guide Vane Endwall—Part 1: Aerodynamics. *Journal of Turbomachinery,* July, Volume 143, p. 121009.

Anderson, J. B. et al., 2017. *Freestream Flow Effects on Film Effectiveness and Heat Transfer Coefficient Augmentation for Compound Angle Shaped Holes.* s.l., s.n., p. V05CT19A027.

Barigozzi, G., Abdeh, H., Rouina, S. & Franchina, N., 2022. The Aero-Thermal Performance of Purge Flow and Discrete Holes Film Cooling of Rotor Blade Platform in Modern High Pressure Gas Turbines: A Review. *International Journal of Turbomachinery, Propulsion and Power,* Volume 7, p. 22.

Barigozzi, G., Benzoni, G., Franchini, G. & Perdichizzi, A., 2005. Fan-Shaped Hole Effects on the Aero-Thermal Performance of a Film-Cooled Endwall. *Journal of Turbomachinery,* February, Volume 128, pp. 43-52.

Blair, M. F., 1974. *An Experimental Study of Heat Transfer and Film Cooling on Large-Scale Turbine Endwalls.* Zurich, s.n., p. V01AT01A033.

Burns, G. W. et al., 1993. *Temperature-Electromotive Force Reference Functions and Tables for the Letter-designated Thermocouple Types Based on the ITS-90.* s.l.:National Institute of Standards and Technology (N.I.S.T.).

Childs, P. R. N., 2010. *Rotating Flow.* s.l.:Elsevier.

Chowdhury, N. H. K. et al., 2017. Turbine Vane Endwall Film Cooling With Slashface Leakage and Discrete Hole Configuration. *Journal of Turbomachinery,* February, Volume 139, p. 061003.

Chung, H. K., Na, Y. S. & Lee, J. S., 2009. *The Effect of Embedded Vortices on Film Cooling with Compound Angle Orientations.* s.l., Begel House Inc..

Chyu, M. K., 1996. Use of a laser-induced fluorescence thermal imaging system for film cooling heat transfer measurement. April.

Colban, W., Thole, K. A. & Haendler, M., 2008. A Comparison of Cylindrical and Fan-

Shaped Film-Cooling Holes on a Vane Endwall at Low and High Freestream Turbulence Levels. *Journal of Turbomachinery,* May, Volume 130, p. 031007.

Coletti, F. et al., 2013. Turbulent transport in an inclined jet in crossflow. *International Journal of Heat and Fluid Flow,* Volume 43, pp. 149-160.

Coletti, F., Elkins, C. J. & Eaton, J. K., 2013. An inclined jet in crossflow under the effect of streamwise pressure gradients. *Experiments in Fluids,* Volume 54, pp. 1-16.

Cui, X., Dai, R., Liu, P. & Lin, C., 2022. Effects of near-wall streamwise vortex on the film cooling performance of a fan-shaped hole. *Journal of Thermal Science and Engineering Applications,* Volume 14, p. 091013.

Cui, X., Liu, P., Lin, C. & Dai, R., 2022. Freestream effects on the interaction between near-wall vortex and film ejected from a fan-shaped hole. *Experimental Thermal and Fluid Science,* Volume 139, p. 110721.

Eaton, J. K., 1995. Effects of mean flow three dimensionality on turbulent boundary-layer structure. *AIAA journal,* Volume 33, p. 2020–2025.

Ekkad, S. V., Ou, S. & Rivir, R. B., 2004. A Transient Infrared Thermography Method for Simultaneous Film Cooling Effectiveness and Heat Transfer Coefficient Measurements From a Single Test. *Journal of Turbomachinery,* December, Volume 126, pp. 597-603.

Elkins, C. J., Issakhanian, E. & Eaton, J. K., 2011. *Magnetic Resonance Imaging Techniques for Measuring Film Cooling Flow Velocity and Effectiveness.* s.l., s.n., p. T10173.

Fric, T. F. & Roshko, A., 1994. Vortical structure in the wake of a transverse jet. *Journal of Fluid Mechanics,* Volume 279, p. 1–47.

Friedrichs, S., Hodson, H. P. & Dawes, W. N., 1999. The Design of an Improved Endwall Film-Cooling Configuration. *ASME Journal of Turbomachinery,* Volume 121, pp. 772-780.

Goldstein, R. J. & Chen, P. H., 1987. Film Cooling of a Turbine Blade With Injection Through Two Rows of Holes in the Near-Endwall Region. *Journal of Turbomachinery,* October, Volume 109, pp. 588-593.

Goldstein, R. J. & Cho, H. H., 1995. A review of mass transfer measurements using naphthalene sublimation. *Experimental Thermal and Fluid Science,* Volume 10, pp. 416-434.

Goldstein, R. J., Eckert, E. R. G. & Burggraf, F., 1974. Effects of hole geometry and density on three-dimensional film cooling. *International Journal of Heat and Mass Transfer,* Volume 17, pp. 595-607.

Goldstein, R. J., Eckert, E. R. G. & Ramsey, J. W., 1968. Film Cooling With Injection Through Holes: Adiabatic Wall Temperatures Downstream of a Circular Hole. *Journal of Engineering for Power,* October, Volume 90, pp. 384-393.

Goldstein, R. J. & Jin, P., 2000. *Film Cooling Downstream of a Row of Discrete Holes With Compound Angle.* s.l., s.n., p. V003T01A054.

Gunady, I. E. et al., 2021. Velocity and concentration field measurements and large eddy simulation of a shaped film cooling hole. *International Journal of Heat and Fluid Flow,* Volume 90, p. 108837.

Han, J.-C., Rallabandi, A. P. & others, 2010. Turbine blade film cooling using PSP technique. *Front. Heat Mass Transfer,* Volume 1, p. 013001.

Han, S. & Goldstein, R. J., 2005. Influence of Blade Leading Edge Geometry on Turbine Endwall Heat (Mass) Transfer. *Journal of Turbomachinery,* February, Volume 128, pp. 798-813.

Haydt, S. & Lynch, S., 2018. *Flow Field of a Shaped Film Cooling Hole Over a Range of Compound Angles.* s.l., s.n.

Haydt, S. & Lynch, S., 2019. Cooling Effectiveness for a Shaped Film Cooling Hole at a Range of Compound Angles. *ASME Journal of Turbomachinery,* Volume 141, p. 041005.

Hay, J. L. & Hollingsworth, D. K., 1996. A comparison of trichromic systems for use in the calibration of polymer-dispersed thermochromic liquid crystals. *Experimental thermal and fluid science,* Volume 12, p. 1–12.

Ireland, P. T. & Jones, T. V., 2000. Liquid crystal measurements of heat transfer and surface shear stress. *Measurement Science and Technology,* Volume 11, p. 969.

Jabbari, M. Y., Marston, K. C., Eckert, E. R. G. & Goldstein, R. J., 1996. Film Cooling of the Gas Turbine Endwall by Discrete-Hole Injection. *Journal of Turbomachinery,* April, Volume 118, pp. 278-284.

Ligrani, P. M. & Mitchell, S. W., 1994. Effects of Embedded Vortices on Injectant From Film Cooling Holes With Large Spanwise Spacing and Compound Angle Orientations in a Turbulent Boundary Layer. *Journal of Turbomachinery,* October, Volume 116, pp. 709-720.

Ligrani, P. M. & Mitchell, S. W., 1994. Interactions Between Embedded Vortices and Injectant From Film Cooling Holes With Compound Angle Orientations in a Turbulent Boundary Layer. *Journal of Turbomachinery,* January, Volume 116, pp. 80-91.

Ligrani, P. M., Ortiz, A., Joseph, S. L. & Evans, D. L., 1989. Effects of Embedded Vortices on Film-Cooled Turbulent Boundary Layers. *Journal of Turbomachinery,* January, Volume 111, pp. 71-77.

Ligrani, P. M., Ortiz, A., Joseph, S. L. & Evans, D. L., 1989. Effects of Embedded Vortices on Film-Cooled Turbulent Boundary Layers. *Journal of Turbomachinery,* January, Volume 111, pp. 71-77.

Ligrani, P. M. & Williams, W., 1990. Effects of an embedded vortex on injectant from a single film-cooling hole in a turbulent boundary layer.

Li, Y., Zhang, Y., Su, X. & Yuan, X., 2018. Experimental and numerical investigations of shaped hole film cooling with the influence of endwall crossflow. *International Journal of Heat and Mass Transfer,* Volume 120, p. 42–55.

Mahesh, K., 2013. The Interaction of Jets with Crossflow. *Annual Review of Fluid Mechanics,* Volume 45, pp. 379-407.

Moffat, R. J., 1988. Describing the uncertainties in experimental results. *Experimental Thermal and Fluid Science,* Volume 1, pp. 3-17.

Nawathe, K., Kim, Y. & Simon, T., 2023. Turbine Vane Passage Experiments Documenting Evolution of Secondary Flows With Changes in Combustor Coolant Injection Flowrates. *ASME Journal of Turbomachinery,* Volume 145, p. 041016.

Nawathe, K. P., 2022. *Secondary Flow, Turbulence, and Film Cooling Measurements in a Gas Turbine Vane Passage Downstream of a Novel Combustor-Turbine Interface,* s.l.: s.n.

Nawathe, K. P., Nath, A. R., Kim, Y. W. & Simon, T. W., 2023. Turbine Vane Passage Cooling Experiments With a Close-Coupled Combustor-Turbine Interface Geometry—Part I: Describing the Flow. *Journal of Turbomachinery,* August, Volume 145, p. 101005.

Nawathe, K. & Simon, T. W., 2022. *TURBULENCE MEASUREMENTS IN A TURBINE CASCADE FLOW*. s.l., s.n.

Ornano, F. & Povey, T., 2017. Experimental and computational study of the effect of momentum-flux ratio on high-pressure nozzle guide vane endwall cooling systems. *ASME Journal of Turbomachinery,* Volume 139, p. 121002.

Papa, M., Srinivasan, V. & Goldstein, R. J., 2011. Film Cooling Effect of Rotor-Stator Purge Flow on Endwall Heat/Mass Transfer. *ASME Journal of Turbomachinery,* Volume 134, p. 041014.

Royce, R., 1986. *The Jet Engine.* s.l.:John Wiley & Sons.

Sakai, E., Takahashi, T. & Watanabe, H., 2014. Large-eddy simulation of an inclined round jet issuing into a crossflow. *International Journal of Heat and Mass Transfer,* Volume 69, pp. 300-311.

Schmidt, D. L., Sen, B. & Bogard, D. G., 1996. Film Cooling With Compound Angle Holes: Adiabatic Effectiveness. *Journal of Turbomachinery,* October, Volume 118, pp. 807-813.

Schroeder, R. P. & Thole, K. A., 2014. *Adiabatic effectiveness measurements for a baseline shaped film cooling hole.* s.l., s.n., p. V05BT13A036.

Schroeder, R. P. & Thole, K. A., 2022. Adiabatic Effectiveness Measurements for a Baseline Shaped Film Cooling Hole. *Journal of Turbomachinery,* September, Volume 144, p. 121003.

Simon, T., Piggush, J., Amano, R. S. & Sundén, B., 2008. *Hot gas path heat transfer characteristics/active cooling of turbine components.* s.l.:WITPress.

Stinson, M. E., 2019. *Influence of Purge Flow Swirl and Passage Discrete Hole Injection Angle on Turbine Blade Endwall Cooling,* s.l.: s.n.

Stratton, Z. T. & Shih, T. I.-P., 2018. Effects of Density and Blowing Ratios on the Turbulent Structure and Effectiveness of Film Cooling. *Journal of Turbomachinery,* September, Volume 140, p. 101007.

Velte, C. M., Hansen, M. O. & Okulov, V. L., 2016. Multiple vortex structures in the wake of a rectangular winglet in ground effect. *Experimental Thermal and Fluid Science,* Volume 72, pp. 31-39.

Wang, H. P., Olson, S. J., Goldstein, R. J. & Eckert, E. R. G., 1997. Flow Visualization in a Linear Turbine Cascade of High Performance Turbine Blades. *Journal of Turbomachinery,* January, Volume 119, pp. 1-8.

Wang, Q., Moosania, M. & Zhou, C., 2022. Effects of an incoming vortex on the film cooling jet. *International Journal of Heat and Mass Transfer,* Volume 185, p. 122323.

Werschnik, H., Schiffer, H.-P. & Steinhausen, C., 2017. Robustness of a Turbine Endwall Film Cooling Design to Swirling Combustor Inflow. *Journal of Propulsion and Power,* Volume 33, pp. 917-926.

Yang, Z. H. O. U., Zhang, Y., Xinrong, S. U. & Xin, Y. U. A. N., 2018. Effect of inlet rotating swirl on endwall film cooling for two representative hole arrangements. *Chinese Journal of Aeronautics,* Volume 31, pp. 1095-1108.

Zamiri, A. & Chung, J. T., 2021. Large Eddy Simulation of Compound Angle Effects on Cooling Effectiveness and Flow Structure of Fan-Shaped Holes. *International Journal of Heat and Mass Transfer,* Volume 178, p. 121599.

Zhong, L., Zhou, C. & Chen, S., 2016. Effects of approaching main flow boundary layer on flow and cooling performance of an inclined jet in cross flow. *International Journal of Heat and Mass Transfer,* Volume 103, pp. 572-581.

Zhong, L., Zhou, C. & Chen, S., 2016. *Large eddy simulation of inclined jet in cross flow with cylindrical and fan-shaped holes.* s.l., s.n., p. V05CT12A006.

Zhu, R., Lin, E., Simon, T. & Xie, G., 2021. Investigation and numerical simulation on film cooling performance with an anti-vortex hole design: Influences of diameter ratio. *International Communications in Heat and Mass Transfer,* Volume 121, p. 105118.

Appendix A

A.1 Conference paper presented at Turbo Expo 2024

Chen, T, Stinson, M, & Simon, T. "Passage Secondary Flow Effects on Turbine Endwall Discrete Hole Film Cooling - A Review with Unique New Evidence." Proceedings of the ASME Turbo Expo 2024: Turbomachinery Technical Conference and Exposition. Volume 7: Heat Transfer: Combustors; Heat Transfer: Film Cooling. London, United Kingdom. June 24–28, 2024. V007T12A014. ASME. https://doi.org/10.1115/GT2024-123466